Design of new metallic glass composites and nanostructured alloys with improved mechanical properties

Junheng Gao

A thesis submitted for the degree of Doctor of Philosophy

January 2016

Department of Materials Science and Engineering

The University of Sheffield

Abstract

In this thesis two series of alloys were developed to obtain a combination of high strength, high ductility and work hardening. A new composition design strategy was proposed to create bulk metallic glass composites (BMGC) with high strength, large ductility and excellent work hardening from the brittle MgZnCa bulk metallic glass system. The volume fraction, size of both the dendrites and amorphous matrix can be effectively tuned by varying of the composition, and the yield strength, fracture strength and ductility also varies accordingly. The increase in alloying elements results in an increase in the volume fraction of amorphous matrix and a decrease in the dendrite size, which leads to higher yielding strength but lower ductility. The mechanical properties of the current Mg alloy can be interpreted by considering the BMGCs as a combination of the nanometer scale metallic glass matrix with a ductile dendritic structure. The high strength, large ductility and excellent work hardening observed in the $\mathrm{Mg_{91.5}Zn_{7.5}Ca_1}$ can be attributed to the homogeneous deformation of nanometre scale amorphous matrices, which delays the formation and rapid propagation of microcracks from the interface.

In addition, a series of in-situ-cast nanostructured CuZrTi alloys were successfully designed by appropriate choice of alloying elements and compositions. XRD and TEM analysis shows that the alloys consist of softer Cu solid solution and harder nano-scale $\mathrm{Cu_{51}Zr_{14}}$ matrix embedded with retained $\mathrm{Cu_5Zr}$ .The $\mathrm{Cu_{90.5}Zr_{7.5}Ti_2}$alloy exhibited a yield strength of 787MPa, a fracture strength of 1221MPa and room temperature uniform tensile elongation of 5.16%, exhibiting simultaneous ultrahigh strength and large uniform elongation. During tensile tests, the relatively softer (larger) primary Cu dendrites with numerous intragranular nanoprecipiates are believed to yield first, leading to substantial dislocation accumulation due to their relatively large grain size and the uniform distribution of numerous intragranular nanoprecipiates. With further increase in loading, the ultrafine Cu solid solution in the ultrafine clusters starts yielding

and dislocation multiplication commences in this ultrafine Cu. Meanwhile, the formation of deformation bands are believed to start in the primary Cu dendrites due to the already existing high dislocation density, both of which further contribute to the work hardening and uniform plastic deformation. Finally, the hard $\mathrm{Cu_{51}Zr_{14}}$ matrix commences plastic deformation and upon further loading, cracks start to form from the interface, leading to the final failure.

Acknowledgement

Firstly, I would like to express my sincere gratitude to my supervisor, Prof. Mark Rainforth, for his guidance, encouragement, patience, and support over the past 4 years and without his help, this work would not be half as good. My sincere gratitude also goes to my supervisor, Prof. Iain Todd, for his guidance and giving me freedom to pursue my own interests.

Next, I would like to say thanks to the research students in H6 for providing a friendly environment during my PhD study. My sincere gratitude also goes to all the fellow rapid solidifiers -Jake, Phil, Zhao, Haiyun, Yuhe- for creating friendly working environment and sharing their priceless experience. The technical staff in MSE are thanked for their kind support during the past 4 years. Especially, my sincere gratitude goes to Paul Hawksworth and Dean, for their timely help in maintaining the small scale melter and tensile test machine working.

I would also want to express my thanks to Dr Peter, Dr Peng Zeng, Dr Le Ma and Dr Cheryl in Sorby Centre for their training and timely help when necessary. Particular thanks go to Dr Jo sharp, Dr Huairou Zhang and Ms Dawn Bussey for helping out with HR-TEM and nanoidentation.

The financial support from CSC and the University of Sheffield is kindly acknowledged.

Last but not least, my sincere gratitude goes to my families, especially to my parents, my wife and my children, for their constant support and love.

Junheng Gao

January 2016

Table of Contents

Chapter 1

Introduction

It has been a constant challenge for material scientists to develop a material that is both strong and ductile. Recently, with the approach of global warming and energy crisis, high strength is much more desirable because stronger materials could reduce the weight of vehicles to enhance the energy efficiency. As part of this, much more attention has been paid to improve the ductility of bulk metallic glass and nanostructured materials in the past decades as high ductility is essential to prevent catastrophic failure of engineering materials.

Since 1960, with the discovery of a metallic glass system in AuSi[1], amorphous alloys have produced extensively scientific and commercial interest due to their special properties such as high strength (up to 4GPa), large elastic elongation for a glassy material (2%), which typically exceeds those compared with traditional polycrystalline alloys. In the time period from their discovery in 1960 through to the late 1990s, the research of metallic glass has centred on understanding those alloying characteristics that can stabilize the supercooled liquid to impede crystal formation. In the mid-1990s, the critical thickness to form a BMG for $Pd_{40}Cu_{30}Ni_{10}P_{20}$ reached as large as 10cm[2], which triggered a surge in commercial interest in BMGs. However, a large number of shortcomings were also identified when they are used as structural materials, particularly the low fracture toughness and almost zero tensile ductility below their glass transition temperature. To circumvent the poor ductility of BMGs, the research has shifted to the development of new classes of BMGs with high Poisson ratios and metallic glass composites. These are called Bulk Metallic Glass Composites (BMGCs). Super plasticity has been observed in the ZrCuNiAl alloy in compression through the appropriate choice of its composition by controlling elastic moduli[3]. However, no monolithic metallic glass exhibit significant ductility in tension, even for those with high Poisson ratios and such BMGs are expensive as they generally contain large amount of precious elements.

The mechanism of BMG fracture is the formation of highly localized shear bands under shear stress, followed by the shear band propagation without any impediment, as there are no microstructural features in monolithic BMGs to impede them. The idea of BMGCs is to improve the fracture toughness and ductility by introducing a ductile second phase into the amorphous matrix to impede the propagation of shear bands. Currently, most of the ductile BMGCs are developed from the Ti-(or Zr)-Be based system. The Ti-(or Zr)-Be-based composites are optimal for BMGC formation due to the lack of stable compounds between the constituents and Be, which prevents heterogeneous nucleation at the dendrites during quenching[4]. Moreover, the Zr-(or Ti)-based BMGCs exhibit a macroscopic strain softening phenomenon with an early onset of necking, which would limit their usefulness as engineering materials. However, given the toxicity of Be, there would be clear advantages to developing BMGCs without Be.

Since nanostructured materials (NMs) were first defined by Gleiter[5, 6], study in NMs has flourished over the last two decades. Bulk NMs are generally produced either through a multiple processing steps such as the synthesis and consolidation of nanoparticles, or by employing techniques that are not easily commercially viable such as severe plastic deformation. NMs produced by multiple processing steps often have defects, such as porosity, incomplete bonding and impurities, which cause premature failure under tension, sometimes even before the onset of yielding. In comparison, severe plastic deformation, such as equal channel angle extrusion (ECAP) and high pressure torsion (HPT), can synthesize flaw-free NMs that exhibit higher ductility than those synthesized by multiple-step approach. However, even these fully dense NMs often exhibit a very low or near-zero uniform tensile elongation (strain before necking) due to their poor strain hardening capacity. Uniform elongation can more accurately present the real ductility of NMs than the elongation to failure because uniform elongation is less affected by the gauge length. The large post-necking strain often imparts a false impression of high ductility in NMs as most of them have a very short gauge length. A high work-hardening rate is essential for improving the uniform elongation because it can help delay localized deformation under tensile stress[7]. However, NMs often have a low or no work-hardening because dislocation multiplication/accumulation is severely confined by the nanometre-scale geometries[8, 9] and the absence of defects in grain interior to interact with dislocations[10]. Recently, various strategies have been reported to improve the ductility and toughness of NMs, such as bimodal grain size, nanopreciptates, and pre-existing growth twins (PGTs). Among these, PGTs and intragranular nanoprecipitates are the most widely pursued and studied because both of them help with the multiplication and storage of dislocation, which increases the work-hardening rate. Nevertheless, it still remains challenging to enhance the uniform tensile elongation in bulk NMs due to the difficulties to embed toughing mechanisms such as PGTs and nanoprecipites in bulk NMs. In practice, PGTs often occur in eletrodeposited thin films and the characterized non-equilibrium grain boundaries in ultrafine alloys or NMs will preferentially motivate intergranular precipitation instead of intragranular precipitation even at room temperature.

The current project is mainly centred on the design of new alloys such as Mg-based bulk metallic glass composites (chapter 4) and CuZr-based in-situ-cast nanostructured materials (chapter 5) with both high strength and high uniform elongation by introducing work hardening mechanism. Chapter 2 presents a general literature review relevant to bulk metallic glass, metallic glass composites and nanostructured materials. Chapter 3 gives the detailed information of experimental work. Chapter 4 illustrates the new composition design strategy of the Mg-based bulk metallic glass composites and their microstructural characterization, mechanical properties, and the discussion of the feasibility of the composition design and the deformation mechanism of the composites. Chapter 5 focuses on the design of in-situ-cast nanostructured CuZrTi alloys, and the detailed microstructural analysis, solidification procedures and the deformation mechanism are carefully characterized and discussed.

References

[1] W. Klement, R.H. Willens, P.O.L. Duwez, Non-crystalline Structure in Solidified Gold-Silicon Alloys, Nature, 187 (1960) 869-870.
[2] A. Inoue, N. Nishiyama, Extremely low critical cooling rates of new Pd-Cu-P base amorphous alloys, Mater. Sci. Eng.: A, 226–228 (1997) 401-405.
[3] Y.H. Liu, G. Wang, R.J. Wang, D.Q. Zhao, M.X. Pan, W.H. Wang, Super Plastic Bulk Metallic Glasses at Room Temperature, Science, 315 (2007) 1385-1388.
[4] D.C. Hofmann, Bulk Metallic Glasses and Their Composites: A Brief History of Diverging Fields ,J. Mater., 2013 (2013) 0-8.
[5] M.A. Meyers, A. Mishra, D.J. Benson, Mechanical properties of nanocrystalline materials", Progress in Materials Science,Prog. Mater. Sci., 51 (2006) 427-556.
[6] H. Gleiter,Nanocrystalline materials,Prog. Mater. Sci., 33 (1989) 223-315.
[7] Y.H. Zhao, X.Z. Liao, S. Cheng, E. Ma, Y.T. Zhu, Simultaneously Increasing the Ductility and Strength of Nanostructured Alloys, Adv. Mater., 18 (2006) 2280-2283.
[8] X. Li, Y. Wei, L. Lu, K. Lu, H. Gao, Dislocation nucleation governed softening and maximum strength in nano-twinned metals,Nature, 464 (2010) 877-880.
[9] E. Ma, Nanocrystalline materials: Controlling plastic instability, Nat. Mater., 2 (2003) 7-8.
[10] E. Ma, T.D. Shen, X.L. Wu, Nanostructured metals: Less is more, Nat. Mater., 5 (2006) 515-516.

Chapter 2

Literature Review

2.1 Brief History of Metallic Glass and Metallic Glass Composites

Since the first metallic glass, $Au_{75}Si_{25}$, was discovered in 1960[1], metallic glasses have attracted widespread commercial and scientific interest because of their technological promise for practical applications and scientific importance in understanding the glass formation and glass phenomena. Initially, the focus of research in this area was centred on the rapidly quenched thin foils at a cooling rate of $10^5 - 10^6$ K/s [2-4]. The disordered atomic microstructure of the parent liquid alloy could be frozen into solid state materials by rapid-cooling molten alloys below their glass-transition temperature, which could kinetically bypass the nucleation and growth of crystalline phase as crystal nucleation and growth are time-dependent phenomena [5]. This rapid quenching technique permits large numbers of alloys to be made into the amorphous state in comparison with other methods such as vapour condensation. In 1974, the first metallic glass rod with millimetre diameter was fabricated by Chen from the ternary Pd-Cu-Si alloy using simple suction-casting method, termed bulk metallic glass (BMG)[6]. The well-known Pd-Ni-P BMG was produced by Turnbull and co-workers in 1982 using boron oxide fluxing method [7, 8]. As the melt was purified and heterogeneous nucleation was eliminated by fluxing materials, the amorphous structure of the parent Pd-Ni-P liquid alloy was retained into the bulk glass ingot with centimetre size solidified at a cooling rate as slow as 10K/s. In the late 1980s, new multicomponent BMG alloy systems such as La-Al-Ni consisting of common elements were developed by Inoue et al. in Tohoku University of Japan [9]. They systematically studied the glass forming ability (GFA) of ternary alloys of rare-earth materials with Al and ferrous metals. By casting alloy melts in to copper mould with water cooling, they successfully fabricated fully amorphous rods and bars with thickness up to several millimetres [10]. In 1993, Greer proposed the “confusion rules”, which indicates that the potential competing crystalline phase could be destabilized by larger number of components in an alloy system [11]. The intrinsic factors of an alloy (such as the number, purities and the atomic size of constituent elements, composition, cohesion among the metals, etc.) instead of external factors (such as cooling rate, etc.) play key roles in the glass formation [2]. As the development of multicomponent alloy compositions with high GFA has resulted in realistic critical cooling rate as low as 1K/s, the primary shortfall of most BMGs is the absence of plastic deformation at room temperature that restricts BMGs from being used extensively as structural materials[12, 13].

To overcome the low ductility problems, some research shifted to the toughening strategies such as designing new BMGs with high Poisson ratios and BMG composites. Although BMGs with high Poisson ratios have shown great promise, these alloys are usually expensive as they generally contain large amount of precious elements [14]. In the early of 2000’s, progress was made by recognizing that the brittle failure of BMG could be mitigated by the addition of ductile dendrite phase [15] which started a parallel field of research in bulk metallic glass composites(BMGCs). Currently, most of the ductile BMGCs are developed from the Ti/Zr-Be-based systems [5, 16-19]. The Ti/Zr-Be-based composites are optimal for BMGC formation due to the lack of stable compounds between the constituents and Be, which prevents heterogeneous nucleation at the dendrites during quenching [5]. Although many BMGCs have been discovered in a variety of systems, none of these alloys outperform the Ti/Zr-Be-based BMGCs in terms of mechanical properties such as strength and ductility. Hofmann et al.[17] suggest that the large plastic strain and toughness of these Ti/Zr-Be-based composites are based on the following two principles: (i) introducing dendrites with lower shear modulus compared with the amorphous matrix to initiate local shear banding; and (ii) matching the microstructural length scale such as the interdendritic spacing, λ, with the radius of the plastic zone (R_p) to impede the share band extension.

In 2002, He and his colleagues successfully created nanostructure-dendrite composite with ultrahigh strength comparable to BMG and ductility significantly higher than BMG by directly casting, which provides a new approach to strengthening materials [20]. Their multi-element recipe is a new twist on the idea used to develop BMGs, where multi elements are added to suppress the crystallization process. But in this case, some of the elements are used to stabilize the dendrite phase, while some of them also serve to ensure grain size stability. Moreover, their directly casting approach is superior to other processes to produce nanocrystalline alloys such as consolidation of nanocrystalline powder, or severe plastic deformation, which are either costly or introduce defects, e.g. porosity and impurities [21].

2.2 Formation of Metallic Glass

Early approaches to search for new metallic glass formers were mostly by tedious trial and error method [2], but researchers gradually understood that the correct choice of alloying elements would improve the glass forming ability significantly. In general, the GFA of BMG tends to increase as more elements are added, i.e. the "confusion rules"[11]. It is believed that a large number of alloying elements can destabilize the potential crystalline phase, which makes the melt more stable relative to the crystalline phase. In 2000, Inoue proposed the following three empirical rules [4], i.e. (1) Multi-component systems consisting of more than three elements, (2) the difference in atomic ratio among the three main elements above 12%, (3) negative mixing heat among the three main elements. They claimed that the atomic configurations of alloys satisfying the above empirical rules are significantly different from those of their corresponding crystalline phase. Moreover, the atomic configurations favour the glass formation in terms of the thermodynamic and kinetic aspects.

The ability to form glass by rapid cooling from equilibrium liquid state equals to supress the nucleation and growth of the corresponding crystalline phase within the supercooled liquid [2]. A key parameter for the prediction of GFA of metallic liquids is the reduced glass transition temperature $T_{rg}=\frac{T_g}{T_{liquid}}$[22]. For the supercooled liquid, the free energy difference between the liquid and a crystal provides a driving force for crystal nucleation, while the formation of the liquid–crystal interface introduce a positive interfacial energy that disfavours nucleation[2, 23]. An energy barrier (composition fluctuation) needs to be overcome for the formation of a nucleus. The nucleus growth requires the rearrangement of the liquid atoms, which is highly dependent on the atomic diffusivity or viscosity of the liquid. Therefore, the nucleation rate is determined by the product of a thermodynamic term, which depends on the probability of a fluctuation to overcome the nucleation barrier, and a kinetic term, which depends on atomic diffusion (or viscosity)[23], as shown:

$$I(T) = \frac{A}{\eta(T)} \exp\left[-\frac{\Delta G^*}{kT}\right] \tag{2.1}$$

Where I(T) is the homogenous nucleation rate, A is a constant on the order of 10^{32} Pa s/(m^3s), k is the Boltzmann's constant, T the absolute temperature, $\eta(T)$ is the viscosity. $\Delta G^*$is the activation energy which is the nucleation barrier for the formation of stable nuclei. $\Delta G^* = \frac{16\pi\sigma^3}{3(\Delta g(T))^2}$ under the assumption of classical nucleation theory, $\Delta g(T)$ is the free engery difference between liquid state and crystalline state, which is the driving force for crystallization, σ is the interfacial energy between the nuclei and liquid[23]. The positive interfacial energy opposes nucleation. Equation 2.1 outlines the general factors, which are crucial for glass formation: $\frac{1}{\eta}$ corresponds to the effective diffusivity, which describes the kinetic influence on the frustration of the melt; ΔG^* gives the thermodynamic aspect of glass formation [2]. The composition of the melt has a strong influence on the structure of the melt, which in turn reflects the viscosity and the value of ΔG^*[2, 4, 23]. A densely packed liquid structure generally results in a high viscosity. Both a high viscosity and a low value of ΔG^* are believed to be essential for high GFA of metallic glass [23, 24].

2.2.1 Thermodynamic aspects

From thermodynamic consideration, the Gibbs free energy difference, ($\Delta g(T)$), between the supercooled liquid phase and nucleus is the driving force for the nucleation of crystallite. Bulk metallic glass alloys naturally exhibit small$\Delta g(T)$ between the supercooled liquid phase and crystallite phase, which results in low nucleation rate and therefore high GFA [2, 4, 23]. The value of $\Delta g(T)$ can be calculated by integrating the specific capacity difference $\Delta C_p^{l-s}(T)$ according to equation 2.2[2]

$$\Delta g_{l-s}(T) = \Delta H_f - \Delta S_f T_o - \int_T^{T_o} \Delta C_p^{l-s}(T)dT + \int_T^{T_o} \frac{\Delta C_p^{l-s}(T)}{T} dT \tag{2.2}$$

Where ΔH_f and ΔS_f are the enthalpy and entropy of fusion, respectively, at the temperature of T_o, where the crystal phase and the liquid are in equilibrium. According to equation2.2, low $\Delta g_{l-s}(T)$ signifies a small enthalpy of fusion ΔH_f and large entropy of fusion ΔS_f. A multicomponent alloy is expected to have large ΔS_f as ΔS_f is proportional to the number of microscopic state[24] and consequently the increase in alloy component leads to larger ΔS_f and denser random packing in the liquid stage, which lowers the value of ΔH_f and the interfacial energy between the crystalline and liquid. This interpretation is consist with the “confusion principle”[11] and Ionue’s empirical rule[4] that large GFA is usually observed in the multicomponent alloy systems containing more than three elements.

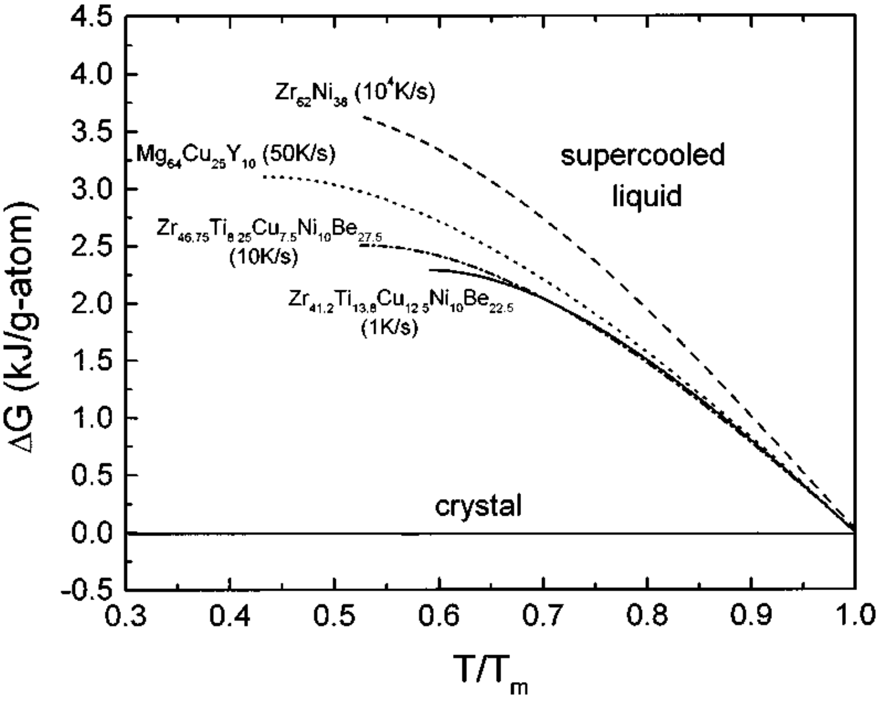

Fig2.1 Gibbs free energy difference between the supercooled liquid and the crystalline mixture for different glass-forming alloy [25].

In order to further investigate the influence of Gibbs free-energy difference between the supercooled liquid and the crystalline on the GFA, Busch, et al. compared the Gibbs free-energy difference of Vit1 with those of other typical eutectic, or close eutectic, glass-forming systems [25]. These alloys exhibit quite different critical cooling rate between 1K/s for Vit1 ($Zr_{41.2}Ti_{13.8}Cu_{12.5}Ni_{10}Be_{22.5}$ (at.%) BMGC) and 10^4 K/s for the binary $Zr_{62}Ni_{38}$. The alloys with high critical cooling rate tend to have larger Gibbs free-energy difference with respect to their crystalline state. The small Gibbs free-energy difference of these deep eutectic bulk glass forming alloy systems indicates that they already have a small free volume and a tendency to form short range order at or close to the melting point. These results support the assumption that the crystalline phase of multicomponent systems have relatively large configurational entropies of mixing and the fact that multicomponent systems with high GFA are very viscous and relatively dense liquid at the melting point and upon undercooling [25].

To more effectively predict the GFA , Turnbull was the first to promote the idea that the GFA should be coupled to the reduced glass transition temperature, $T_{rg}=\frac{T_g}{T_{liq}}$[22]. He calculated that when $T_{rg} > \frac{2}{3}$, the nucleation rate of the supercooled liquid become very low, which favours the verification of a melt. A large T_{rg} value means a large glass transition temperature, T_g and a low liquidus temperature, T_{liq}, which results in a small temperature window between the stable region of glass and the melt. In view of this, high GFA alloy can be found among alloy compositions with deep eutectics, which form liquids that are stable to relatively low temperature. Based on similar thermodynamic consideration, Lu et al. proposed that $\gamma = \frac{T_X}{T_g+T_{liq}}$ also reflects the GFA of metallic alloys and even gives better reference for judging the GFA among metallic glasses [26].

2.2.2 Kinetics aspects

From the perspective of kinetics, the kinetic parameter influencing glass formation is the viscosity (or diffusion) and the relationship between viscosity and diffusion are often expressed by the Stockes-Einstein relation $D=\frac{kT}{3\pi\eta l}$, where l is the average atomic diameter [23]. The viscosity of a liquid is commonly described by a modification of the Vogel-Fulcher-Tamman (VFT) relationship [27],

$$\eta(T) = \eta_o \exp\left(\frac{D^*T_o}{T-T_o}\right) \tag{2.3}$$

Where D^* is the fragility parameter which identifies the property of liquid[27], T_o is the VFT temperature, at which the barriers with respect to flow would go to infinity, and η_o is a constant inversely proportional to the molar volume of the liquid. The fragility describes the degree with which the viscosity of a supercooled liquid deviates from Arrhenius behaviour. Liquids are commonly referred to as “fragile” when $D^* < 10$ and ‘‘strong’’ when $D^* > 20$. Strong liquids exhibit a high equilibrium melt viscosity and show a more Arrhenius-like temperature dependence of the viscosity than fragile liquids [23].

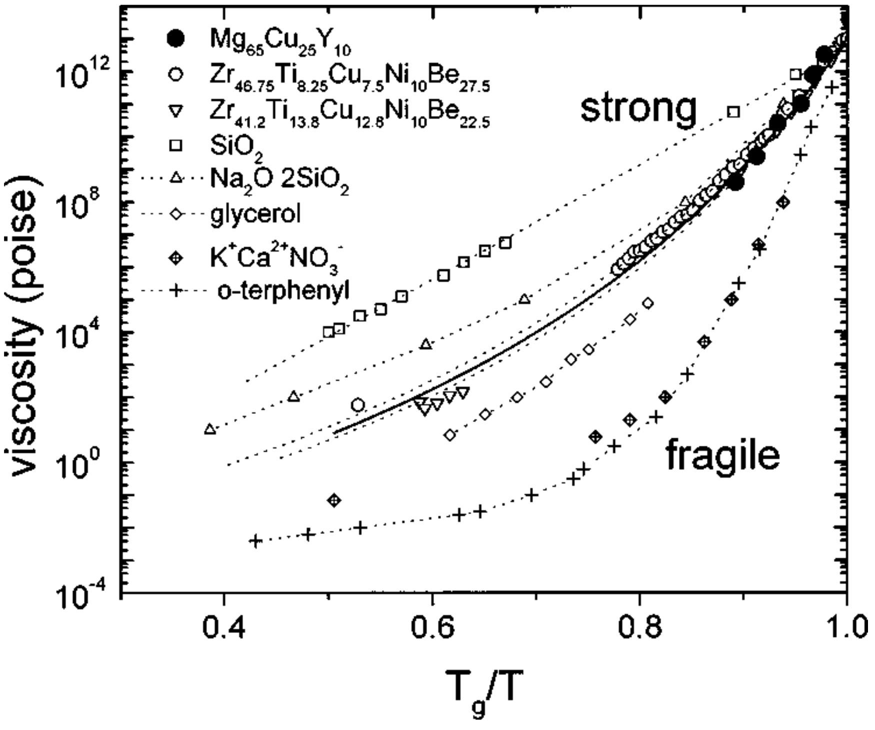

Fig2.2 A comparison of viscosity of various glass-forming liquid. The plot shows that the BMG forming liquid can be classified into strong liquid [25].

The change of viscosity of a melt as a function of undercooling can be used to classify the different liquids, because it reflects the mobility of atoms in the supercooling state. Fig2.2 compares the viscosities of several typical metallic glass melts with several typical non-metallic liquids [25]. SiO_2 is the strongest glass former and its melt has a fragility D* of about 100. It has a very low VFT temperature and a very high melt viscosity. The typical fragile glass former is O-terphenyl with a fragility of 5 and a low melt viscosity. The available viscosity data of the melts of BMG indicates that they behave kinetically much closer to high glass formers such as silicate melts than fragile glasses and have fragility around 20[2]. The viscosity of BMG melts is in the range of 2–5 Pa s, which is about three orders of magnitude more viscous than pure metals with viscosities of the order of 10^{-3}Pa s[28]. Notable exceptions to this are the Pd-based BMGs where low critical cooling rate (e.g. 0.15K/s for$Pd_{40}Cu_{25}Ni_{15}P_{20}$ [29]) combine with fragile behaviour. The neutron scattering studies show that the melts of BMGs share similar relaxation behaviour with strong liquids [30, 31], which have high viscosity and sluggish kinetics in the undercooling state. The nucleation and growth of thermodynamically favoured phases in the supercooled melt are retarded by the poor mobility of the constituents, which lead to large GFA and high thermal stability of the supercooled liquid state. The fragile glass formers (with a large change in viscosity closeT_g) are difficult to vitrify because of the enhanced atomic transport.

2.2.3 The enhancement of glass forming ability by minor element addition

Microalloying is believed to be an effective means to improve the glass forming ability of various glass forming alloys [32-36]. For instance, the critical diameter of Cu-Zr-Al metallic glass rod can be increased to 8mm from 3mm by adding only 2-5 at.% Y to the glass forming system[33]. In order to rationalize the micro-alloying effect, different theories have been proposed. For example, it is believed that the minor addition could scavenge oxygen impurities which might act as nucleation sites, and thus hampers inhomogeneous nucleation of crystals in the supercooled melts[33, 37, 38]; or that, after micro-alloying, the resultant composition could approach a deep eutectic composition, therefore stabilizing the glass forming liquid[33]. Furthermore, Zhang, et.al proposed that micro-alloying could introduce atomic-level strain energy into the liquid, which impairs the thermodynamic driving force for crystal nucleation [35].

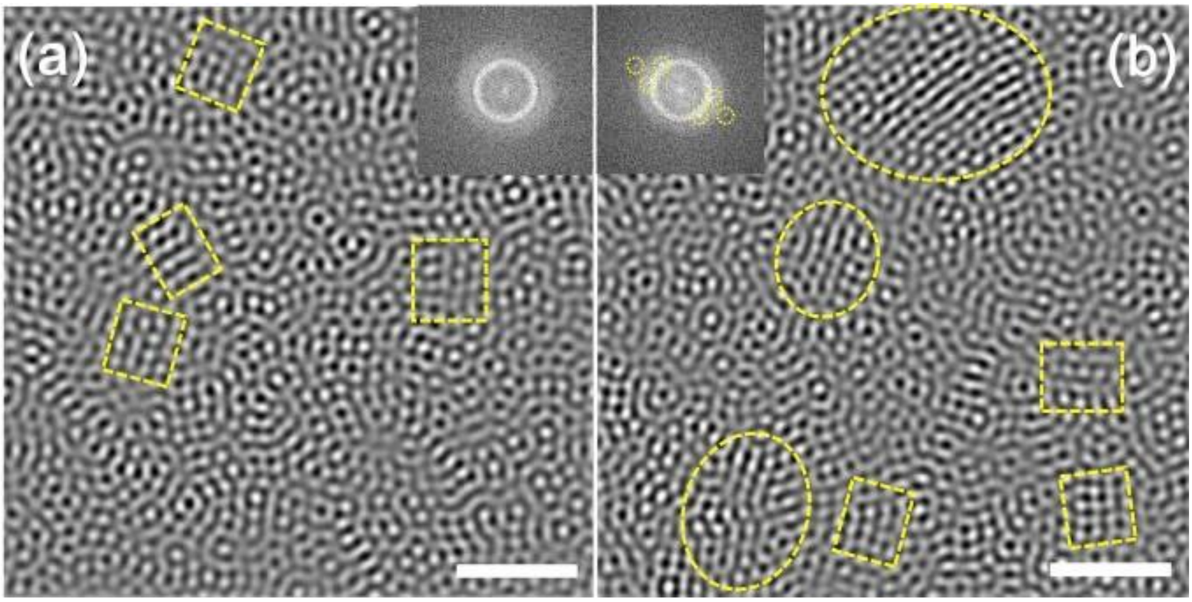

Fig2.3 Typical localized crystal-like atomic ordering observed in the as-cast $Cu_{46}Zr_{47-x}Al_7Y_x$ (x=0,2) BMG alloys. (a) x=0 and (b) x=2 are the FFT-filtered images, showing the atomic configurations for an amorphous region with ordered clusters. Insets show the corresponding diffraction patterns of a and b obtained via FFT. (Scale bar=2 nm)[39].

Recently, Wang et.al studied the structural origin of micro-alloying effect at the atomic scale, based on Cu-Zr BMG system [39]. As shown in Fig 2.3, the minor addition of Y tends to promote the crystal-like structure growth in CuZrAl alloy. Fig 2.3(b) shows that the growth of the crystal-like structure is evident at many places (yellow circled area) in Y-bearing BMG; however, the size of these crystal-like structure is limited within 2-4nm, which is insufficient to change the overall amorphous structure. The limited growth of micro-alloying introduced the local crystal-like structure could be attributed to the introduction of the atomic-level strain energy into Gibbs free energy for crystal nucleation[35]and/or presence of the icosahedral-like clusters, which situated around the crystal-like order regions and act like pinning ‘particles’ to suppress large-scale crystallization, as discussed in Ref[40]. Moreover, the results of nanobeam EDS analysis reveals that the crystal-like atomic clusters of about 4 nm is enriched in Cu and contains Y, while their surroundings are free of Y and poor in Cu but enriched in Zr.

The local fluctuations in chemical composition could be attributed to the partial substitution of Zr with Y in consideration of the positive mixing enthalpy (35 kJ/mol) between Y and Zr. Therefore, it is believed that the emergence of the crystal-like orders is spatially associated with the added Y element, leading to local chemical fluctuations that stabilize the Y-containing supercooled liquid.

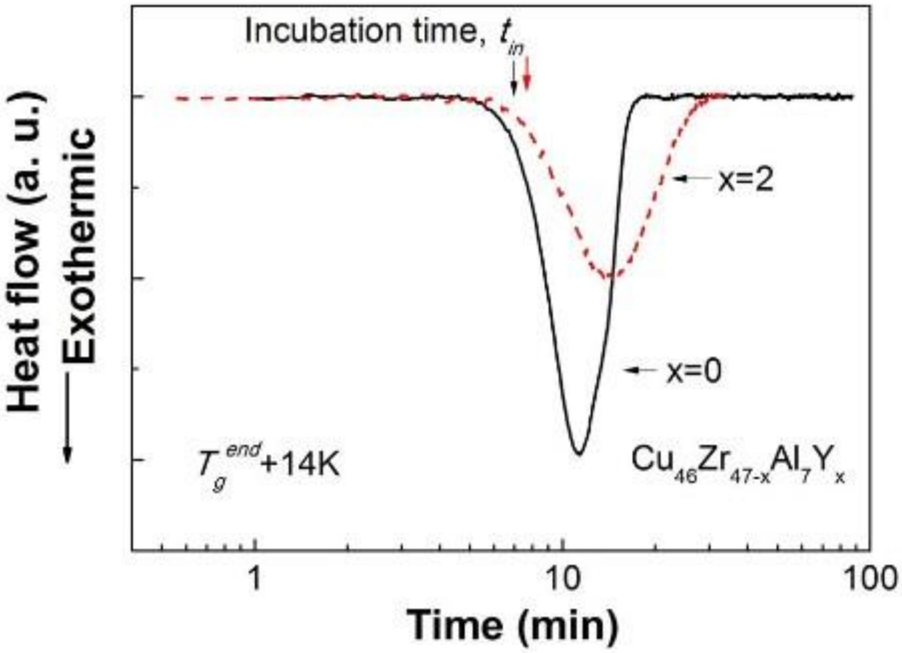

Fig2.4 Isothermal DSC traces for $\mathrm{Cu_{46}Zr_{47-x}Al_7Y_x}$ (x=0, 2) held in supercooled liquid region at $\mathrm{T_g^{end}}$+14k[39].

To correlate the observed atomic structure with the macroscopic thermodynamics, the crystallisation behaviour of $\mathrm{Cu_{46}Zr_{47-x}Al_7Y_x}$ (x=0, 2) was examined using DSC. As shown in Fig 2.4, the clear exothermic peak in the isothermal DSC traces indicates their glassy nature. More interestingly, after the minor addition of the 2 at % Y, the isothermal exothermic crystallization reaction is significantly delayed, as indicated by the increased incubation time in Fig 2.4. The delayed exothermic crystallization reaction suggests that the minor addition of

2 at.% Y leads to a distinct increase in the viscosity of the supercooled liquid, echoing the formation of more atomic crystal-like clusters in the Y-bearing alloy.

To explain why the increasing degree of crystal-like structure does not accelerate the overall crystallization rate in the glass forming liquid, one may note the competition between the growth of crystal- and icosahedra-like structure, taking into account that previous study has indicated their coexistence in the Cu-Zr based BMG[41]. As the atomic ordering with a spherical-like symmetry maximizes local atomic densities and is usually favoured over the latter during an ordering process of a glass-forming liquid [42], these icosahedra-like clusters could pin the boundary of the crystal-like clusters formed later and thus constrain their growth [40]. Once the growth of the local crystal-like order is constrained, the increased overall structural ordering reduces the thermodynamic driving force for crystallization. As illustrated in Fig2.5, the free-energy of the metallic glass-forming liquid is lowered down as a result of the structural ordering due to micro-alloying. According to the classic thermodynamics, the free-energy difference, Δg^{l-c} between the liquid phase and crystals decreases. As illustrated in Ref [43], the free energy barrierΔG^{*} against crystallization is expressed as $\Delta G^{*} = \frac{16\pi {\sigma_{l-c}}^{3}}{3(\Delta g^{l-c})^{2}}$, where σ_{l-c} is the interface tension between the liquid and the crystal. For a givenσ_{l-c}, ΔG^{*} increase with a decrease of Δg^{l-c}. As the crystaliziaton rate is expressed as $I(T) = \frac{k_n}{\eta} \exp\left[-\frac{\Delta G^{*}}{k_B T}\right]$, where k_n is a constant, $\eta$is the viscosity, k_B the Boltzmann constant and T the temperature. The crystallization rate becomes slow due to the micro-alloying induced structural ordering, therefore enchanting the GFA.

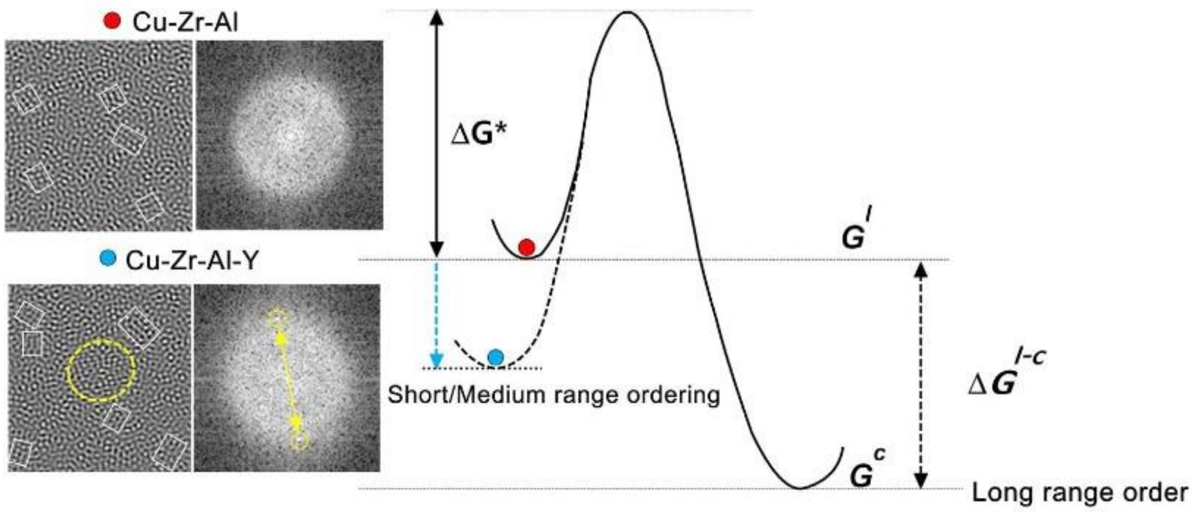

Fig 2.5 Schematics of the free energy profiles for the $Cu_{46}Zr_{47-x}Al_7Y_x$ (x=0, 2) BMG forming supercooled liquids showing the effect of structural ordering due to the minor Y element addition [39].

2.3 Mechanical Properties of Bulk Metallic Glass

Due to the absence of long-range translational symmetry [4, 44-46], metallic glasses possess some excellent mechanical and physical properties, which are promising for current and future applications [3, 47-49]. One of the enduring attractions of metallic glasses is their impressive suite of mechanical properties [12]. For example, metallic glasses generally exhibit elastic moduli on the same order as conventional crystalline alloys sharing comparable composition, but their room temperature strengths are significantly in excess of their corresponding polycrystalline alloys. However, they usually suffer a strong tendency for shear localization and macroscopically brittle failure at room temperature in tension [12, 50-53], although clear evidence has shown that they are capable of legitimate plastic shear at micro/nano scale [53-57].

2.3.1 Deformation mechanism

The atomic bonding in metallic glasses is of primarily metallic character, so strain can be readily accommodated at atomic scale through changes in neighbourhood [12]. For example, atomic bonds can be broken and reformed without significant concern for, e.g. the rigidity of bond angles as in a covalent solid, or the balance of charges as in an ionic solid. However, unlike crystalline metals, where dislocations can change atomic neighbourhood to accommodate strain at low energies or stress, the local rearrangement of atoms in metallic glass requires high energy or high stress due to the absence of long-range ordered structure.

During deformation of metallic glass, there is a general consensus that a local rearrangement of atoms is required to accommodate strain [41, 58]. The volume fraction and size of rearrangement atoms during deformation strongly depends on different alloy systems [58]. Even though many bulk metallic glass alloys have been developed in different alloy systems in recent years [3, 4], a fundamental knowledge on the relationship between structure and deformation behaviour of metallic glass is still not fully resolved, although there are several different theories to address the correlation between the glassy structures and the deformation mechanisms of MGs.

2.3.1.1 Shear Transformation Zone Theory

Argon and Kuo suggested that, in order to accommodate the applied shear strain, small clusters of close-packed atoms will rearrange spontaneously and cooperatively, which is termed a shear transformation zone (STZ) as illustrated schematically in Fig2.6 [59-62].This shear transformation zone theory is proposed based on an atomic-analogue bubble-raft model and also referred to as a “flow defect” or “τ defect”[61, 63], a local “inelastic transition”[60]. During shear plastic deformation, the STZ essentially involve a cluster of atoms that undergoes an inelastic shear distortion from one relatively low energy configuration to another configuration with relatively low energy via an activated state with high energy and a large volume [12]. With further increase in the applied shear strain, more STZs will be triggered and this consequently leads to the formation of shear bands [64, 65].

A quantitative model of STZ behaviour was proposed by Argon [66, 67], suggesting that the STZ operates within the elastic confinement of the glass matrix, and the stress and strain redistribution resulted by the shear distortion occurs around the STZ region. The calculation of the free energy for STZ activation basing on the elastic constants of MG is given by [12, 67, 68].

$$\Delta F_0 = \left[\frac{7-5V}{30(1-V)} + \frac{2(1+V)}{9(1-V)}\beta^2 + \frac{1}{2\gamma_0} * \frac{\tau_0}{\mu(T)}\right] * \mu(T) * {\gamma_0}^2 * \Omega_0 \qquad (2.4)$$

Where v is the Poisson’ ration, τ_0 is the athermal stress at which the STZ transforms, and $\mu(T)$ is the temperature-dependent shear modulus. The second term in the brackets contains the dilatational energy related to the STZ action. Β is the ratio of the dilatation to the shear strain; γ_0 is the characteristic strain of a STZ and generally adopted to be of order of ~0.1 and $\Omega_0$is the characteristic volume of STZ and usually consists of a few up to ~100 atoms, as observed in simulation and a variety of experimental measurement [59, 61, 68-76]. By adopting the typical value of transition metals, the energy of a STZ is estimated to be on the order 1-5eV, or ~20-120kT_g, with k being the Boltzmann constant. According to the original model of Argon et al. [68, 77-79], a dynamic theory for STZ operation has been proposed and it contains the following several characteristics[12, 47, 52, 58, 62, 72]: (i) due to the saturation and jamming of the system, the transformed STZ is irreversible along the same shear direction; (ii) because the creation rate of newly formed STZs is highly related to their transformation rate of pre-existing STZs, the creation and annihilation rates of STZs are proportional to that of the irreversible plastic deformation; (iii) the attempt frequency of the transition is coupled with the noise in the system, which is driven by the strain rate; (iv) the transition rates between jammed and flowing zones are highly dependent on the applied stress.

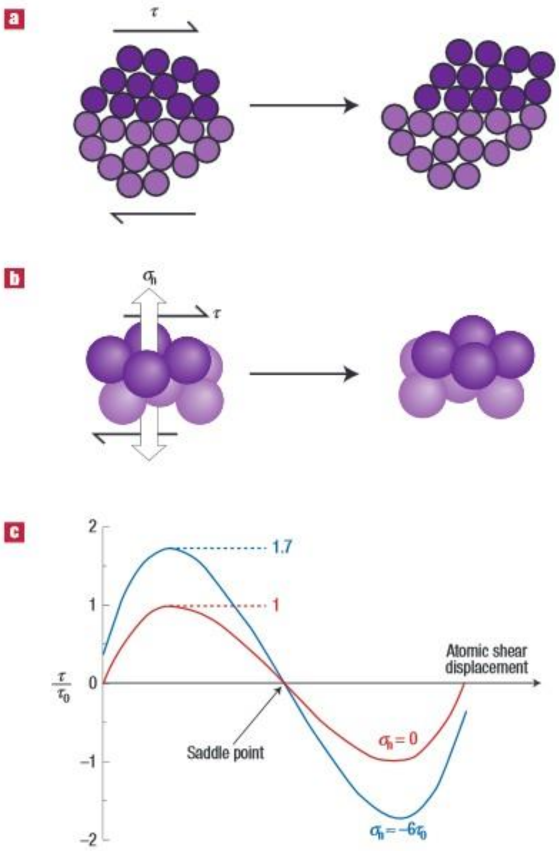

Fig2.6 Schematic representations of STZs in amorphous alloy. (a) A two-dimensional schematic representation of a STZ in a MG. In order to accommodate an applied shear stress τ, a shear displacement occurs with the darker upper atoms shift to right-hand side with respect to the lower atoms. (b) A 3-D representation of STZ. The four upper atoms move together with respect to the five lower atoms, and the shear direction is the trajectory with constant normal stress σ_n. (c) the applied shear stress τ required to maintain a given atomic shear displacement, normalized by the maximum value of τ at σ_n=0, τ_0. The starting and ending structures shown in b correspond to the beginning and end of the curve. The maximum value of τ required to complete the shear displacement increases with an applied compressive stress [62].

2.3.1.2 Free volume model

As an alternative model for the plastic flow in metallic glass, the free volume model was first proposed by Turnbull and co-workers [80] and was first applied to explain the deformation of glass by Spaepen et al.[81]. In this model, the deformation process is viewed as a series of discrete atom jumps in the amorphous structure, as depicted in Fig 2.7[81]. The free volume is the empty space around the constituent atoms and is believed to be distributed statistically among all the atoms in metallic glasses [82, 83]. As the atom jumping is a diffusion-like process, the characteristic energy scale is of the order of activation energy for diffusion,15-25 kT_g ,which is very close to the lower end of the range for the expected energy for an STZ operation[80, 81, 84]. However, the STZ activation energy is highly dependent on subtle redistribution of many atoms in a diffuse volume, while the activation energy for the free volume model is more related to a highly localized atomic jump into a vacancy in the amorphous structure [12].

The inelastic relaxation preferentially occurs at the sites with high free volume by local atom rearrangement due to the poor mechanical coupling at these regions [12, 58, 64, 81]. The destabilization of the amorphous structure is preferred to occur at these regions with an increase of the applied stress. The free volume keeps constant at low stresses condition because the annihilation rate is equal to its creation rate [12, 58, 64, 81].With further increasing in stress, the creation rate is larger than the annihilation rate, so the free volume increases at this stage. Accompanying the increase of free volume, softening occurs, then followed by the decreasing of applied stress, which leads to the decrease of driving force for the creation of free volume until a steady state is achieved between the annihilation and creation rate [12, 48, 58, 64, 81].

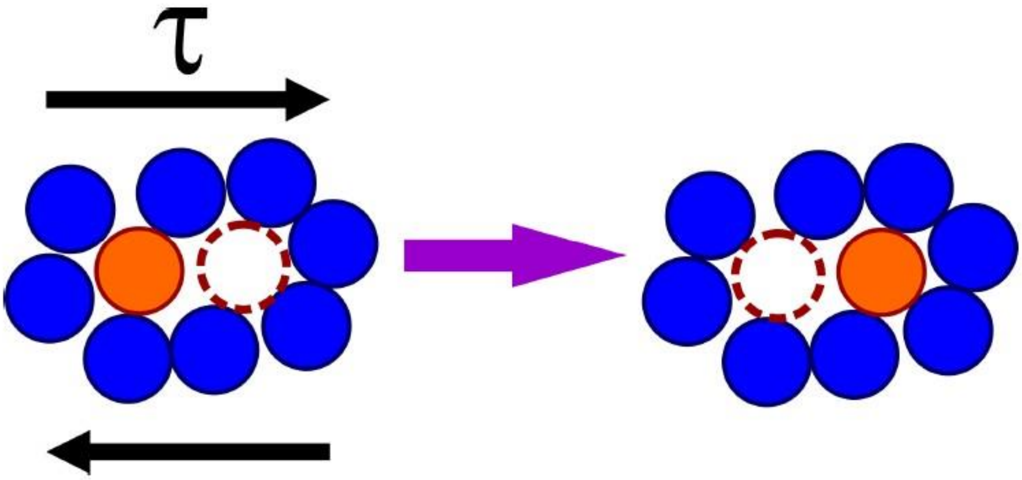

Fig2.7 A two-dimensional schematic representation of the plastic deformation behaviour basing on the Free volume model [81].

2.3.2 Sample size effect on the deformation behaviour of metallic glass

It has been established that, for single-crystal metals in micrometre or submicron scale, smaller is stronger, because the small the sample size, the nucleation and operation of dislocation is more difficult, resulting in higher stress for yielding and plastic flow[85-88]. Therefore, it is intriguing whether a parallel “size effect” exists for metallic glass strength, although these findings in single crystals cannot be directly applied to metallic glass due to absence of dislocation in the amorphous structure [89]. In order to study the influence of sample size on the mechanical properties of metallic glass, a number of experiments have been carried out in recent years on a variety of alloy systems, including Pd-[90], Cu-[91], Zr-[53, 91-93], Fe-[94]and Mg-based BMGs[94, 95]. Unfortunately, there is a controversial debate about the size-strengthening effect, as several groups reported that the reduction of sample size yields not only increased strength and ductility but also the transition in deformation mode from shear localization to homogenous-like flow [53, 55, 57, 85], while others claim little or no size-effect on the mechanical behaviours[90, 91, 96, 97].

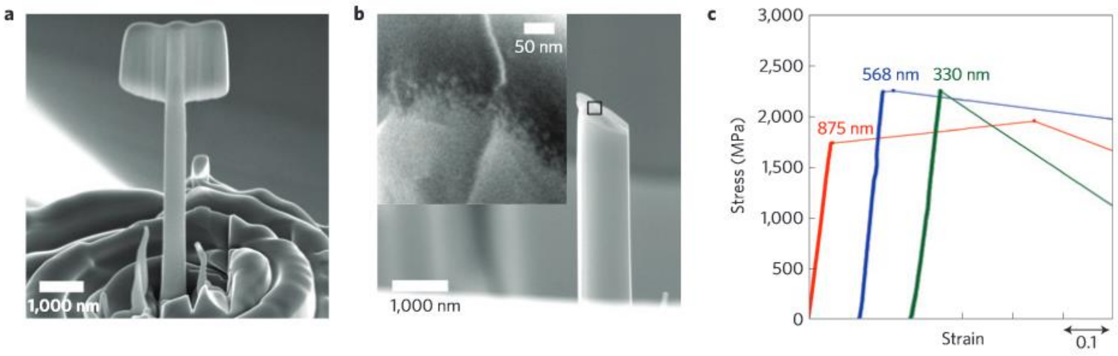

Fig2.8 Typical SEM images and stress train curves of nanopillars larger than 200nm for tension test. (a) as-produced nanopillar, (b) as-deformed nanopillar, the inset in (b) is the magnified image taken from the square near the fracture region in (b) showing the formation of shear band, (c) stress-strain curves for samples with different diameters [53].

Guo et al.[54] first observed that when the extrinsic size of Zr-based BMG reduced to several hundreds of nanometres, tensile ductility can be clearly observed based on the in situ tensile test in a transmission electron microscope. Volkert et al. [57] quantitatively illustrated a distict change from shear-band mediated plastic deformation of glassy $Pd_{77}Si_{23}$ micro-columns to homogeneous follow deformation when the specimen diameter below 400nm. These results were further confirmed by Ref. [53]. Jang and Greer conducted in situ nanotension tests on Zr-based BMG with diameter in the range of 875nm-100nm.As shown in Fig2.8c, the fracture strength increases with a decrease in the sample diameter and these curves share the same signature: elastic loading followed catastrophic failure at 3-5% strain, without any notable plastic strain. Shear banding dominated the deformation process for all the samples with diameter above 200nm, as observed in the inset of Fig2.8b, so it seems that the reduction of size sample size to 200nm does not affect the deformation although larger brittle-to-ductile transition size (300nm) has been observed in Al-based BMG[89, 91].

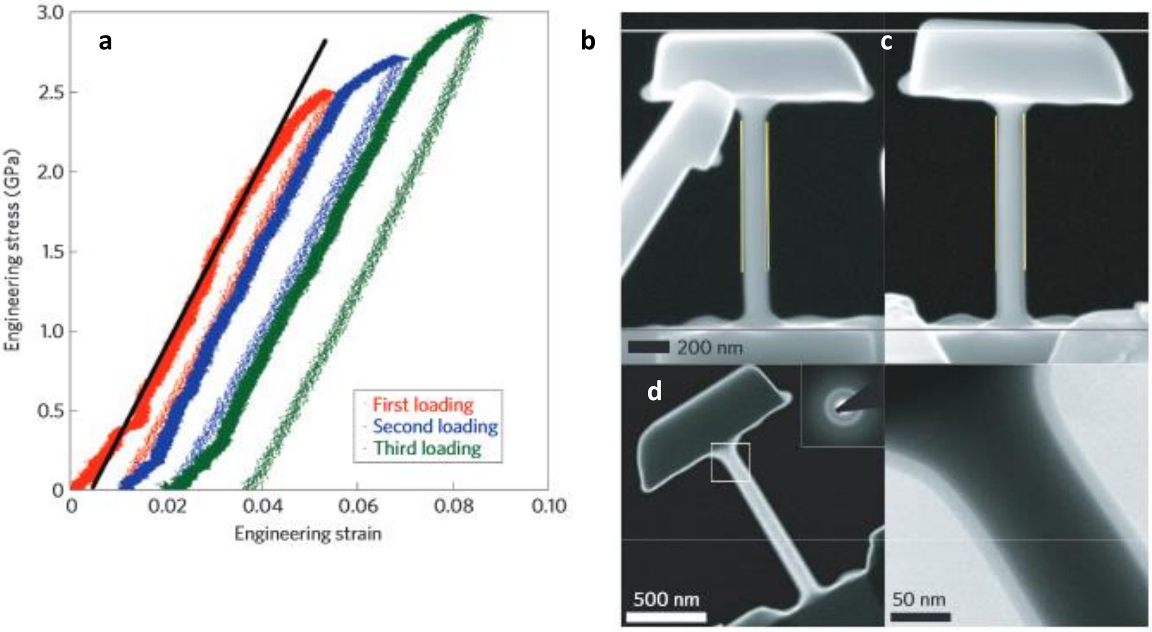

Fig2.9 Multiple-loading in situ nano-tension results for 100nm-diameter specimen. (a) Engineering stress strain curves for loading and unloading three times before the final failure. SEM images (b and c) showing that, in comparison with the as-fabricated sample (b), the sample after the multiple loading (c) became taller and small neck was observed near the head as show in the vertical lines. (d) Dark-field TEM image and corresponding diffraction pattern after tensile test. High magnified bright-field TEM images from the square region in right-hand side of (d)[53].

However, the 100nm-diameter sample deformed homogenously under a uniaxial tensile load. According to the engineering and true stress-strain curves, these 100nm-samples show characteristics more typical of ductile metals, that is, nonlinear plastic deformation after yielding, work hardening, ultimate tensile strength and necking. However, although the stress-train curves of these100nm-diameter samples share similar characteristics with that of ductile metals, the fracture micrograph is different from the cup-and-cone shape characteristics of ductile metals, fracturing by shearing off along 53° with respect the loading axis, suggesting that these smallest samples deform like ductile metals but fail like metallic glass. The multiple loading-and-unloading tests further confirm the working hardening behaviour of these 100nm samples, as shown in Fig2.9a. The loading cycle consists of loading up to a few plastic strains and then completely unloading, repeating three times. As shown in Fig2.9a, the yield stress of subsequent loading increased approximately to the flow stress previous loading, suggesting that the materials work hardened during each loading. The dark-field image and corresponding diffraction pattern shown in Fig2.9d confirm that the materials remains amorphous, while the magnified bright-field images shown in Fig2.9c indicates that no shear bands were formed in the necked region after plastic deformation.

In order to explain the deformation mechanism responsible for the homogenous deformation and work hardening, Jang and Greer introduced a competing mechanism between localised shear banding and homogeneous flow and the contribution of each process to the overall deformation is different with different sample size. Similar to the Griffith's crack-propagation criterion, the stress required to activate a pre-existing shear band to fracture is[57]:

$$\sigma=\sqrt{\frac{2\sqrt{2}\Gamma E}{ad}} \tag{2.5}$$

Where Γ is the energy per unit area of shear band, E is Young's modulus, a is the aspect ratio height over diameter and d is the diameter. As shown in Fig2.10, the shear band activation stress gradually increases with decreasing specimen diameter. The stress necessary to initiate homogenous flow is independent of sample size and is in the range of the elastic limit at room temperature and ideal strength (~E/30). Therefore, there should be a critical diameter, d^* (shown as the intersection of the two curves in Fig2.10), where the deformation mechanism transfers form shear banding to homogeneous flow. When the sample size $d > d^*$, the material fails by localised shear-band propagation, as the stress required for shear-band propagation is lower than the stress required for homogeneous flow. When the sample size $d < d^*$, the stress required for homogeneous deformation is too low to activate the pre-existing embryonic shear band, so homogeneous deformation prevails. As a result of work hardening the flow stress increases gradually until the shear-band propagation stress is reached and the material fails. In order to calculate d*, Γ is estimated to be ~11 Jm^{-2} by equating the elastic energy exerted on the column ($\pi\sigma\varepsilon r^2 h/2$) with the increase in shear band energy ($\sqrt{2}\,\pi r^2\Gamma$)[57]]. The d* is calculated to be between ~30 and 100nm by using Γ=11 Jm^{-2} , a=8, which equates well with the observation.

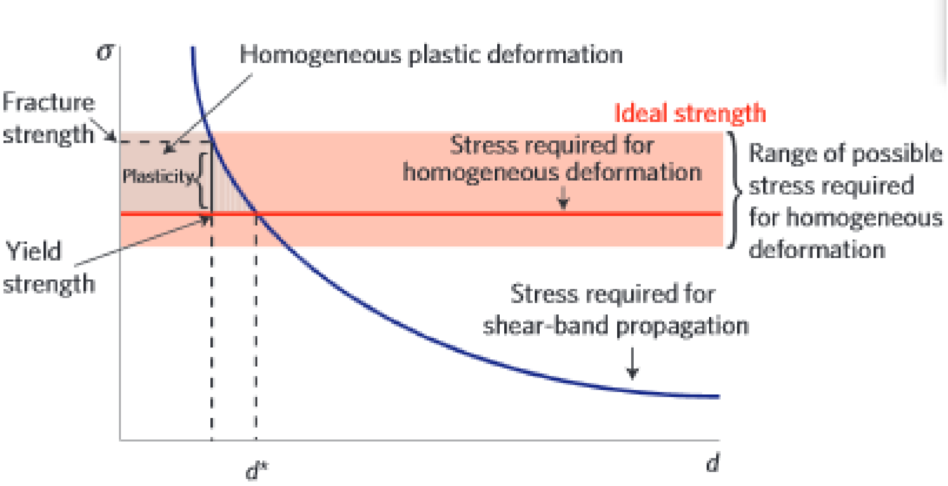

Fig2.10 Diagrammatic sketch of the applied stress necessary to initiate a shear-band motion versus homogeneous flow as a function of sample size, d[53].

Tonnies et al.[93] further extended the study of the size-introduced brittle-to-ductile transition of metallic glass at small scales. Their results suggest that the transition in flow mode is rate dependent but there is no change in atomistic deformation mechanism (shear banding). As shown in Fig2.11(a), for the sample larger than 400nm in diameter, a very clear transition between elastic and plastic regime is observed at a stress of about 1.1-1.2GPa and strain jump during plastic deformation is also seen, which is believed to correspond to the intermittent kinetics of shear banding [98, 99], while for the sample smaller than 300nm in diameter the material yields at much lower stress and strain jumps are absent. Fig 2.11 (b) and (c) display the rate sensitivity of loading rate covering a range of 4 to 5 orders of magnitude. However, for metallic glass at macroscopic scale shows negligible or apparent negative strain-rate sensitivity because of dynamic velocity weakening during inhomogeneous flow [52]. It should be noted that the stress rate can be directly translated into a strain rate. As shown in Fig2.11 (b) and (c), with a decrease of stress (strain) rate, the unexpected change of elastic slope is observed and certainly not due to the size-dependent elasticity.

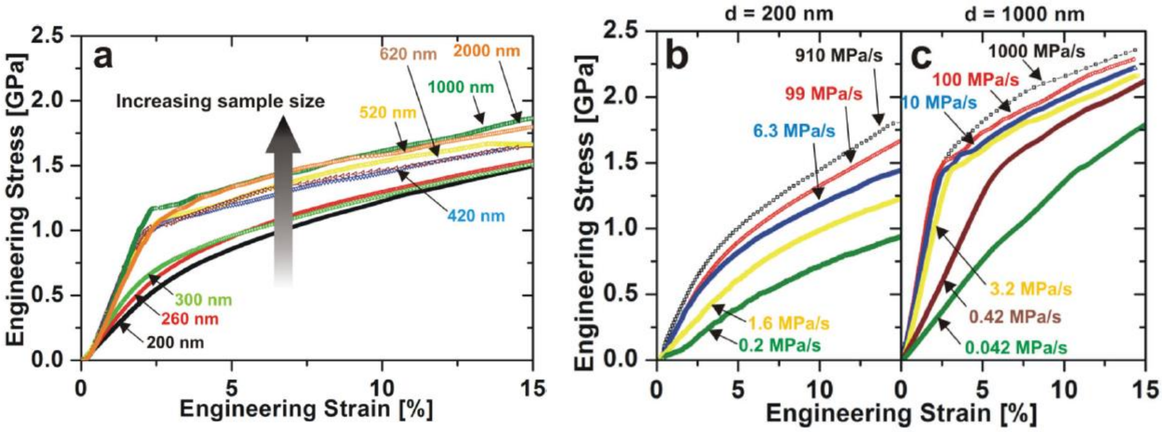

Fig2.11 (a) Engineering stress train curves as a function of specimen size. (b) and (c) engineering stress strain curves as a function of stress rate with column diameter of (b) 200nm and (c)1000nm[93].

In order to further quantify the rate dependence, they calculated the strain-rate sensitivity, m for all tested columns with size of 200nm and 1000nm. The strain-rate sensitivity exponent m is calculated via:

$$\mathrm{m} = \frac{\mathrm{d}\log(\sigma_\mathrm{f})}{\mathrm{d}\log(\dot{\varepsilon})}\bigg|_{\varepsilon_\mathrm{pl}=5\%} \tag{2.6}$$

Here σ_f is the flow stress obtained at the column top where plastic deformation initiates, and $\dot{\varepsilon}$ is the strain rate. The strain-rate sensitivity, $\mathrm{m} = 0.05$ is obtained by a linear fit in a diagram of flow stress (σ_f) versus strain rate ($\varepsilon_\mathrm{pl} = 5\%$), regardless of applied stress, sample size and deformation mode. Although an increase in scatter in the low strain rate regime is observed in Fig2.11a, there is no change in m within a constant sample size series as well as in different sample sizes. Thus, apparently, the samples with different size have different flow response at constant testing temperature, but their underlying atomic deformation mechanism is same, because a change in the atomic deformation mechanism will lead to a change in m[100].

The rate-size deformation map shown in Fig2.12b provides empirical boundaries between the intermittent and homogeneous flow. As can be observed from Fig2.12b, the transition between the intermittent and homogenous flow is highly dependent on the applied rate, which leads to the homogenous regime inaccessible with conventional techniques at larger diameter. The transition rate, $\dot{\varepsilon}_{pl}$, was evaluated at 5% strain, and yields a power-law with a very similar exponent as the stress-rate boundary.

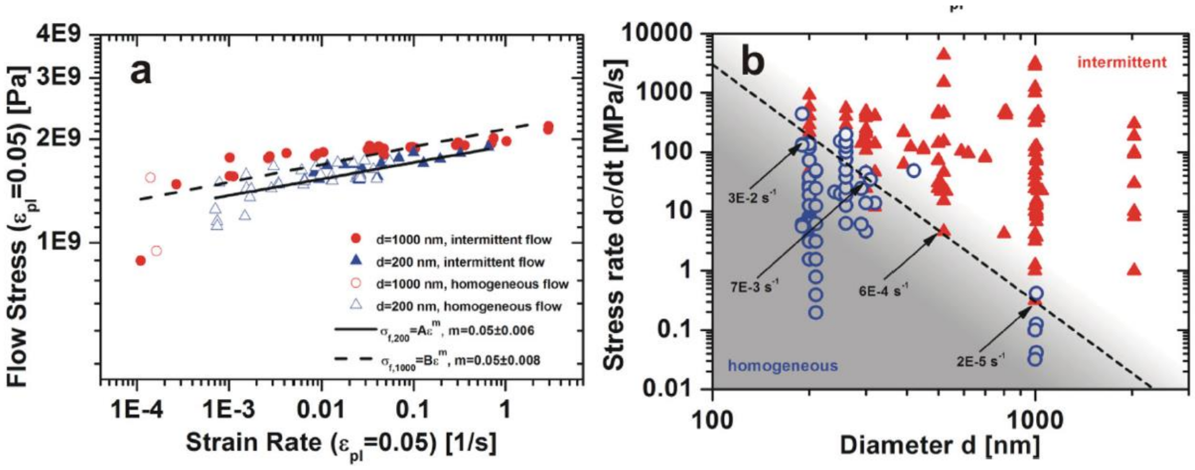

Fig2.12 (a) Flow stress versus strain rate at a plastic strain of 5%. (b) A rate-size deformation map of intermittent versus homogenous flow (at least 300 sample were investigated). Plastic train rates shown around the transition line are indicated for different sample size [93].

In order to further explore the deformation mechanism of metallic glass at small scale, the shear-band morphology was studied with same stress rate range (10-100MPa/s). The shear band spacing, d_{SB}, were evaluated via:

$$d_{SB}=\cos(\alpha)\times\frac{l}{x} \tag{2.6}$$

Here l is the height of the deformed region along the loading axis; x is the number of shear bands observed for each sample, α is the angle between the loading axis and the shear-band normal. The reported angular value, $\alpha=50\pm4^{o}$ is adopted[57]. As summarized in Fig2.13a, a linear trend, d_{SB}=0.09d, between the shear-band spacing and the sample diameter is observed. The shear-band offset,o_{SB}, was also evaluated with $o_{SB}=\frac{w}{\cos(\alpha)\times x}$, where w is the increase of the width at the top of the deformed sample. As shown in Fig2.13a, o_{SB} scales similarly with d_{SB}. The decrease of o_{SB} with a decrease of sample size can be understood directly when considering that the shear-band velocity scales with sample size as well [96]. The shear-band velocity difference in the size range covered in Fig2.13a is within a factor of three when calculated directly from the time-displacement data. This correlates well with the o_{SB} scaling, and indicates that it is due to the lower shear-band propagation velocity in smaller sample.

It is evident to see that in Fig2.14a, the shear-band spacing, d_{SB}, decreases with a decrease of sample size, which approaches the widely accepted length scale itself (10-20nm)[101]. The shear-band affected volume fraction $V_{f,SB}$ ($V_{f,SB}=\frac{t_{SB}}{0.09d}$, here t_{SB} is the shear − band thickness) is shown in Fig2.13b for 3 different assumption of shear-band thicknesses. It is clearly shown that the volume fraction of materials in the shear-band zone approaches unity in very small samples, which is independent of the value of shear-band thickness. The shear-band spacing of 500nm metallic glass columns is roughly twice the shear-band thickness, as shown in Fig2.13a, which indicates a potential interaction of neighbouring shear bands, as suggested by several reports in the framework of self-organized critical behaviour of inhomogeneous flow of metallic glass [102].With a decrease in sample size, the shear-band affected volume overlap, leading to deformation into the entire sample. Therefore, it is natural to see a transition between intermittent to homogeneous flows, although the underlying deformation mechanism is still dominated by activation and propagation of shear bands. Considering that the material in a shear band is in a structurally state comparable to that close to the glass transition, as observed from shear-band dynamic work [98, 103, 104] and modelling [105-107], it is natural to observe a smooth stress-strain response of a sample with a major volume fraction of shear-band material. The structural-state similarity of materials between the shear-band affected area and glass transition can be further confirmed by the comparing strain-rate sensitivity of $\mathrm{m} = 0.05$ with the known bulk values. The results indicate that the overall mechanical response of the deformed small-scale samples is very similar to the material at temperature very close to $\mathrm{T_g}$. With a few tens of degree below $\mathrm{T_g}$, the strain rate sensitivity, m, obtained from bulk testing at a strain rate of $\sim 10^{-3}\mathrm{s}^{-1}$, decreases from the value around 0.7-0.9 at $\mathrm{T_g}$ to 0.1-0.2[108-110] and further decreases to ± 0.001 at room temperature[52, 100].

The rate-dependent critical diameter, at which the apparent homogenous flow is observed, increases with a decrease in strain rate. As discussed above, when homogeneous plastic flow occurs for small-scale columns, shear-band spacing approaches the shear-band thickness. The homogeneous plastic flow observed in a $1\mu\mathrm{m}$ column compressed at a strain rate of $1\times 10^{14}\mathrm{s}^{-1}$ can be understood with an increase in the effective shear-band nucleation per unit strain with a lower strain rate. Given the condition that the deformation of metallic glass is thermally activated at all temperature, it is not surprising that, at ambient conditions, a decrease in strain rate leads to higher shear-band density [111, 112].

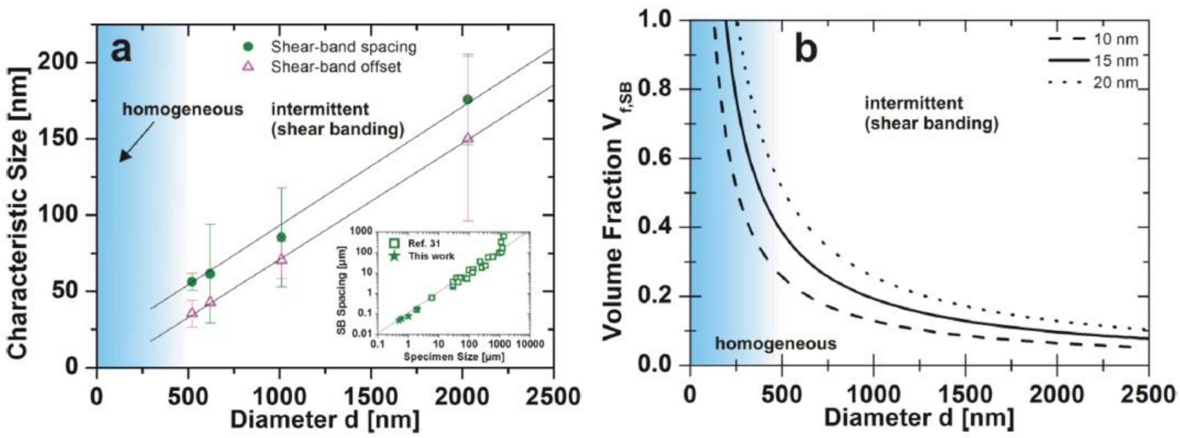

Fig2.13 (a) Shear-band spacing and offset versus sample size (diameter). (b) The volume fraction of shear-band affected materials as a function of sample size (diameter)[93].

2.4 Bulk metallic glass matrix composites

Despite the various attractive properties of BMGs that have been identified, there are two primary limitations for their widespread applications [2, 3, 52, 113]: (1) rapid cooling rate (typically 100-$10^6 \mathrm{k/s}$) is required for generating amorphous alloy, and (2) poor ductility, especially in tension, of the as-cast alloys at temperature below their $\mathrm{T_g}$[52]. The development of multicomponent of alloy compositions has relaxed the limitation of cooling rate [3]. Therefore, the absence of appreciable plastic deformation prior failure is the primary shortfall that restricts these materials from being used as structural materials for safety reasons.

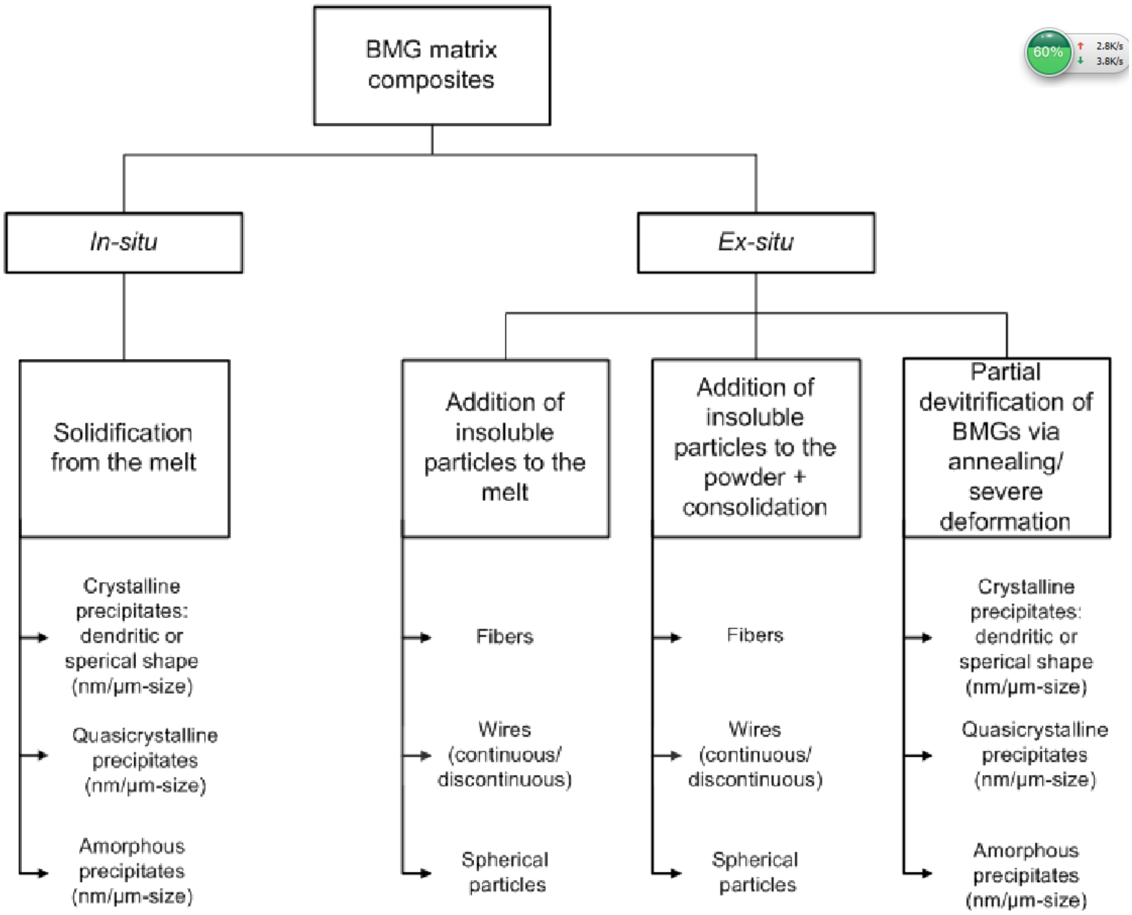

Fig2.14 Classification scheme of BMGCs according to their processing routes [114]

Considering the failure mechanism of BMGs, i.e., formation of localized shear bands, followed by the shear band propagation under loading until one dominant shear band ruptures [52], it is obvious that the objective must be to introduce ductile secondary phase into the MG. The ductile secondary phase acts as an obstruction against the propagation of a shear band and dissipates the fracture energy [14]. Potentially, these obstructions may further dissipate the fracture energy by promoting the emission of more shear bands.

BMGCs are generally produced by ex situ or in situ processing routes, as shown in Fig2.14. Ex situ BMGCs are fabricated by a two-step process by adding a foreign phase, such as fibres, wires, spheres, etc., during a certain stage of the processing (i.e., casting, powder metallurgy, co-processing of BMGs and reinforcement in the supercooled liquid region (SCLR)). In contrast, in situ BMGCs are produced in a single procedure, i.e., directly cooled from the melt by chemical separation of the melt into two different phases (i.e., a amorphous matrix with ductile dendrites or ductile intermetallic). Although there is greater chance to tailor the microstructure and mechanical properties of ex situ BMGCs via adjustments in the type, size and shape of the reinforcement phase, the in situ BMGCs are simpler and more economical fabrication routes. Moreover, one major advantage of the in situ BMGCs is their better interfacial bonding between the reinforcement phase and the matrix, which is very important for the effective shear stress transfer from matrix to the reinforcement phase [14]. Therefore, this thesis concentrated on the recent development of in situ BMGCs.

2.4.1 Design of in situ bulk metallic glass composites

The ideas of a partially crystalline metallic glass or a combination of metallic glass with crystalline inclusions have been around as early as metallic glass [5]. Early annealing experiments to study the glassy structure resulted in partial crystallization, while the development of other metallic glass composites through alloy development progressed very slowly. In the late 1990s, efforts were made to develop “ex situ” composites, where MGs were infiltrated with wires or powders to create two-phase structures [115, 116].Although improvement in compressive plasticity of these ex situ composites were observed over monolithic BMG, ductility in tension was still absent. In 1999, the first ductile in situ BMGCs were developed in Zr-Ti-Cu-Ni-Be by Hays and Kim at Caltech [15], where a secondary Zr solid solution dendrite could grow in equilibrium with a glass forming liquid. This first ductile BMGCs were developed by utilizing chemical decomposition in Zr-Ti-Cu-Ni-Be, considering that Cu, Ni and Be have little or no solubility in the body centered cubic phase (bcc) of Zr-Ti. When partial Cu, Ni and Be were replaced by Zr and Ti, a thermodynamic equilibrium is formed between bcc Zr dendrites and a eutectic liquid. When quenched, the remaining liquid freezes as glassy matrix with crystalline dendrites spaced within [15]. However, although many

BMGCs have been discovered in variety of systems since the first ductile BMGC $Zr_{56.2}Ti_{13.8}Nb_5Cu_{6.9}Ni_{g5.6}Be_{12.5}$ published in 2001, their mechanical properties, i.e., strength and ductility, did not outperform their original alloy [117-121]. As suggested in Refs.[5, 17, 116], there are several responsible reasons including the unique chemistry of Be-bearing composites, mechanical behaviours of the dendrites, size of dendrites and the toughness of the matrix. By 2007, Douglas Hofmann and his colleagues proposed a series of guidelines for creating ductile dendrites reinforced BMGCs[122]: (i) A highly processable BMG system with very sluggish crystallization is required. Zr(Ti)-Be BMG system is optimal for the formation of ductile BMGCs because there are no stable compounds between the constituents and Be, which hinders heterogeneous nucleation of brittle compounds on the dendrites during quenching. (ii) In order to prevent the dendrites from causing heterogeneous nucleation of unexpected brittle phases, it requires an alloy system that has a thermodynamic equilibrium between one stable crystal and the remaining glass-forming liquid [19, 123]. (iii) The dendrites should have a lower shear modulus than the matrix, so during deformation, the softer dendrite can attract the cracks to them, rather than propagating through the glassy matrix alone. (iv)The microstructural length scale such as the interdendritic spacing, λ, should match with the radius of the plastic zone (Rp) of glassy matrix to impede the share band extension. In order to tailor the microstructure, a semisolid processing, an intermediate step during quenching, where the BMGC is held just above the solidus temperature in the two–phase region for coarsening prior to final quenching, was introduced. (v) The fracture toughness of the interface between soft dendrite and glassy matrix must be high enough to prevent crack growth along the interface.

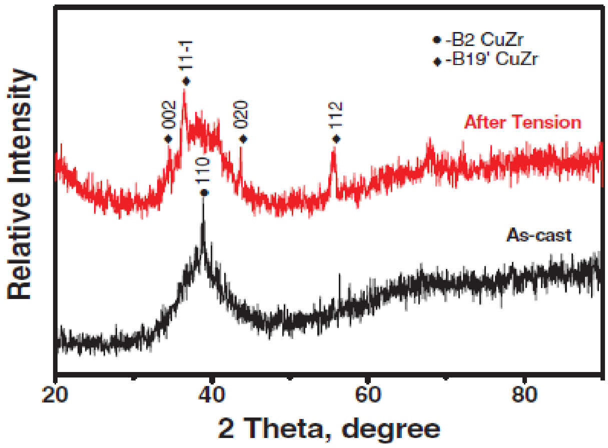

Fig2.15 XRD patterns of the as-cast and deformed CuZrAlCo BMGCs[124].

Although significant improvement of mechanical behaviour has been observed in Zr-(Ti-)Be BMGCs reinforced by ductile h.c.p.Zr/b.c.c.Ti-dendrite solid solution, a macroscopic strain softening phenomenon, accompanying early onset of necking, is always observed in these BMGCs, which severely limits their applications as structural materials[124]. Cu-Zr BMGCs with austenitic precipitates have shown a uniform tensile ductility and pronounced work-hardening due to a diffusionless phase transformation (martensitic transformation) which occurs during straining, known as TRIP effect (transformation-induced plasticity) [124-127] and TWIP effect (Twinning-induced plasticity)[128]. However, it is generally believed that B2 CuZr phase is not stable for most CuZr alloy [129, 130], which only exists in high temperature (988k for CuZr binary alloy) [126] and below it, decomposes into low temperature equilibrium phases, such as $Cu_{10}Zr_7$ and $CuZr_2$. This eutectoid decomposition can be avoided by quenching and the B2 CuZr phase, which undergoes martensitic transformation on straining, can be resolved in room temperature [129, 130]. The XRD patterns shown in Fig2.15 of the as-cast and deformed specimens are typical for a BMGC; crystalline phase peaks superimposed on the amorphous hump correspond to the B2 CuZr phase and B19′ CuZr phase for as-cast and deformed specimens, respectively, implying that the B2 CuZr phase underwent martensitic transformation from B2 structure to a martensitic B19′ structure [124]. From the stress-strain

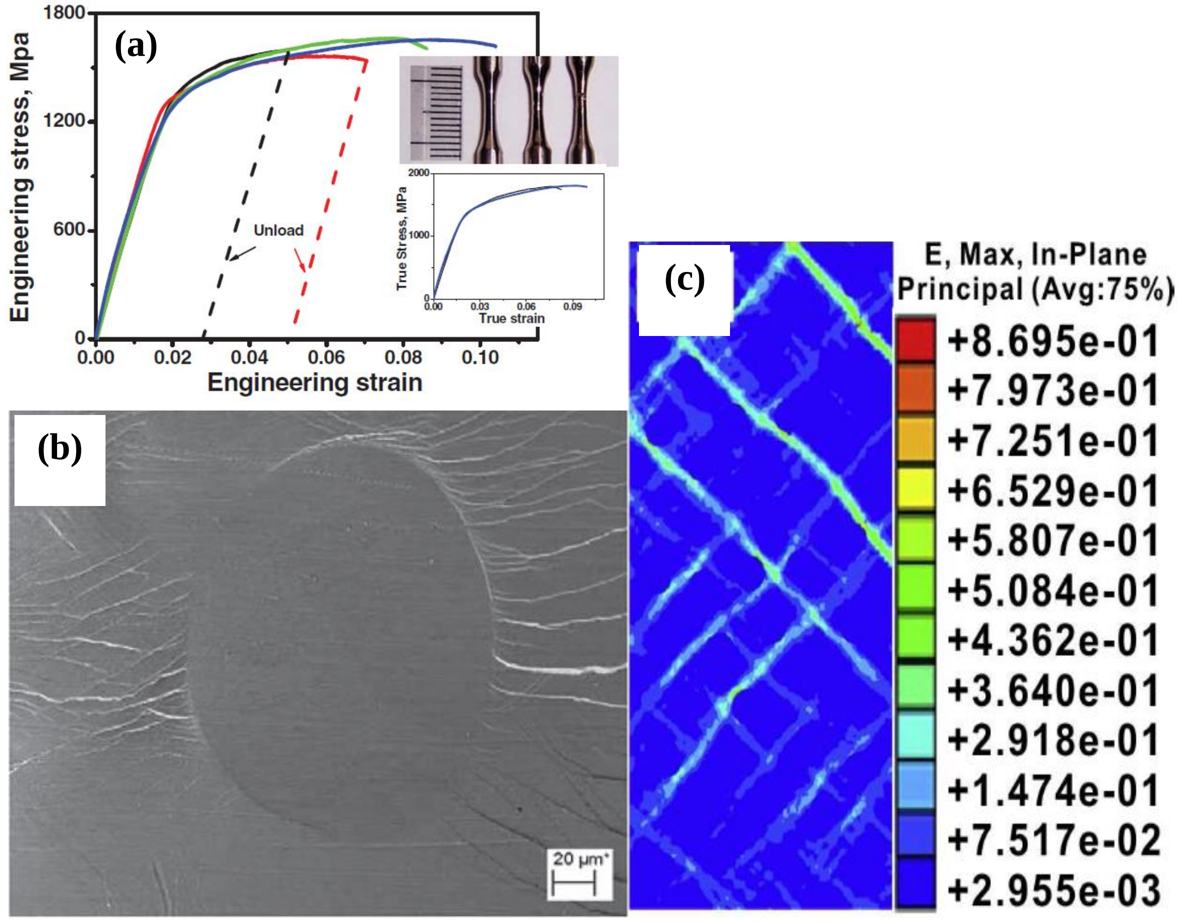

Fig2.16 (a) Tensile stress-strain curves of CuZrAlCo BMGCs, (b) lateral morphology after tension showing the formation of multiple shear bands, and (c) stress distribution induced by the B2 CuZr phase during deformation[124].

curves shown in Fig2.16a, significant work hardening can be seen and as shown in Fig2.16b, multiple shear bands deflect at the interface between the crystals and the glassy matrix and then divide into many shear bands around the B2 CuZr phase. It is believed that the tensile work-softening could be suppressed by the martensitic transformation from B2 to B19, which further improves ductility of the present composites [127]. As reported in Ref [131], martensitic phase transformation of austenite B2 crystals could release the stress concentration around them and hinders free volume accumulation. Consequently, the rapid propagation of shear bands can be hindered, which requires higher stress to motivate the shear bands and consequently prevents work-softening and the early necking [127, 131]. Finite element analysis results shown in Fig2.16c illustrates that the B2 CuZr phase tends to distribute the plastic strain more homogeneously in the glassy matrix during deformation, which is another factor that contribute the improvement of ductility.

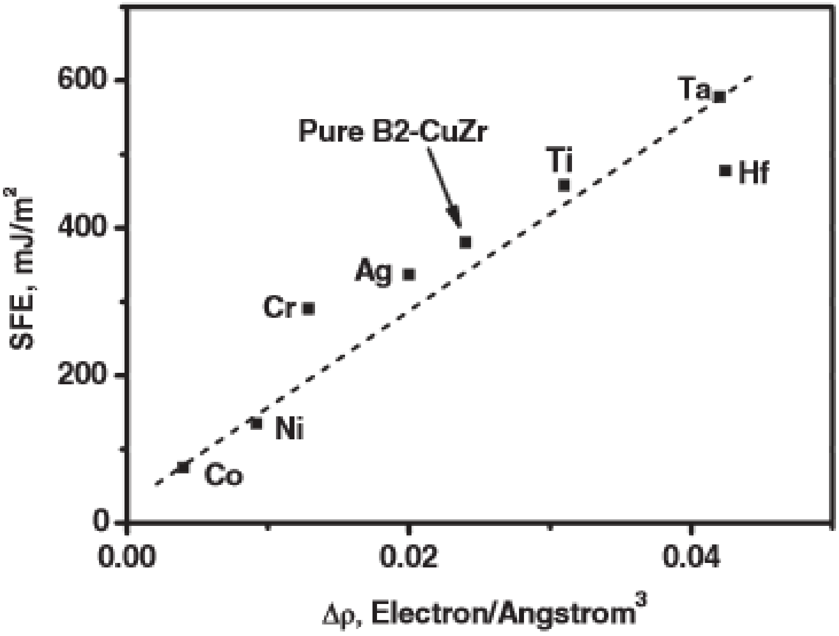

Fig2.17 The value of stacking fault energy as a function of the electronic density charge redistribution on the (011)[100] slip system of B2-CuZr phase microalloyed with different elements [128].

Deformation twinning is one of the main modes for strain energy relaxation, especially for nanocrystalline metals, whose mechanical properties can be effectively improved by tailoring the capability of deformation twining [132-135]. Wu and his colleagues successfully improved the mechanical performance of BMGCs containing austenite particles by tailoring the stacking fault energy [128]. The stacking fault energy, which is the energy cost per unit area by relative displacement of two parts in a crystal through a shift vector across a certain plane, governs the twinning event [136, 137]. In the B2-CuZr phase, (011)[100] is the slip system with minimum stacking fault energy among all the slip system investigated, which is also the most favourable slip direction. Therefore, the stacking fault energy as a function of the shift vector along (011)[100] slip system with or without Ti and Co substitution of Cu on [124, 127] the slipping plane were calculated[128].

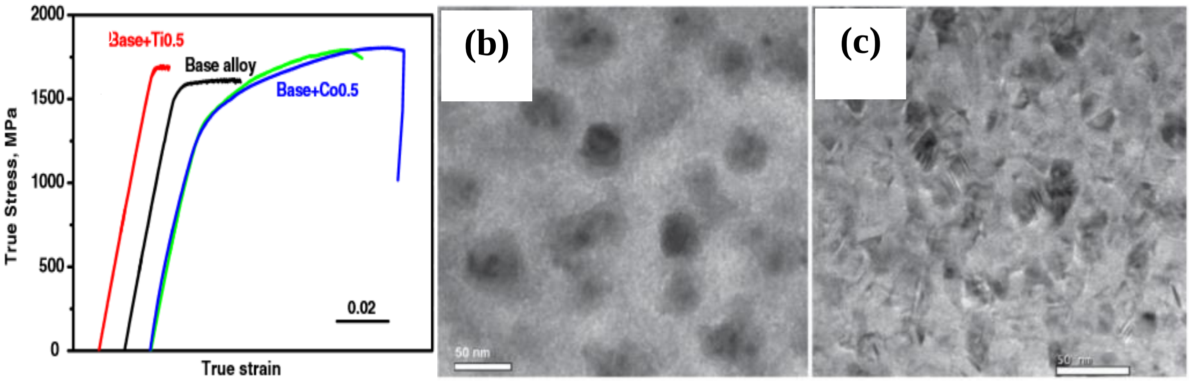

Fig2.18. Tensile stress-strain results of base alloy ($Zr_{48}Cu_{48}Al_4$), $Zr_{48}Cu_{47.5}Al_4Ti_{0.5}$ and $Zr_{48}Cu_{47.5}Al_4Co_{0.5}$ BMGCs. High resolution images of B2 nancrystals in (a) $Zr_{48}Cu_{48}Al_4$ and (b) $Zr_{48}Cu_{47.5}Al_4Co_{0.5}$, respectively [128].

As suggested by Ogata et al. [138, 139], stacking fault energy is strongly related to the charge density change during the formation of stacking fault. Fig2.17 displays the stacking fault values of B2-CuZr alloyed with different elements as a function of the electronic density charge redistribution on the (011)[100] slip system. It clearly shows that the alloying elements that enhance the electronic charge redistribution also increase stacking fault energy. The Co substitution of Cu can drastically decrease the electronic charge redistribution from 0.024 to 0.004 electrons/$\AA^3$ during stacking fault formation, thus reducing stacking fault energy, while the substitution of Cu by Ti enhances the stacking fault energy, thus increasing tacking fault energy [128]. The addition of Co tends to increase the onset temperature of martensitic transformation and decrease the activation energy of austenite B2 phase, facilitating the martensitic transformation [128].

As shown in Fig2.18a, the minor addition of Co can remarkably enhance the tensile ductility and work-hardening capability in comparison with the base alloy and the $Zr_{48}Cu_{47.5}Al_4Ti_{0.5}$. The microstructure of the base alloy and $Zr_{48}Cu_{47.5}Al_4Co_{0.5}$ were analysed by high resolution transmission electron microscopy to further analyse the underlying deformation mechanism. In the base alloy, numerous nanocrytal austenitic B2 particles were observed in addition to micrometre sized B2 structure (Fig2.18b). However, nanosized B2 phase with a distinct characteristic was observed. Stacking fault and twining embryos can be observed from the enlargement of a nanocrystal, Fig2.18b. Selected area diffraction patterns show that the phase slightly away from twin boundary was austenitic B2 phase, while the crystallographic structure around the twin boundaries was identified as the monoclinic B19' structure[128], which means that twinning embryos with B19' martensitic lattice have already nucleated in the quenched Co-containing alloy. It is generally believed that, kinetically, it is often easier to thicken a twin rather than to form a new one. Therefore, deformation twining is easier to be induced due to the pre-exist twin nuclei of Co-containing alloy[140, 141], which promotes the martensitic transformation and improves the plastic stability and macroscopic tensile ductility.

2.4.2 Relationship between microstructure and mechanical properties of in situ BMGCs.

The mechanical properties of monolithic BMGs strongly depend on the sample size, especially for bending test [17, 71, 142]. In bending, plasticity is greatly improved when the characteristic dimension, the plastic zone of a crack tip, R_p, is larger than D/2 (D is the sample thickness)[71, 142]. R_p is a materials length scale related to fracture toughness and for a mode I opening crack, It is expressed as [17],

$$R_p == \frac{1}{2\pi}(\frac{k_{1C}}{\sigma_Y})^2 \qquad (2.8)$$

Where $k_{1C}$is the linear fracture toughness, σ_Y is yielding strength. From brittle to tough BMG materials, R_p varies from ~1μm to ~1mm [17].

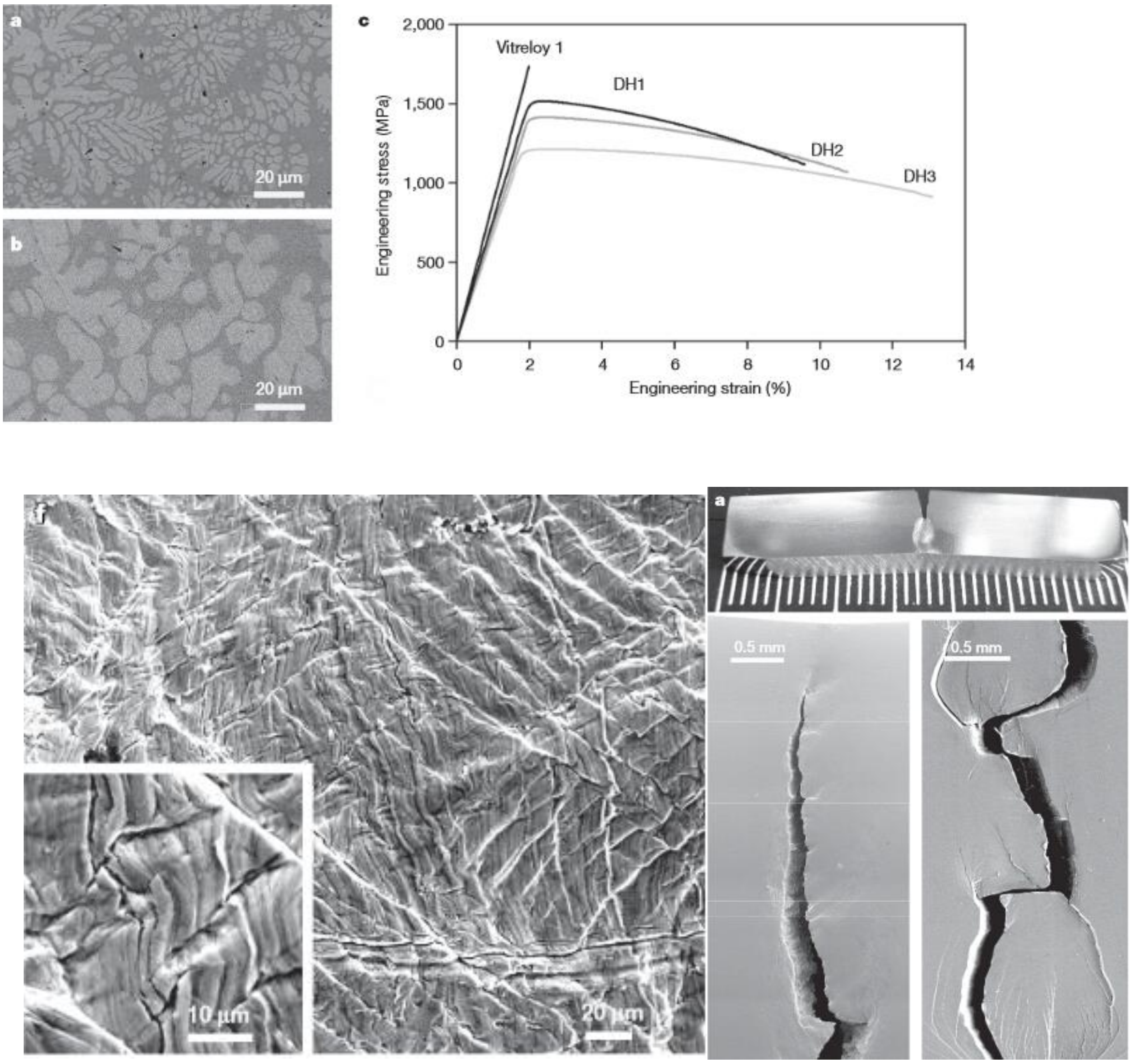

Fig2.19. Backscattered SEM images show the microstructure of $Zr_{36.6}Ti_{31.4}Nb_{7.6}Cu_{5.9}Be_{19.1}$ (DH1) (a) and $Zr_{39.6}Ti_{33.9}Nb_{7.6}Cu_{6.4}Be_{12.5}$ (DH3) (b). (C) Stress-strain curves of DH1, DH2 ($Zr_{38.3}Ti_{32.9}Nb_{7.3}Cu_{6.2}Be_{15.3}$), DH3 and Vitreloy. (d) SEM image shows the tensile surface with high magnification micrograph shown in the inset. (E) Optical image (top) shows a plastic zone of a crack tip in scale of several millimetres and SEM image of an arrested crack in DH1 during a K_{1C} test; the bottom-left side shows an arrested crack in DH1 and bottom-right displays the micrograph of Vitreloy during K_{1C} test[17].

In tension, the strain softening and instability was further enhanced by the opening stress on shear bands, followed by shear band lengthening and slipping without limit. Therefore, the suppression of tensile instability of BMG requires a mechanism to restrict shear band extension. Hofmann proposed a microstructural stabilization mechanism by introducing inhomogeneity in elastic or plastic material properties at a microstructural length, $L \approx R_p$[17]. Shear bands initiated in soft regions can be arrested in surrounding regions with higher yield stress or stiffness.

After analysing a series of SEM images (Fig2.19 a,b), Douglas et al. found both the dendrite size (L≈60-120μm) and inter-dendritic spacing (S≈80-140μm) were in the order of R_p, which is estimated from its K_{1C} ≈70MPam$^{1/2}$ to be ~200μm[17]. The shear bands shown in Fig2.19d have a dominant spacing $d_p \approx$ 15μm, while the length of individual primary shear band (60-100μm) is of the order of L and S, and is somewhat smaller than R_p, but of the order of R_p. The dense secondary shear bands shown in the inset of Fig2.19 d with spacing $d_s \approx$ 1-2 μm are uniformly distributed within primary shear bands. It is found that $d_p \approx L/10$ and $d_s \approx d_p/10$ and similar results was also observed for primary/secondary shear-banding patterns of BMG in bending tests of thin plates [142, 143]. The optical and SEM images shown in Fig2.19F show that extensive plasticity was observed in DH1 and the final crack was arrested before the sample failure. In contrast, the cracks were never arrested in monolithic BMG. The results show that matching the microstructural scale, such as dendrite size and inter-dendritic spacing, with the characteristic length scale R_p (plastic shielding of an opening crack tip) can greatly limit the shear band extension and suppress shear and opening.

2.4.3 Deformation mechanism of in-situ dendrite-reinforced BMGCs in tension

It is generally believed that because of the crystalline dendrite with lower shear modulus distributed within the glassy matrix, the extension of shear band can be effectively arrested by the soft dendrite upon loading, provided that the microstructural features match the plastic zone size, $\mathrm{R_p}$, of the glassy matrix[17]. As a result, tensile instability can be suppressed and significantly improved ductility has been observed. In compression, the severe lattice distortion, local amorphization in the dendrite, and the accumulation of dislocation close to the interface upon training are believed to be responsible for the enhanced ductility and work hardening in compression [144]. However, in tension, most of the dendrite-reinforced BMGCs exhibit softening after yielding instead of work-hardening [17, 123, 145, 146], which indicates different deformation mechanism from the corresponding compression test.

Recently, Qiao et al. conducted a detailed study on the deformation micromechanisms of BMGCs in tension [18, 146]. They did a detailed investigation on the deformation behaviour of $\mathrm{Ti_{46}Zr_{20}Nb_{7.3}V_{12}Be_{17}}$ BMGC and found there are three deformation stages during the tension tests (Fig2.20): elastic, work-hardening and softening, which corresponds to the constitutive relations elastic-elastic, elastic-plastic and plastic-plastic of dual-phase BMGCs[18]. In the first stage, both dendrites and glassy matrix deform elastically. With an increase in stress, the dendrite starts to yield, while the matrix still deform elastically. Work-hardening dominates at this stage. Due to the local severe deformation of individual dendrite, numerous subdivisions formed, divided by shear bands and dense dislocation walls. With further straining, both the dendrite and glassy matrix deform plastically. At this stage, dendrite fragmentation continues and multiplication of shear bands occurs within the glassy matrix accompanied by impediment of dendrites. Local necking occurs and strain softening dominates.

The super elongation before fragmentation of the individual dendrite, rather than local crystallization within the glassy matr-

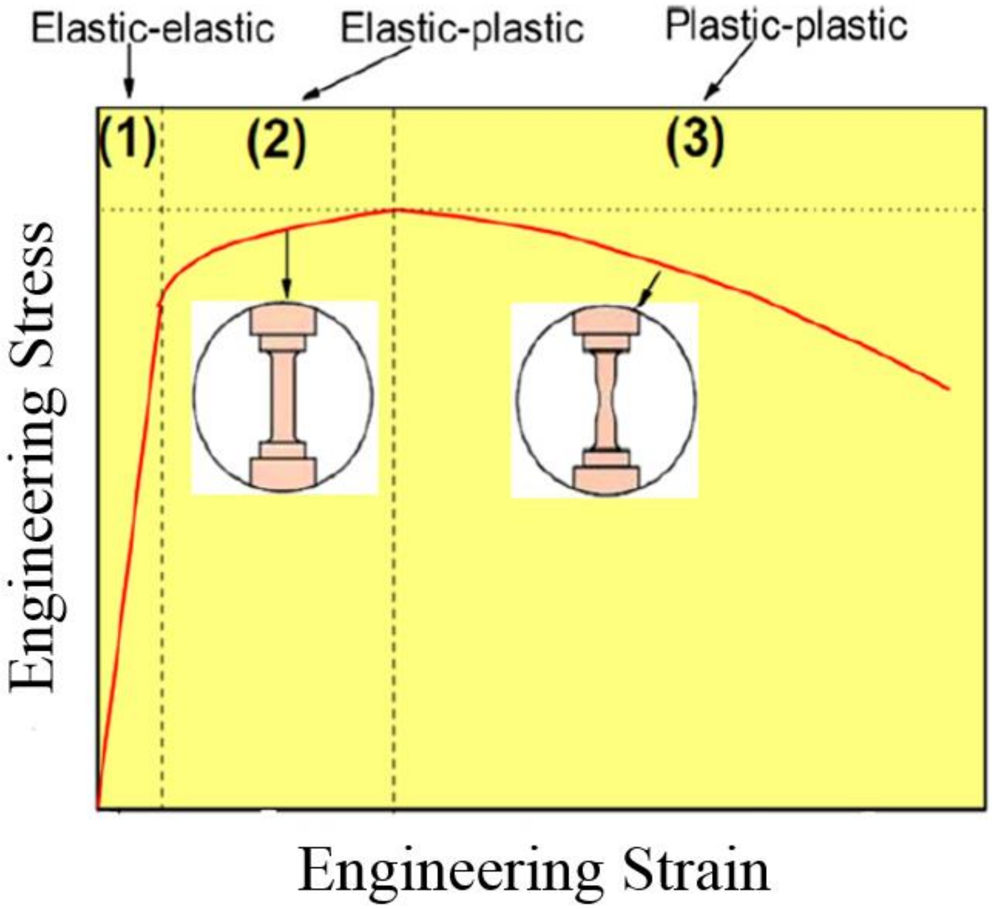

Fig2.20 Schematic Stress-strain curves of BMGCs illustrating 3 stages in tension: elastic, work-hardening and softening [18].

-ix and/or atom debonding around the interface, accounts for the high tensile ductility. They suggested that the super elongation before fragmentation of individual dendrite resulted from subdivisions divided by the dense dislocation walls or shear bands, leads to the macroscopic tensile ductility. Many interface sites were also analysed to check whether debonding occurs or not after tension. No atomic debonding was found after deformation, indicating good structural coherence of the interface. Dislocation, lattice distortions and local amorphization were observed as well at the site in the dendrite near the interface. After glassy matrix yielding, the matrix usually exhibits softening [78], accompanied by the formation of shear bands. Therefore, the tensile stress decreases and the deformation in this plastic-plastic stage is characterized by an interaction between the deformation structure in dendrites, such as dislocations and lattice distortion, and shear bands. The work-hardening capacity of BMGCs strongly depends on the plastic strain of dendrites and the yield strength of the glassy matrix [18]. The homogenous deformation (work-hardening) is vital for BMGCs use as structural materials [147]. The yielding strength of the glassy matrix decides the tensile strength of BMGCs, as an indicator of the capacity of work-hardening.

2.5 Possibility to design in-situ-cast nanostructured alloys from CuZr alloy system with high glass forming ability

2.5.1 Introduction

Since nanocrystalline materials were first defined by Gleiter[148, 149], the study of nanostructured materials (NMs) has flourished over the last two decades. As indicated from the name, NMs are single or multi-phase polycrystalline materials with grain size in the range of 1×10^{-9}~250×10^{-9}m [150]. Above the upper limit of this regime, the materials with grain size from 250nm to 1000nm are often referred to as ultrafine grain materials. In comparison with coarse-grained polycrystalline materials with grain size usually in the range of 10-300μm, NMs are characterized by a large volume fraction of grain boundaries [151], which greatly influence their mechanical, physical and chemical properties. Many superior properties can be observed in NMs in comparison with conventional polycrystalline materials [150], such as increased strength and hardness, improved toughness, higher specific heat, enhanced diffusivity, superior soft magnetic properties and enhanced thermal expansion coefficient.

Generally speaking, these nanometre scale features are introduced by either a two-step approach, in which nanoparticles or powders with nanoscale grains are first synthesized, followed by consolidation to bulk materials with nanoscale or ultra-fine grains [152, 153], or a one-step approach such as electro-deposition[135, 154], severe plastic deformation, e.g. high pressure torsion[155], equal channel angular pressing[156], surface mechanical attrition treatment[157], cryomilling (rolling at liquid nitrogen temperature)[147]. NMs produced by the two-step approach often have defects, such as porosity or cracks that results in very low ductility [158]. In comparison, severe plastic deformation, such as equal channel angle extrusion (ECAP) and high pressure torsion, can synthesize flaw-free NMs. However, even these flow-free NMs also exhibit a very low uniform elongation [147]. The large atomic defect density in the grain interior and at grain boundaries after severe plastic deformation tends to hinder dislocation gliding and multiplication during plastic deformation [159]. Although subsequent heat treatments can to some extent relieve these numerous atomic defects, after heat treatment the dislocations tend to accumulate around grain boundaries [159]. Zhao et al. observed that[160], after tensile testing, dislocation density of ECAP-pressed Cu reduced from 4.3×10^{14} to $3.0\times 10^{14}\ \mathrm{m}^{-2}$, indicating that the poor dislocation accumulation capacity is responsible for the early necking (negligible working hardening) of nanostructured alloys. Currently, the most common methods to produce NMs are inert gas condensation, mechanical alloying, electrodeposition, crystallization from amorphous solids and severe plastic deformation [150].

2.5.2 Deformation behaviour and toughening approaches for nanocrystalline alloys

The strength and ductility of materials are governed by their deformation mechanism, which in turn are determined by their microstructure [158]. NMs usually have high strength but relatively low ductility at ambient temperatures [150]. The low ductility has become the most crucial challenge in NMs [161]. One can view the high strength and poor ductility observed in NMs as a result of severe constraints on dislocation activities [162], which results in the lack of work hardening mechanism due to their low dislocation accumulation capability. Dislocations are generated from one side of grain boundaries and disappear at another, leaving no dislocation to accumulate inside the grain interior during plastic deformation [158]. The high value of work hardening rate is essential for uniform elongation because it helps delay the onset of localized deformation, such as shear bands, where very large strain have been concentrated [158]. Work hardening is caused by the accumulation and interaction of dislocations, which creates obstacles to further dislocation propagation, thus requiring high stress for further deformation [162]. Therefore, in order to make mutually exclusively properties (such as strength and ductility) coexist in one material, one possible solution is to find strengthening features that not only impede dislocation motion but are also able to accommodate plastic deformation. In recent years, various approaches have been reported to improve the ductility and toughness of NMs, such as bimodal grain size [160], nanopreciptates[163, 164], and nanotwins[165]. Among these, nanotwinned structures are the most widely pursued and studied because twin boundaries possess specific interactions with the dislocations. Twins can act as a barrier to dislocation motion in a manner similar to conventional grain boundaries or precipitates to enhance the strength, while at the same time, twins provide a slip system which could improve the ductility [165, 166]. These pre-existing twins are generally observed in electrodeposited thin films of nanostructured Cu or nanostructured Cu fabricated by inter-gas condensation followed by compaction [160].

When the grain size is at the nanoscale, the mean free path of dislocations emitted from grain boundary source is severely limited by the grain size and therefore dislocation reactions, cross slip, and other mechanisms of dislocation multiplication are effectively prohibited[162, 167]. Molecular dynamics simulations suggest that during plastic deformation of single-phase NMs, the dislocations generated at grain boundary sources can run freely until they are absorbed into the opposite grain boundary, causing dislocation starvation[162]. In order to enhance the dislocation accumulation and multiplication capability of single-phase NMs, one possible approach is to introduce much smaller nanoscale precipitates in grain interior. Zhao and colleges introduced nanoscale second-phase particles into nanostructured Al alloy matrix by low temperature ageing after severe plastic deformation at liquid nitrogen temperature, which doubled the uniform elongation, while further improving, rather than sacrificing, its yielding strength [147]. The high resolution images show that, after tensile test, there is no change in the dislocation density at the edges of η′ and η particles, indicating that dislocations are most likely emitted by the mismatch at the interface between matrix and nanoprecipates. During plastic deformation, these dislocations cut through coherent G-P zones and accumulated around these nanoprecipitates. Consequently, dynamic recovery during deformation is significantly hindered and increased dislocation accumulation capability is observed.

2.5.3 Development of nanostructured materials with in-situ composite structure

Localised shear banding instead of dislocation slip is the main deformation mechanism in metallic glasses due to their long-range disordered structure [2, 4, 12].The localized deformation mode is attributed to the lack of strain hardening mechanism in amorphous alloys, which results in room-temperature brittleness and strain softening. However, this challenge has been addressed recently via development of BMGCs consisting of soft crystalline dendrites embedded in amorphous matrix [17, 19]. More interestingly, He et al. successfully applied this idea to create nanocrystalline materials with an in-situ composite structure, consisting of nanocrystalline matrix and micrometre scale dendrites [20]. As shown in Fig2.21, Ti (Ta,Sn) solid solution dendrites formed within the nanocrystalline matrix. During plastic deformation, these dendrites serve as blocks and to slow down and stabilize shear banding, suppressing any shear bands that form uncontrollably across the entire sample, which result in catastrophic failure. Consequently, this alloy showed a promising combination of high strength, pronounced strain hardening, and large plastic strain in compression and multiple shear bands were observed after test.

This work has several significant implications for the development of nanocrystalline materials [20]. First, these bulk NMs are fabricated by directly casting from the melt. Currently, NMs are generally fabricated by nanocrystalline powder consolidation, or by severe plastic deformation to decompose large grain in a conventional material, or electrodeposition to produce foils. In comparison with the directly casting approach, these processes are either costly or introduce defects, such porosity and impurity. Electrodeposition can produce dense materials, but it can only produce in the form of a thin foil.

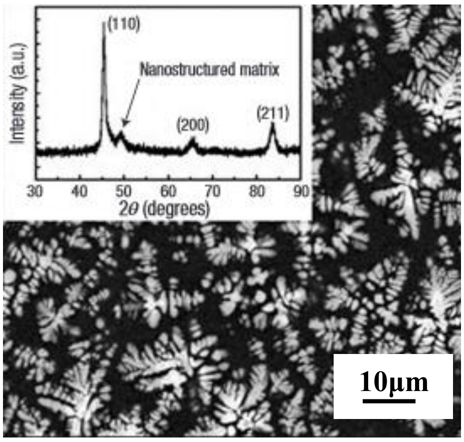

Fig2.21 Back scattered electron image of $Ti_{60}Cu_{14}Ni_{12}Sn_4Ta_{10}$ alloy showing an in situ formed β -Ti (Ta,Sn) dendrite/nanostructured matrix composite microstructure; inset: corresponding XRD pattern presenting the main peaking of β-Ti (Ta,Sn) dendrite[20].

2.5.4 Feasibility study to develop in-situ-cast nanostructured CuZr alloys by introducing diffusional growth restriction

Effective control of phase growth during material synthesis and processing is vital to achieve desired properties for materials [168-170]. Recently, Chen et al. [168] reported that they successfully controlled the fast phase growth by introducing nanoparticles which can spontaneously assemble on the fast-growing phase during cooling. After nucleation, the self-assembly nanoparticles forms a thin layer on the growing nuclei, which limits the diffusion for the further growth of the nuclei. The restriction of diffusion by the nanoparticle layer can lead to the remaining melt becoming sufficiently supercooled/supersaturated, which enables continuous nucleation in the remaining melt, leading to ultrafine structure of the alloy.

In the current work, the objective was to introduce diffusional growth restriction during the solidification to fabricate in-situ-cast NMs by appropriate choice of alloying elements and composition in CuZr alloys. The CuZr system has received extensive attention as a metallic glass largely because of the strong compositional dependence of its glass forming ability coupled with the alloy's ability to yield adequately large amorphous samples to facilitate experimental study [127, 171, 172]. Therefore, significant research has been conducted to explore the mechanism of enhanced glass forming ability in certain compositions of CuZr system. Mendelev et al. [172] conducted molecular dynamics simulations of diffusion in CuZr alloys in their equilibrium liquid and supercooled liquid states. Their simulations reveal that the atom mobility of both copper and zirconium strongly depends on composition and both elements exhibiting minimum diffusivities at ~ 70 at.% Cu, which is very close to the best glass forming composition ($Cu_{64.5}Zr_{35.5}$)[171]. As shown in Fig2.22, the atom mobility of both Cu and Zr significantly depends on the concentration of Zr. At 1100k, the atom mobility of Cu and Zr are at least slowed by one magnitude [172].

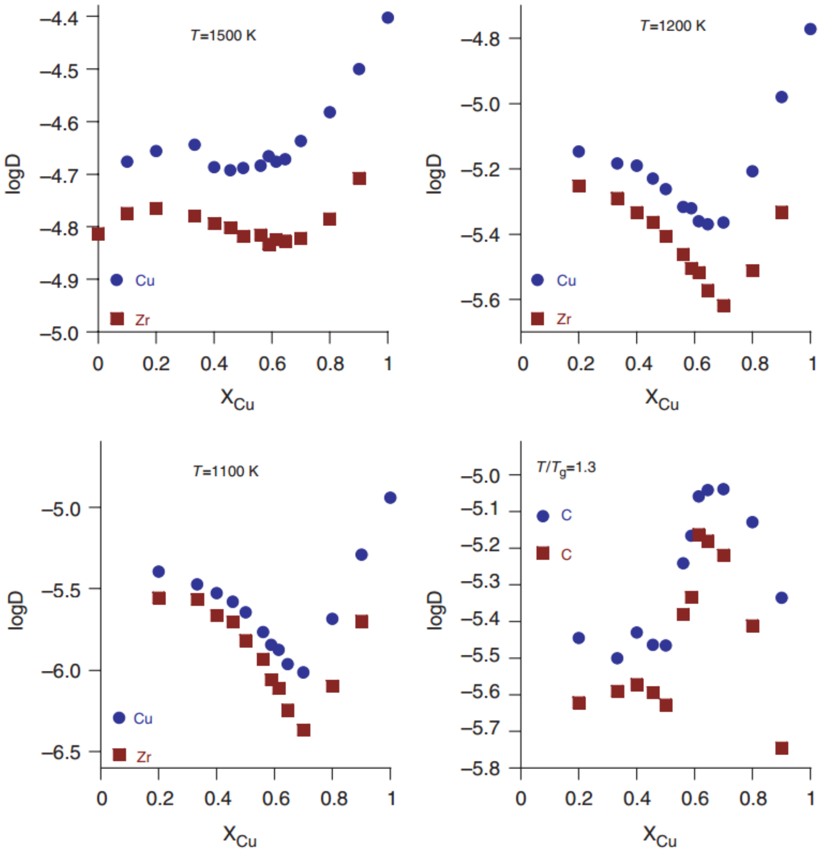

Fig2.22 (a–c) Diffusivities (cm^2s^1) of Copper and Zirconium atoms Cu_xZr_{1-x} supercooled melt as a function of copper concentration at different simulation temperatures. (d) Diffusivities (cm^2s^1) of copper and Zirconium at a temperature ratio of T/ T_g =1.3[172].

Zirconium has negligible solubility in the equilibrium face centred cubic (f.c.c.) Cu (the maximum zirconium solubility in copper is 0.12 at.% at 972°C)[173, 174]. The current work, we try to design in-situ-cast nanostructured CuZrTi alloys using the following two compositions ($Cu_{90.5}Zr_{7.5}$ Ti_2 and$Cu_{90}Zr_8$ Ti_2). These two alloys are slightly hypereutectic in chemical composition according to CuZr phase diagram (eutectic point $Cu_{92.8}Zr_{7.2}$) [174]. However, in light of the CuTi phase diagram [175, 176], the eutectic point in the Cu rich corner is around 20at.% Ti, so the alloys ($Cu_{90.5}Zr_{7.5}$ Ti_2 and $Cu_{90}Zr_8$ Ti_2) are substantially hypoeutectic in chemical composition in the CuTi phase diagram. Therefore the primary Cu dendrites tend to solidify first from the melt with 2at.% Ti. The Ti content is fixed at 2at.% because of the following three considerations: (i) the addition of 2at.% Ti is enough to form supersaturated Cu solid solution as the solubility of Ti in Cu is less than 1at% at 500℃; (ii) 2at.% Ti should be enough to effectively stabilize the primary Cu dendrites during solidification without the formation of any coarse CuTi phase. It is believed that a large quantity of Ti atoms are dissolved into the Cu lattice providing significant solid solution strengthening due to the high cooling rate, and are beneficial to the formation of nano-precipitates in β Cu grains. Zr has negligible solubility at the eutectic temperature in the equilibrium f.c.c. Cu and thus is expected to partition preferentially to the remaining liquid during the initial stage of solidification. The remaining liquid then becomes enriched in Zr, which should restrict the growth of primary Cu solid solution due to the poor mobility of Cu and Zr in the remaining supercooled Zr-rich liquid. With the effective diffusional growth restriction exerted by the surrounding melt rich in Zr and the negligible solubility of Zr in Cu (requiring large amount of Zr atoms partitioning for the further growth of Cu), the surrounding melt can gain sufficient undercooling and supersaturation for a continuous nucleation of new nuclei, because the remaining melt can be substantially stabilized by Zr and Ti to further increase the extent of supercooling as observed in CuZrTi bulk metallic glass system[177]. The solidification of ultrafine/nanoscale Cu crystals in the remaining Zr-rich liquid is expected to proceed. The formation of nanometre Cu crystals further leads to the enrichment of alloying elements in the rest liquid, which should freeze into a hard CuZr phase.

2.6 References

[1] W. Klement, R.H. Willens, P.O.L. Duwez, Non-crystalline Structure in Solidified Gold-Silicon Alloys,Nature, 187 (1960) 869-870.

[2] W.H. Wang, C. Dong, C.H. Shek, Bulk metallic glasses ,Mater. Sci. Eng.: R: Rep., 44 (2004) 45-89.

[3] A. Inoue, A. Takeuchi, Recent development and application products of bulk glassy alloys, Acta Mater., 59 (2011) 2243-2267.

[4] A. Inoue, Stabilization of metallic supercooled liquid and bulk amorphous alloys, Acta Mater., 48 (2000) 279-306.

[5] D.C. Hofmann, Bulk Metallic Glasses and Their Composites: A Brief History of Diverging Fields, J. Mater., 2013 (2013)0- 8.

[6] H.S. Chen, Thermodynamic considerations on the formation and stability of metallic glasses, Acta Metall. Mater., 22 (1974) 1505-1511.

[7] A.J. Drehman, A.L. Greer, D. Turnbull, Bulk formation of a metallic glass:$Pd_{40}Ni_{40}P_{20}$, Appl. Phys. Lett., 41 (1982) 716-717.

[8] H.W. Kui, A.L. Greer, D. Turnbull, Formation of bulk metallic glass by fluxing, Appl. Phys. Lett., 45 (1984) 615-616.

[9] A. Inoue, T.Zhang, Al-La-Ni Amorphous Aalloy with a Wide Supercooled Liquid Region, Mater. Trans.JIM, 30 (1989)965-972.

[10] A.Inoue, T.Nakamura,N.Nishiyama,T.Masumoto, My-Cu-Y Bulk Amorphous Alloy with High Tensile Strength Produced by a High-Pressure Die Casting Method, Mater. Trans.JIM, 33 (1992) 937-945.

[11] A.L. Greer, Confusion by design,Nature, 366 (1993) 303-304.

[12] C.A. Schuh, T.C. Hufnagel, U. Ramamurty, Mechanical behavior of amorphous alloys, Acta Mater., 55 (2007) 4067-4109.

[13] P. Lowhaphandu, L.A. Ludrosky, S.L. Montgomery, J.J. Lewandowski, Deformation and fracture toughness of a bulk amorphous Zr–Ti–Ni–Cu–Be alloy, Intermetallics, 8 (2000) 487-492.

[14] M. Ferry, K.J. Laws, C. White, D.M. Miskovic, K.F. Shamlaye, W. Xu, O. Biletska, Recent developments in ductile bulk metallic glass composites, MRS Communications, 3 (2013) 1-12.

[15] C.C. Hays, C.P. Kim, W.L. Johnson, Microstructure Controlled Shear Band Pattern Formation and Enhanced Plasticity of Bulk Metallic Glasses Containing in situ Formed Ductile Phase Dendrite Dispersions, Phy. Rev. Lett., 84 (2000) 2901-4.

[16] F. Guo, H.J. Wang, S.J. Poon, G.J. Shiflet, Ductile titanium-based glassy alloy ingots, Appl. Phys. Lett., 86 (2005) 091907-3.

[17] D.C. Hofmann, J.-Y. Suh, A. Wiest, G. Duan, M.-L. Lind, M.D. Demetriou, W.L. Johnson, Designing metallic glass matrix composites with high toughness and tensile ductility,Nature, 451 (2008) 1085-1089.

[18] J.W. Qiao, A.C. Sun, E.W. Huang, Y. Zhang, P.K. Liaw, C.P. Chuang, Tensile deformation micromechanisms for bulk metallic glass matrix composites: From work-hardening to softening, Acta Mater., 59 (2011) 4126-4137.

[19] D.C. Hofmann, Shape Memory Bulk Metallic Glass Composites,Science, 329 (2010) 1294-1295.

[20] G. He, J. Eckert, W. Loser, L. Schultz, Novel Ti-base nanostructure-dendrite composite with enhanced plasticity, Nat. Mater., 2 (2003) 33-37.

[21] E. Ma, Nanocrystalline materials: Controlling plastic instability, Nat. Mater., 2 (2003) 7-8.

[22] D. Turnbull, Metastable structures in metallurgy, Metall. Trans. A, 12 (1981) 695-708.

[23] J.F. Löffler, Bulk metallic glasses, Intermetallics, 11 (2003) 529-540.

[24] A. Inoue, High Strength Bulk Amorphous Alloy with Low Critical Cooling Rate ,JIM, 36 (1995) 886-895.

[25] R. Busch, W. Liu, W.L. Johnson, Thermodynamics and kinetics of the Mg65Cu25Y10 bulk metallic glass forming liquid, J. Appl. Phys., 83 (1998) 4134-4141.

[26] Z.P. Lu, C.T. Liu, A new glass-forming ability criterion for bulk metallic glasses ,Acta Mater., 50 (2002) 3501-3512.

[27] C.A. Angell, Formation of Glasses from Liquids and Biopolymers, Science, 267 (1995) 1924-1935.

[28] W.L. Johnson, Bulk Glass-Forming Metallic Alloys: Science and Technology, MRS Bull., 24 (1999) 42-56.

[29] A. Inoue, Direct Comparison between Critical Cooling Rate and Some Quantitiative Parameters for Evaluation of Glass-Forming Ability in Pd-Cu-Ni-P alloys, Mater. Trans.JIM, 43 (2002) 1913-1917.

[30] A. Meyer, J. Wuttke, W. Petry, O.G. Randl, H. Schober, Slow Motion in a Metallic Liquid, Phy. Rev. Lett., 80 (1998) 4454-4457.

[31] A. Meyer, R. Busch, H. Schober, Time-Temperature Superposition of Structural Relaxation in a Viscous Metallic Liquid, Phy. Rev. Lett., 83 (1999) 5027-5029.

[32] W.H. Wang, Roles of minor additions in formation and properties of bulk metallic glasses, Prog. Mater. Sci., 52 (2007) 540-596.

[33] D. Xu, G. Duan, W.L. Johnson, Unusual Glass-Forming Ability of Bulk Amorphous Alloys Based on Ordinary Metal Copper, Phy. Rev. Lett., 92 (2004) 245504-4.

[34] E.S. Park, D.H. Kim, Phase separation and enhancement of plasticity in Cu–Zr–Al–Y bulk metallic glasses, Acta Mater., 54 (2006) 2597-2604.

[35] Y. Zhang, J. Chen, G.L. Chen, X.J. Liu, Glass formation mechanism of minor yttrium addition in CuZrAl alloys, Appl. Phys. Lett., 89 (2006), 131904-131906.

[36] N. Chen, L. Martin, D.V. Luzguine-Luzgin, Role of Alloying Additions in Glass Formation and Properties of Bulk Metallic Glasses, A. Inoue, Mater., 3 (2010) 5320-5339.

[37] Y. Zhang, M.X.Pan, D. Q. Zhao, R. J. Wang, W. H.Wang, Formation of Zr-Based Bulk Metallic Glasses from Low Purity of Materials by Yttrium Addition, Mater.Tran.JIM, 41 (2000)1410-1414.

[38] Z.P. Lu, C.T. Liu, J.R. Thompson, W.D. Porter, Structural Amorphous Steels, Phy. Rev. Lett., 92 (2004) 245503-4.

[39] Q. Wang, C.T. Liu, Y. Yang, J.B. Liu, Y.D. Dong, J. Lu, The atomic-scale mechanism for the enhanced glass-forming-ability of a Cu-Zr based bulk metallic glass with minor element additions, Sci. Rep., 4 (2014)4648-5.

[40] Q. Wang, C.T. Liu, Y. Yang, Y.D. Dong, J. Lu, Atomic-Scale Structural Evolution and Stability of Supercooled Liquid of a Zr-Based Bulk Metallic Glass, Phy. Rev. Lett., 106 (2011) 215505-4.

[41] Y.Q. Cheng, E. Ma, H.W. Sheng, Atomic Level Structure in Multicomponent Bulk Metallic Glass, Phy. Rev. Lett., 102 (2009) 245501-4.

[42] M. Leocmach, H. Tanaka, Roles of icosahedral and crystal-like order in the hard spheres glass transition, Nat. Common., 3 (2012) 974-8.

[43] D. Turnbull, Under what conditions can a glass be formed, Contemp. Phys., 10 (1969) 473-488.

[44] D.B. Miracle, A structural model for metallic glasses, Nat. Mater., 3 (2004) 697-702.

[45] H.W. Sheng, W.K. Luo, F.M. Alamgir, J.M. Bai, E. Ma, Atomic packing and short-to-medium-range order in metallic glasses, Nature, 439 (2006) 419-425.

[46] P.H. Gaskell, Similarities in amorphous and crystalline transition metal-metalloid alloy structures, Nature, 289 (1981) 474-476.

[47] Y.Q. Cheng, E. Ma, Atomic-level structure and structure–property relationship in metallic glasses, Prog. Mater. Sci., 56 (2011) 379-473.

[48] M. Chen, A brief overview of bulk metallic glasses, NPG Asia Mater., 3 (2011) 82-90.

[49] J. Schroers, T.M. Hodges, G. Kumar, H. Raman, A.J. Barnes, Q. Pham, T.A. Waniuk, Thermoplastic blow molding of metals, Mater. Today, 14 (2011) 14-19.

[50] Y. Zhao, T. Topping, J.F. Bingert, J.J. Thornton, A.M. Dangelewicz, Y. Li, W. Liu, Y. Zhu, Y. Zhou, E.J. Lavernia, High Tensile Ductility and Strength in Bulk Nanostructured Nickel, Adv. Mater., 20 (2008) 3028-3033.

[51] F.F. Wu, Z.F. Zhang, S.X. Mao, Size-dependent shear fracture and global tensile plasticity of metallic glasses, Acta Mater.,57 (2009) 257-266.

[52] M.M. Trexler, N.N. Thadhani, Mechanical properties of bulk metallic glasses, Prog. Mater. Sci., 55 (2010) 759-839.

[53] D. Jang, J.R. Greer, Transition from a strong-yet-brittle to a stronger-and-ductile state by size reduction of metallic glasses, Nat. Mater., 9 (2010) 215-219.

[54] H. Guo, P.F. Yan, Y.B. Wang, J. Tan, Z.F. Zhang, M.L. Sui, E. Ma, Tensile ductility and necking of metallic glass, Nat. Mater., 6 (2007) 735-739.

[55] J.H. Luo, F.F. Wu, J.Y. Huang, J.Q. Wang, S.X. Mao, Superelongation and Atomic Chain Formation in Nanosized Metallic Glass, Phys. Rev. Lett., 104 (2010) 215503-4.

[56] Z.W. Shan, J. Li, Y.Q. Cheng, A.M. Minor, S.A. Syed Asif, O.L. Warren, E. Ma, Plastic flow and failure resistance of metallic glass: Insight from in situ compression of nanopillars Phys.Rev.B, 77 (2008) 155419-6.

[57] C.A. Volkert, A. Donohue, F. Spaepen, Effect of sample size on deformation in amorphous metals,J. Appl. Phys, 103 (2008) 083539-6.

[58] M. Chen, Mechanical Behavior of Metallic Glasses: Microscopic Understanding of Strength and Ductility,Ann. Rev. Mater. Res., 38 (2008) 445-469.

[59] A.S. Argon, H.Y. Kuo, Plastic flow in a disordered bubble raft (an analog of a metallic glass), Mater.Sci.Eng., 39 (1979) 101-109.

[60] V.V. Bulatov, A.S. Argon, A stochastic model for continuum elasto-plastic behavior. I. Numerical approach and strain localization, Model. Simul. Mater. Sci., 2 (1994) 167.

[61] D. Srolovitz, V. Vitek, T. Egami, An atomistic study of deformation of amorphous metals, Acta Met., 31 (1983) 335-352.

[62] C.A. Schuh, A.C. Lund, Atomistic basis for the plastic yield criterion of metallic glass,Nat. Mater., 2 (2003) 449-452.

[63] M.L. Falk, Molecular-dynamics study of ductile and brittle fracture in model noncrystalline solids Phys.Rev.B, 60 (1999) 7062-7070.

[64] J.S. Langer, Shear-transformation-zone theory of deformation in metallic glasses, Scripta Mater., 54 (2006) 375-379.

[65] M.L. Falk, J.S. Langer, Dynamics of viscoplastic deformation in amorphous solids,Phys.Rev.E, 57 (1998) 7192-7205.

[66] A.S. Argon, Plastic deformation in metallic glasses, Acta Met., 27 (1979) 47-58.

[67] Z.W. Zhu, H.F. Zhang, W.S. Sun, B.Z. Ding, Z.Q. Hu, Processing of bulk metallic glasses with high strength and large compressive plasticity in $Cu_{50}Zr_{50}$, Scripta Mater., 54 (2006) 1145-1149.

[68] T. Mukai, T.G. Nieh, Y. Kawamura, A. Inoue, K. Higashi, Effect of strain rate on compressive behavior of a Pd40Ni40P20 bulk metallic glass, Intermetallics, 10 (2002) 1071-1077.

[69] W.H. Wang, D.W. He, D.Q. Zhao, Y.S. Yao, M. He, Nanocrystallization of ZrTiCuNiBeC bulk metallic glass under high pressure, Appl. Phys. Lett., 75 (1999) 2770-2772.

[70] Y.X. Zhuang, J.Z. Jiang, T.J. Zhou, H. Rasmussen, L. Gerward, M. Mezouar, W. Crichton, A. Inoue, Pressure effects on Al89La6Ni5 amorphous alloy crystallization,Appl. Phys. Lett., 77 (2000) 4133-4135.

[71] R.D. Conner, W.L. Johnson, N.E. Paton, W.D. Nix, Shear bands and cracking of metallic glass plates in bending ,J. Appl. Phys., 94 (2003) 904-911.

[72] A.C. Lund, C.A. Schuh, Yield surface of a simulated metallic glass, Acta Mater., 51 (2003) 5399-5411.

[73] A.S. Argon, L.T. Shi, Analysis of plastic flow in an amorphous soap bubble raft by the use of an inter-bubble potential, Philos. Mag. A, 46 (1982) 275-294.

[74] W.L. Johnson, K. Samwer, A Universal Criterion for Plastic Yielding of Metallic Glasses with a Temperature Dependence Phys. Rev. Lett., 95 (2005) 195501-4.

[75] S.G. Mayr, Activation Energy of Shear Transformation Zones: A Key for Understanding Rheology of Glasses and Liquids, Phys. Rev. Lett., 97 (2006) 195501-4.

[76] M. Zink, K. Samwer, W.L. Johnson, S.G. Mayr, Plastic deformation of metallic glasses: Size of shear transformation zones from molecular dynamics simulations, Phys.Rev.B, 73 (2006) 172203-3.

[77] H. Kimura, T. Masumoto, Deformation and fracture of an amorphous Pd□Cu□Si alloy in V-notch bending tests—I: Model mechanics of inhomogeneous plastic flow in non-strain hardening solid, Acta Met., 28 (1980) 1663-1675.

[78] H. Bei, S. Xie, E.P. George, Softening Caused by Profuse Shear Banding in a Bulk Metallic Glass, Phys. Rev. Lett., 96 (2006) 105503-4.

[79] K.F. Yao, F. Ruan, Y.Q. Yang, N. Chen, Superductile bulk metallic glass, Appl. Phys.Lett., 88 (2006) 122106-3.

[80] D.E. Polk, D. Turnbull, Flow of melt and glass forms of metallic alloys, Acta Met., 20 (1972) 493-498.

[81] F. Spaepen, A microscopic mechanism for steady state inhomogeneous flow in metallic glasses, Acta Met., 25 (1977) 407-415.

[82] P.S. Steif, F. Spaepen, J.W. Hutchinson, Strain localization in amorphous metals, Acta Met., 30 (1982) 447-455.

[83] V.A. Khonik, The Kinetics of Irreversible Structural Relaxation and Homogeneous Plastic Flow of Metallic Glasses, Phys. Status Solidi (a), 177 (2000) 173-189.

[84] F.G. Shi, T.G. Nieh, Y.T. Chou, A free volume approach for self-diffusion in metals, Scripta Mater., 43 (2000) 265-267.

[85] M.D. Uchic, D.M. Dimiduk, J.N. Florando, W.D. Nix, Sample Dimensions Influence Strength and Crystal Plasticity, Science, 305 (2004) 986-989.

[86] J.R. Greer, J.T.M. De Hosson, Plasticity in small-sized metallic systems: Intrinsic versus extrinsic size effect ,Prog. Mater. Sci., 56 (2011) 654-724.

[87] J.R. Greer, W.C. Oliver, W.D. Nix, Size dependence of mechanical properties of gold at the micron scale in the absence of strain gradients, Acta Mater., 53 (2005) 1821-1830.

[88] T. Zhu, J. Li, Ultra-strength materials", Progress in Materials Science, Prog. Mater. Sci., 55 (2010) 710-757.

[89] C.C. Wang, J. Ding, Y.Q. Cheng, J.C. Wan, L. Tian, J. Sun, Z.W. Shan, J. Li, E. Ma, Sample size matters for Al88Fe7Gd5 metallic glass: Smaller is stronger, Acta Mater., 60 (2012) 5370-5379.

[90] B.E. Schuster, Q. Wei, T.C. Hufnagel, K.T. Ramesh, Size-independent strength and deformation mode in compression of a Pd-based metallic glass ,Acta Mater., 56 (2008) 5091-5100.

[91] O.V. Kuzmin, Y.T. Pei, C.Q. Chen, J.T.M. De Hosson, Intrinsic and extrinsic size effects in the deformation of metallic glass nanopillars ,Acta Mater., 60 (2012) 889-898.

[92] J.C. Ye, J. Lu, C.T. Liu, Q. Wang, Y. Yang, Atomistic free-volume zones and inelastic deformation of metallic glasses ,Nat. Mater., 9 (2010) 619-623.

[93] D. Tönnies, R. Maaß, C.A. Volkert, Room Temperature Homogeneous Ductility of Micrometer-Sized Metallic Glass, Adv. Mater., 26 (2014) 5715-5721.

[94] J.C. Ye, J. Lu, Y. Yang, P.K. Liaw, Extraction of bulk metallic-glass yield strengths using tapered micropillars in micro-compression experiments, Intermetallics, 18 (2010) 385-393.

[95] C.J. Lee, J.C. Huang, T.G. Nieh, Sample size effect and microcompression of $Mg_{65}Cu_{25}Gd_{10}$ metallic glass, Appl. Phys. Lett., 91 (2007) 161913-3.

[96] C.Q. Chen, Y.T. Pei, J.T.M. De Hosson, Effects of size on the mechanical response of metallic glasses investigated through in situ TEM bending and compression experiments, Acta Mater., 58 (2010) 189-200.

[97] A. Bharathula, S.-W. Lee, W.J. Wright, K.M. Flores, Compression testing of metallic glass at small length scales: Effects on deformation mode and stability, Acta Mater., 58 (2010) 5789-5796.

[98] R. Maaß, D. Klaumünzer, J.F. Löffler, Propagation dynamics of individual shear bands during inhomogeneous flow in a Zr-based bulk metallic glass, Acta Mater., 59 (2011) 3205-3213.

[99] D. Klaumünzer, R. Maaß, J.F. Löffler, Stick-slip dynamics and recent insights into shear banding in metallic glasses, J. Mater. Res., 26 (2011) 1453-1463.

[100] A. Dubach, F.H. Dalla Torre, J.F. Löffler, Constitutive model for inhomogeneous flow in bulk metallic glasses, Acta Mater., 57 (2009) 881-892.

[101] A.L. Greer, Y.Q. Cheng, E. Ma, Shear bands in metallic glasses,Mater. Sci. Eng.: R: Rep., 74 (2013) 71-132.

[102] B.A. Sun, H.B. Yu, W. Jiao, H.Y. Bai, D.Q. Zhao, W.H. Wang, Plasticity of Ductile Metallic Glasses: A Self-Organized Critical State,Phys. Rev. Lett., 105 (2010) 035501-4.

[103] D. Klaumünzer, A. Lazarev, R. Maaß, F.H. Dalla Torre, A. Vinogradov, J.F. Löffler, Probing Shear-Band Initiation in Metallic Glasses, Phys. Rev. Lett., 107 (2011) 185502-5.

[104] R. Maaß, D. Klaumünzer, G. Villard, P.M. Derlet, J.F. Löffler, Shear-band arrest and stress overshoots during inhomogeneous flow in a metallic glass, Appl.Phys.Lett, 100 (2012) 071904 -4.

[105] F. Shimizu, S. Ogata, J. Li, Yield point of metallic glass ,Acta Mater., 54 (2006) 4293-4298.

[106] A.J. Cao, Y.Q. Cheng, E. Ma, Structural processes that initiate shear localization in metallic glass, Acta Mater. 57 (2009) 5146-5155.

[107] P. Guan, M. Chen, T. Egami, Stress-Temperature Scaling for Steady-State Flow in Metallic Glasses, Phys. Rev. Lett., 104 (2010) 205701-4.

[108] J. Lu, G. Ravichandran, W.L. Johnson, Deformation behavior of the $Zr_{41.2}Ti_{13.8}Cu_{12.5}Ni_{10}Be_{22.5}$bulk metallic glass over a wide range of strain-rates and temperatures, Acta Mater., 51 (2003) 3429-3443.

[109] Y. Kawamura, T. Shibata, A. Inoue, T. Masumoto, Spatiotemporally inhomogeneous plastic flow of a bulk-metallic glass, Scripta Mater., 37 (1997) 431-436.

[110] Y. Kawamura, T. Nakamura, A. Inoue, Superplasticity in $Pd_{40}Ni_{40}P_{20}$ metallic glass, Scripta Mater., 39 (1998) 301-306.

[111] W.H. Jiang, G.J. Fan, F.X. Liu, G.Y. Wang, H. Choo, P.K. Liaw, Spatiotemporally inhomogeneous plastic flow of a bulk-metallic glass, Int. J. Plasticity, 24 (2008) 1-16.

[112] H. Zhang, S. Maiti, G. Subhash, Evolution of shear bands in bulk metallic glasses under dynamic loading, J. Mech. Phys. Solids, 56 (2008) 2171-2187.

[113] M.F. Ashby, A.L. Greer, Metallic glasses as structural materials, Scripta Mater., 54 (2006) 321-326.

[114] J. Eckert, J. Das, S. Pauly, C. Duhamel, Processing Routes, Microstructure and Mechanical Properties of Metallic Glasses and their Composites, Adv. Eng. Mater., 9 (2007) 443-453.

[115] H. Choi-Yim, R. Busch, W.L. Johnson, The effect of silicon on the glass forming ability of the $Cu_{47}Ti_{34}Zr_{11}Ni_8$ bulk metallic glass forming alloy during processing of composites, J. Appl. Phys., 83 (1998) 7993-5.

[116] H. Choi-Yim, R.D. Conner, F. Szuecs, W.L. Johnson, Processing, microstructure and properties of ductile metal particulate reinforced $Zr_{57}Nb_5Al_{10}Cu_{15.4}Ni_{12.6}$bulk metallic glass composites, Acta Mater., 50 (2002) 2737-2745.

[117] Z. Zhu, H. Zhang, Z. Hu, W. Zhang, A. Inoue, Ta-particulate reinforced Zr-based bulk metallic glass matrix composite with tensile plasticity, Scripta Mater., 62 (2010) 278-281.

[118] M.L. Lee, Y. Li, C.A. Schuh, Effect of a controlled volume fraction of dendritic phases on tensile and compressive ductility in La-based metallic glass matrix composites, Acta Mater., 52 (2004) 4121-4131.

[119] H. Tan, Y. Zhang, Y. Li, Synthesis of La-based in-situ bulk metallic glass matrix composite, Intermetallics, 10 (2002) 1203-1205.

[120] C. Fan, R.T. Ott, T.C. Hufnagel, Metallic glass matrix composite with precipitated ductile reinforcement, Appl.Phys.Lett., 81 (2002) 1020-3.

[121] U. Kühn, J. Eckert, N. Mattern, L. Schultz, ZrNbCuNiAl bulk metallic glass matrix composites containing dendritic bcc phase precipitates, Appl.Phys.Lett., 80 (2002) 2478-3.

[122] D.C. Hofmann, W.L. Johnson, in: MSF, Trans. Tech. Publ., (2010)657-663.

[123] D.C. Hofmann, J.-Y. Suh, A. Wiest, M.-L. Lind, M.D. Demetriou, W.L. Johnson, Demetriou and W. L. Johnson, "Development of tough, low-density titanium-based bulk metallic glass matrix composites with tensile ductility, P. Natl. Acad. Sci., 105 (2008) 20136-20140.

[124] Y. Wu, Y. Xiao, G. Chen, C.T. Liu, Z. Lu, Bulk Metallic Glass Composites with Transformation-Mediated Work-Hardening and Ductility, Adv. Mater., 22 (2010) 2770-2773.

[125] C.P. Kim, Y.S. Oh, S. Lee, N.J. Kim, Realization of high tensile ductility in a bulk metallic glass composite by the utilization of deformation-induced martensitic transformation, Scripta Mater., 65 (2011) 304-307.

[126] S. Pauly, J. Das, J. Bednarcik, N. Mattern, K.B. Kim, D.H. Kim, J. Eckert, Deformation-induced martensitic transformation in Cu–Zr–(Al,Ti) bulk metallic glass composites, Scripta Mater., 60 (2009) 431-434.

[127] Y. Wu, H. Wang, H.H. Wu, Z.Y. Zhang, X.D. Hui, G.L. Chen, D. Ma, X.L. Wang, Z.P. Lu, Formation of Cu–Zr–Al bulk metallic glass composites with improved tensile properties, Acta Mater., 59 (2011) 2928-2936.

[128] Y. Wu, D.Q. Zhou, W.L. Song, H. Wang, Z.Y. Zhang, D. Ma, X.L. Wang, Z.P. Lu, Ductilizing Bulk Metallic Glass Composite by Tailoring Stacking Fault Energy, Phys. Rev. Lett., 109 (2012) 245506-5.

[129] J.W. Seo, D. Schryvers, TEM investigation of the microstructure and defects of CuZr martensite. Part I: Morphology and twin systems, Acta Mater., 46 (1998) 1165-1175.

[130] D. Schryvers, G.S. Firstov, J.W. Seo, J. Van Humbeeck, Y.N. Koval, Unit cell determination in CuZr martensite by electron microscopy and X-ray diffraction, Scripta Mater., 36 (1997) 1119-1125.

[131] X.W. Das J.Kim KB, Wei BC, Zhang ZF, Wang WH, et al, Dutile metallic glass in supercooled martensic alloy, Mater. Trans.JIM, 47 (2006) 2606-2608.

[132] K. Lu, L. Lu, S. Suresh, Strengthening Materials by Engineering Coherent Internal Boundaries at the Nanoscale, Science, 324 (2009) 349-352.

[133] X.L. Wu, Y.T. Zhu, Y.G. Wei, Q. Wei, Strong Strain Hardening in Nanocrystalline Nickel, Phys.Rev. Lett., 103 (2009) 205504-4.

[134] Y.H. Zhao, Y.T. Zhu, X.Z. Liao, Z. Horita, T.G. Langdon, Tailoring stacking fault energy for high ductility and high strength in ultrafine grained Cu and its alloy, Appl.Phys.Lett., 89 (2006)121906-3.

[135] E. Ma, Y.M. Wang, Q.H. Lu, M.L. Sui, L. Lu, K. Lu, Strain hardening and large tensile elongation in ultrahigh-strength nano-twinned copper, Appl.Phys.Lett., 85 (2004) 4932-4934.

[136] N. Hatcher, O.Y. Kontsevoi, A.J. Freeman, Role of elastic and shear stabilities in the martensitic transformation path of NiTi, Phys.Rev.B, 80 (2009) 144203-18.

[137] A. Frøseth, H. Van Swygenhoven, P.M. Derlet, The influence of twins on the mechanical properties of nc-Al, Acta Mater., 52 (2004) 2259-2268.

[138] S. Ogata, J. Li, S. Yip, Ideal Pure Shear Strength of Aluminum and Copper, Science, 298 (2002) 807-811.

[139] Y. Qi, R.K. Mishra, Ab initio study of the effect of solute atoms on the stacking fault energy in aluminium, Phys.Rev.B, 75 (2007) 224105-5.

[140] S. Ogata, J. Li, S. Yip, Energy landscape of deformation twinning in bcc and fcc metals, Phys.Rev.B, 71 (2005) 224102-11.

[141] M. Chen, E. Ma, K.J. Hemker, H. Sheng, Y. Wang, X. Cheng, Deformation Twinning in Nanocrystalline Aluminum, Science, 300 (2003) 1275-1277.

[142] R.D. Conner, Y. Li, W.D. Nix, W.L. Johnson, Shear band spacing under bending of Zr-based metallic glass plates, Acta Mater., 52 (2004) 2429-2434.

[143] G. Ravichandran, A. Molinari, Analysis of shear banding in metallic glasses under bending, Acta Mater., 53 (2005) 4087-4095.

[144] J.W. Qiao, Y. Zhang, P.K. Liaw, G.L. Chen, Micromechanisms of plastic deformation of a dendrite/Zr-based bulk-metallic-glass composite, Scripta Mater., 61 (2009) 1087-1090.

[145] F. Szuecs, C.P. Kim, W.L. Johnson, Mechanical properties of Zr56.2Ti13.8Nb5.0Cu6.9Ni5.6Be12.5 ductile phase reinforced bulk metallic glass composite, Acta Mater., 49 (2001) 1507-1513.

[146] J.W. Qiao, T. Zhang, F.Q. Yang, P.K. Liaw, S. Pauly, B.S. Xu, A Tensile Deformation Model for In-situ Dendrite/Metallic Glass Matrix Composites, Sci. Rep., 3 (2013)2816-2821.

[147] Y.H. Zhao, X.Z. Liao, S. Cheng, E. Ma, Y.T. Zhu, Simultaneously Increasing the Ductility and Strength of Nanostructured Alloys, Adv. Mater., 18 (2006) 2280-2283.

[148] H. Gleiter, Nanocrystalline materials, Prog. Mater.Sci., 33 (1989) 223-315.

[149] H. Gleiter, Nanostructured materials: basic concepts and microstructure, Acta Mater., 48 (2000) 1-29.

[150] M.A. Meyers, A. Mishra, D.J. Benson, Mechanical properties of nanocrystalline materials, Prog. Mater. Sci., 51 (2006) 427-556.

[151] E. Arzt, Size effects in materials due to microstructural and dimensional constraints: a comparative review, Acta Mater., 46 (1998) 5611-5626.

[152] K.S. Kumar, H. Van Swygenhoven, S. Suresh, Mechanical behavior of nanocrystalline metals and alloys, Acta Mater., 51 (2003) 5743-5774.

[153] R.W. Hayes, D. Witkin, F. Zhou, E.J. Lavernia, Deformation and activation volumes of cryomilled ultrafine-grained aluminium, Acta Mater., 52 (2004) 4259-4271.

[154] L. Lu, R. Schwaiger, Z.W. Shan, M. Dao, K. Lu, S. Suresh, Nano-sized twins induce high rate sensitivity of flow stress in pure copper, Acta Mater., 53 (2005) 2169-2179.

[155] A.P. Zhilyaev, T.G. Langdon, Using high-pressure torsion for metal processing: Fundamentals and applications, Prog. Mater. Sci., 53 (2008) 893-979.

[156] R.Z. Valiev, R.K. Islamgaliev, I.V. Alexandrov, Bulk nanostructured materials from severe plastic deformation, Prog. Mater. Sci., 45 (2000) 103-189.

[157] T.H. Fang, W.L. Li, N.R. Tao, K. Lu, Revealing Extraordinary Intrinsic Tensile Plasticity in Gradient Nano-Grained Copper, Science, 331 (2011) 1587-1590.

[158] Y.T. Zhu, X. Liao, Nanostructured metals: Retaining ductility, Nat. Mater., 3 (2004) 351-352.

[159] R. Valiev, Nanostructuring of metals by severe plastic deformation for advanced properties, Nat. Mater., 3 (2004) 511-516.

[160] Y.H. Zhao, J.F. Bingert, X.Z. Liao, B.Z. Cui, K. Han, A.V. Sergueeva, A.K. Mukherjee, R.Z. Valiev, T.G. Langdon, Y.T. Zhu, Simultaneously Increasing the Ductility and Strength of Ultra-Fine-Grained Pure Copper, Adv. Mater., 18 (2006) 2949-2953.

[161] H. Kou, J. Lu, Y. Li, High-Strength and High-Ductility Nanostructured and Amorphous Metallic Materials, Adv. Mater., 26 (2014) 5518-5524.

[162] E. Ma, T.D. Shen, X.L. Wu, Nanostructured metals: Less is more, Nat. Mate.r, 5 (2006) 515-516.

[163] Z. Horita, K. Ohashi, T. Fujita, K. Kaneko, T.G. Langdon, Achieving High Strength and High Ductility in Precipitation-Hardened Alloys ,Adv. Mater., 17 (2005) 1599-1602.

[164] S. Cheng, Y.H. Zhao, Y.T. Zhu, E. Ma, Optimizing the strength and ductility of fine structured 2024 Al alloy by nano-precipitation, Acta Mater., 55 (2007) 5822-5832.

[165] L. Lu, X. Chen, X. Huang, K. Lu, Revealing the Maximum Strength in Nanotwinned Copper, Science, 323 (2009) 607-610.

[166] Y.T. Zhu, X.Z. Liao, X.L. Wu, Deformation twinning in nanocrystalline materials, Prog. Mater. Sci., 57 (2012) 1-62.

[167] D. Wolf, V. Yamakov, S.R. Phillpot, A. Mukherjee, H. Gleiter, Deformation of nanocrystalline materials by molecular-dynamics simulation: relationship to experiments?, Acta Mater., 53 (2005) 1-40.

[168] L.Y. Chen, J.Q. Xu, H. Choi, H. Konishi, S. Jin, X.C. Li, Rapid control of phase growth by nanoparticles,Nat. Commun., 5 (2014)3879-9.

[169] T. Chookajorn, H.A. Murdoch, C.A. Schuh, Design of Stable Nanocrystalline Alloys,Science, 337 (2012) 951-954.

[170] R.P. Shi, C.P. Wang, D. Wheeler, X.J. Liu, Y. Wang, Formation mechanisms of self-organized core/shell and core/shell/corona microstructures in liquid droplets of immiscible alloys, Acta Mater., 61 (2013) 1229-1243.

[171] D. Wang, Y. Li, B.B. Sun, M.L. Sui, K. Lu, E. Ma, Bulk metallic glass formation in the binary Cu–Zr system, Appl.Phys.Lett., 84 (2004) 4029-3.

[172] M.I. Mendelev, M.J. Kramer, R.T. Ott, D.J. Sordelet, Molecular dynamics simulation of diffusion in supercooled Cu–Zr alloys, Phys.Mag. 89 (2009) 109-126.

[173] N. Wang, C. Li, Z. Du, F. Wang, W. Zhang, The thermodynamic re-assessment of the Cu–Zr system, Calphad, 30 (2006) 461-469.

[174] H. Okamoto, Cu-Zr (Copper-Zirconium),J. Phase Equilib. Diff., 33 (2012) 417-418.

[175] J.L. Murray, The Cu−Ti (Copper-Titanium) system, Bull. .Alloy Phase Diagr., 4 (1983) 81-95.

[176] W.A. Soffa, D.E. Laughlin, High-strength age hardening copper–titanium alloys: redivivus, Prog. Mater. Sci., 49 (2004) 347-366.

[177] A. Inoue, W. Zhang, T. Zhang, K. Kurosaka, Thermal and mechanical properties of Cu-based Cu-Zr-Ti bulk glassy alloys, Mater. Trans. JIM, 42 (2001) 1149-1151.

Chapter 3

Experimental techniques

3.1 Materials preparation

The microstructural evolution as a function of composition, and the effect of microstructure on mechanical behaviour, was systematically studied in a range of MgZnCa alloys and CuZrTi alloys. Specifically, the following alloys were investigated: For the MgZnCa BMGC,$Mg_{91.5}Zn_{7.5}Ca$, $Mg_{87.25}Zn_{11.25}Ca_{1.5}$;for CuZrTi nanostructured alloy $Cu_{90.5}Zn_{7.5}Ti_2$, $Cu_{90}Zn_8Ti_2$ and $Cu_{92.5}Zr_{7.5}$. $Mg_{91.5}Zn_{7.5}Ca_1$

Before prealloying, all the elements (≥purity 99.5%) were weighed from high purity elements with a Precisa XB120A precision electronic balance with an accuracy of ± 0.1mg. The elements were provided by Alfa Aesar and Newmet. All elements were cleaned with wire wool and filed to remove surface oxidation and dirt and, after weighing, the elements except Ca were placed in isopropanol in an ultrasonic bath at room temperature for 5 minutes to dislodge any remaining impurities from the surface.

3.1.1 Induction melting

Induction metling was used to prepare the ingots of MgZnCa alloy. The 10g ingots were alloyed in a boron nitride crucible. In order to balance evaporation losses during melting, an excess of 2 wt% of Zn and Mg were added. Before melting, the chamber was evacuated to 4×10^{-3}Pa and then the chamber was back-filled with argon with an inlet pressure of 2.2MPa and outlet pressure of 1.9MPa. The alloys were melted twice under following argon. The current was increased very slowly (0.2A/minute) to 1A and hold at 1A for 2 minutes to fully melt the alloy. During melting, the melt was agitated. After melting, the alloy was stored in argon atmosphere for 20miutes to cool down.

3.1.2 Injection casting

MgZnCa ingots were carefully polished with sand paper and file to get rid of oxidation and contamination of the surface before casting. MgZnCa BMGCs rods with a diameter of 2mm and 40mm in length were produced by injection casting in an inductive melter. An appropriate amount of alloy (about 1.5g) was cut from the ingot alloy (shown in Fig3.1) and then was loaded into a quartz crucible with a 1 mm diameter nozzle at bottom. The chamber was evacuated to a pressure of 4×10^{-3}Pa via a combination of roughing and diffusion pumping and then the chamber was backfilled with 2/3 atmosphere of argon. The alloy was heated above its melting point by an induction coil, after which an over-pressure of 40 KPa of argon was applied to the melt, forcing it out the quartz crucible and into copper die with a 2mm-diameter cavity.

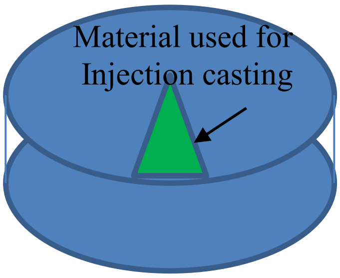

Fig3.1 Sketch of MgZnCa ingots with a diameter of 22mm and 15mm height showing where the material for injecting casting is taken from.

3.1.3 Arc melting

CuZrTi ingots were produced by arc-melting in a water-cooled copper crucible under a high purity argon atmosphere. After placing the high purity elements (3g in total) in the Cu crucible, the chamber was pumped down to 13 Pa and backfilled with argon. This procedure repeats 3 times and then pumped down to 6.7×10^{-3}Pa and backfilled with 1/3 argon atmosphere. In order to further minimize the residual oxygen content of the chamber, a Ti “getter” of roughly 10g was melted prior to melting the sample.   All the alloys were melted at least 3 times in total and were flipped between each melt stage. After melting, the ingot was measured again to make sure the mass loss was $< 0.1\%$.

3.1.4 Suction casting

An in-situ suction casting set-up was used to cast rods with a diameter of 2mm. In order to get a relatively high cooling rate, roughly 1g of alloy was used for each casting and a relatively low power setting (such as current) was applied for casting in comparison with that of melting. Before casting, the copper dies were carefully polished with 1μm diamond paste to increase the heat transfer ability. After the copper dies and alloy were loaded, the chamber and vacuum accumulator was backfilled with pure argon 3 times after the pressure was pumped down to 13Pa (shown in Fig3.2) and finally the chamber was pump down to 6.7×10^{-3}Pa. Before casting, the chamber was backfilled with argon with a pressure a little bit higher (0.1bar) than that of accumulator. The pressure of the chamber and accumulator at this stage could be roughly read from the gauges 1 and 2 shown in Fig3.1. A Ti “getter” was melted prior to casting to further reduce the effect of oxygen.

Fig3.2 Photograph of suction casting facility.

3.2 Characterization

3.2.1 X-ray diffraction

X-ray diffraction (XRD) was used to identify the microstructure of both MgZnCa BMGCs and CuZrTi nanostructured alloys. Samples for XRD test were sectioned into 1mm disks in thickness with a precision diamond saw from rods with a diameter of 2mm. In order to obtain a flat sample, all the disks were carefully polished with a self-designed grip to a same thickness (sample thickness variation less than 1μm) and 16 disks were mounted on a piece of glass using double-sided sticky tape(Fig3.3).

X-ray diffraction was performed on a Siemens D5000 diffractometer fitted with CuKα radiation source. The operating voltage and current of the instrument were 40KV and 40mA, respectively. In order to obtain a maximum signal from the sample, a very slow scan rate of 0.1° /min and a very low step size of 0.01° were used. The diffraction angle (2θ) ranged from

30 to 80 degrees for Mg-based BMGCs and 20 to 100 degrees for CuZrTi alloys.

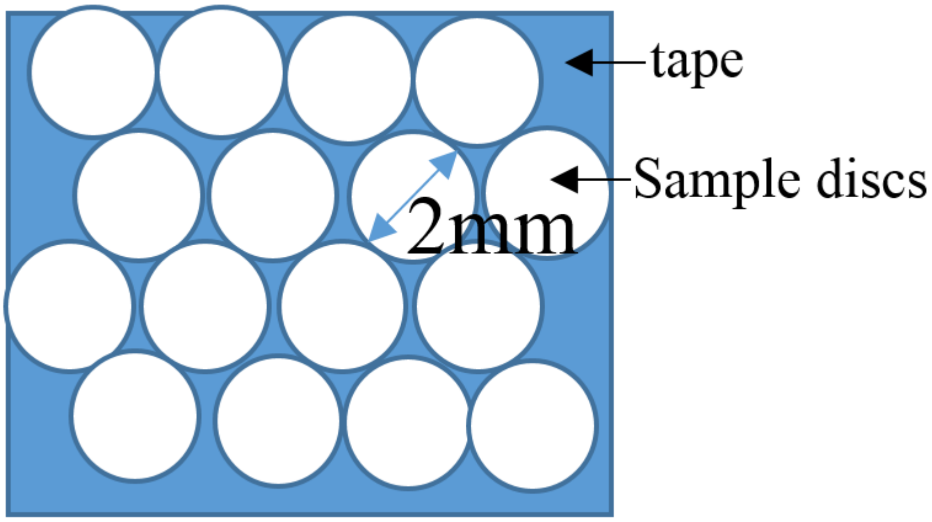

Fig3.3 Sketch of as-cast MgZnCa metallic glass and nanostructured CuZr alloy XRD samples with a diameter of 2mm and 1mm height.

3.2.2 Thermal Analysis

A Perkin Elmer Diamond DSC was used for Differential Scanning Calorimetry (DSC), in standard aluminium pans with a heating rate of 20 K/min up to 700 K under following argon gas for MgZnCa BMGCs. The weight of each sample was 10mg. A baseline scan was run with two empty pans, which was subsequently subtracted from the data file to obtain the real signal. The onset temperate of crystallization (T_{x1}) and melting (T_m) were determined and compared with that of the monolithic BMG of $Mg_{71}Zn_{25}Ca_4$ alloy.

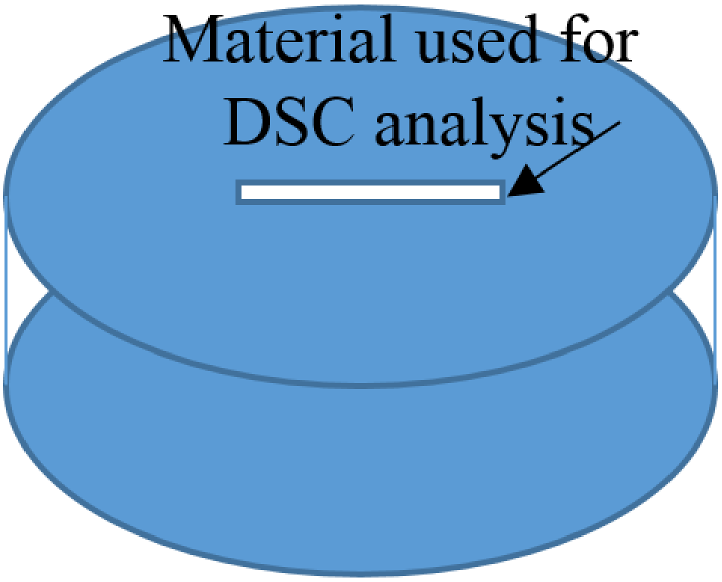

Fig3.3 Sketch of as-cast MgZnCa metallic glass composite showing where DSC samples were taken from.

3.2.3 Nanoidentation

A Hysitron Triboscope Nanomechanical tester (TS70) (coupled to a scanning probe microscope) fitted with a Berkovitch diamond tip was used to indent the dendrite and amorphous matrix of$Mg_{91.5}Zn_{7.5}Ca_1$alloy. For each phase, at least 5 different regions were probed at a load of 5mN. Indentation was performed in the centre of relatively large phase regions, so as to minimize the contribution to the resulting data from surrounding phases. The load, hold and unload regions of the loading schedule each had segment times of 5 s.

Nanoindentation tests were also conducted on nanostructured $Cu_{90.5}Zr_{7.5}Ti_2$ alloy to investigate the mechanical property difference of Cu dendrite solid solution and nanostructured CuZrTi matrix. For each phase, at least 4 different regions were probed at a load of 100μN. Indentation was also performed in the centre of relatively large phase regions, so as to minimize the contribution to the resulting data from surrounding phases. The load rate is 20μN and dwell time is 5 s.

3.2.4 Tensile and compressive Test

Tensile samples with a gauge dimension of Φ0.8mm× 4mm were machined and polished from the as-cast rods with a diameter of 2mm for MgZnCa BMGCs. Tensile tests were conducted on a Hounsfield testing device at a constant strain rate of $1.0 \times 10^{-4}\mathrm{s}^{-1}$ and a digital camera was used to calibrate and measure the strain during loading. At least five samples of each composition were tested to ensure reproducibility of the results. The average tensile mechanical properties, such as 0.2% proof stress ($\mathrm{R_{p0.2}}$), ultimate tensile stress (UTS), total strain to failure ($\varepsilon_{\mathrm{tot}}$) are determined. Hot extruded pure Mg samples with a gauge dimension of Φ6mm× 33mm are also tested on the Hounsfield testing device at a strain rate of $1.0 \times 10^{-1}\mathrm{s}^{-1}$ for comparison. The true stress and strain curves were converted from the engineering stress and strain by using the following two equations:

$$\sigma_{\mathrm{T}} = \sigma_{\mathrm{E}}(1 + \varepsilon_{\mathrm{E}}) \tag{3.1}$$

$$\varepsilon_{\mathrm{T}} = \ln(1 + \varepsilon_{\mathrm{E}}) \tag{3.2}$$

Where σ_{T},σ_{E}, ε_{T} and ε_{E} are the true stress, engineering stress, true strain and engineering strain, respectively.

Tensile tests were conducted on a ZWICK Z050TH 50kN test machine at a constant strain rate of $1.0 \times 10^{-4}\mathrm{s}^{-1}$ and a digital camera was used to calibrate and measure the strain during loading. Tensile samples with a gauge dimension of Φ0.8mm× 4mm were machined and polished from the as-cast rods with a diameter of 2mm for nanostructured CuZr alloys. At least five samples of each composition were tested to ensure reproducibility of the results. Hot extruded pure Cu samples with a gauge dimension of Φ5mm× 20mm were also tested at a strain rate of $1.0 \times 10^{-1}\mathrm{s}^{-1}$ for comparison. The average tensile mechanical properties, such as 0.2% proof stress ($R_{p0.2}$), ultimate tensile stress (UTS), total strain to failure (ε_{tot}) are also determined.

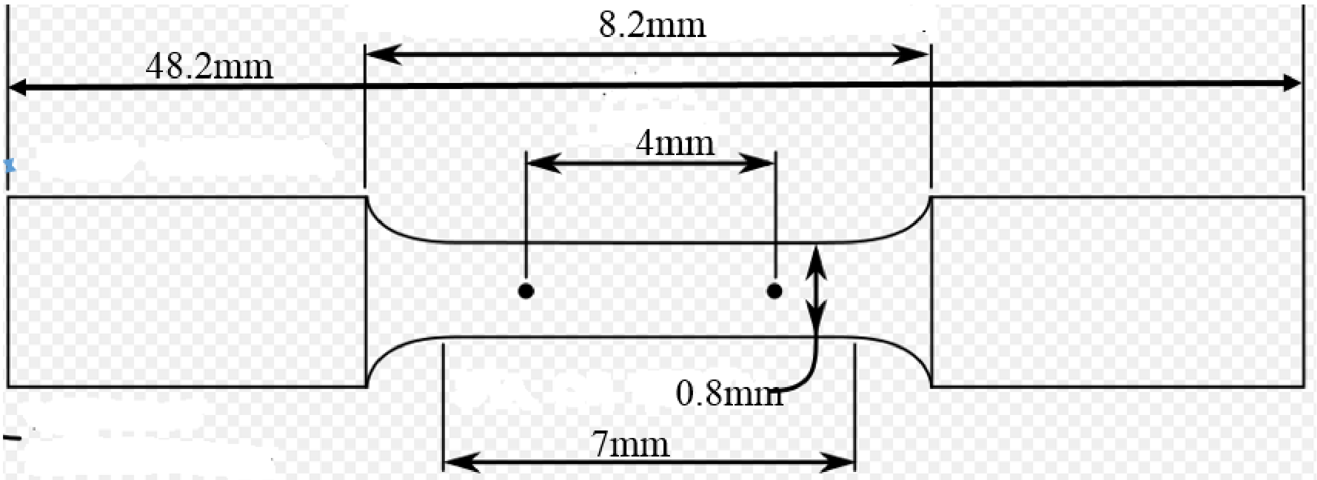

Fig3.4 Sketch of tensile samples for as-cast MgZnCa metallic glass composite and nanostructured CuZr alloy with a diameter of 2mm.

Compressive test was conducted on the Zwick testing equipment at room-temperature. The samples wit aspect ratio of 2:1 (2mm in diameter and 4mm in length) were cut from the as-cast rods, and each end of compressive testing samples were carefully grinded and polished using a home-made sample holder to ensure parallelism. Five specimens were tested for each composition to ensure that the results were reproducible and statistically meaningful. Samples were sandwiched between two BN platens, with graphite grease used as a lubricant to reduce the friction at the specimen–platen interface prior to each testing.

3.2.5 Elastic Modulus Measurement

The elastic modulus of MgZnCa BMGCs was determined via computations based on the sound velocities and material density. The acoustic shear velocity (ν_s) and longitudinal velocity (ν_l) of the BMGCs were determined using an Olympus EPOCH 600 digital ultrasonic flaw detector with a resolution of 10 ns. The carrying frequency of the ultrasonic is 5 MHz. The bulk density of the as-cast samples was determined by the Archimedes method using a balance (New Classic MF MS104S/01) with accuracy of ±0.0001 g.

The following equations are used to calculate the elastic moduli of the BMGCs from the sound velocities and material's density [1]:

$$G = \rho(v_s)^2 \tag{3.3}$$

$$E = 2G(1+\upsilon) \tag{3.4}$$

$$\upsilon = \frac{1}{2}\frac{(v_l)^2 - 2(v_s)^2}{(v_l)^2 - (v_s)^2} \tag{3.5}$$

3.2.6 Scanning Electron Microscopy

The microstructures of ingots, the as-cast samples, and the lateral surfaces and fracture surfaces of both Mg-based BMGCs and nanostructured CuZrTi alloys after tensile testing were investigated by the scanning electron microscopy (FEI Inspect F FEG SEM) with an energy-dispersive spectrometer (EDS). An accelerating voltage of 5kV was used for taking images and 20kV was used for EDS analysis in this work. For Mg-based BMGCs, SEM samples were prepared by grinding with silicon carbide grinding paper from P120 to P4000, followed by polishing with water-based diamond paste from 3μm to 1μm. Then the samples were directly analysed with SEM without etching using a back-scattered detector. Fracture surface and lateral surface after tensile test was analysed using secondary electron detector.

For nanostructured CuZrTi alloys, SEM samples of the ingots and as-cast samples were prepared by grinding with silicon carbide grinding paper from P120 to P4000 and polishing with diamond suspension from 3μm to 1μm. After polishing, the samples were polished using alumina suspension with addition of 1drop/5ml of nitric acid (70%) and 1 drop/5ml of H_2O_2 (30%) for 3mins. Then, the samples were washed in a ultrasonic bath. A back-scattered electron detector was used for analysing the structure of ingots and as-cast samples. A secondary electron detector was used for analysing the microstructure of fracture surface after tensile test.

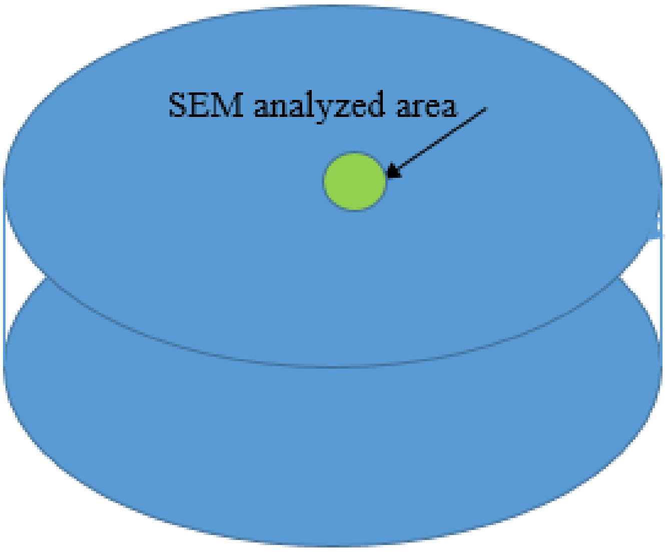

Fig3.5 Sketch of tensile samples for as-cast MgZnCa metallic glass composite and nanostructured CuZr alloy showing SEM analysed area in the cross-section.

3.2.7 Transmission Electron Microscopy

Both Mg-based BMGCs and nanostructured CuZrTi alloys were studied by transmission electron microscopy (TEM). The TEM samples were produced by grinding the specimens (discs of 2mm in diameter) to a thickness of 20μm and then the thin foil was stuck onto a copper O-ring for Mg-based BMGCs (Mo O-ring for nanostructured CuZrTi alloy) with a hole of 1.5mm in diameter. The thin foil samples were thinned by ion milling in Fischione Precision Ion Milling and Polishing System at liquid nitrogen temperatures.

The microstructure of both Mg-based BMGCs and nanostructured CuZrTi alloys was analysed by FEI Tecnai 20 TEM first operated at an accelerating voltage of 200kV, with a an Oxford Instruments energy-dispersive spectrometer. The as-cast $Mg_{91.5}Zn_{7.5}Ca_{1}$ alloy was further analysed by high resolution transmission electron microscopy in a JEOL-2010F operating at 200kV with an Oxford Instruments energy-dispersive spectrometer. The $Cu_{90.5}Zr_{7.5}Ti_{2}$ alloy was analysed by high resolution transmission electron microscopy (TEM) in a JEOL-R005 operating at 300kV with an energy-dispersive spectrometer.

3.3 References

[1] S. Kim, H. Ledbetter, Y. Li, Elastic constants of four Fe-Cr-Ni-Mn alloys, J. Mater. Sci., 29 (1994) 5462-5466

Chapter 4

New Compositional Design for Creating Tough Metallic Glass Composites with Excellent Work Hardening

Abstract

The extrinsic size of both crystalline alloys and amorphous metallic alloys strongly affects their mechanical properties at the submicron scale or nanometre scale. For example Zr-based metallic glass nanopillars exhibit ceramic-like strengths (2.25GPa) and metal-like ductility (25%) simultaneously when the pillar dimension is reduced to <100nm. In this chapter a new compositional design approach is reported to create tough metallic glass composites consisting of micrometre scale dendrites and nanometre scale amorphous matrices that exhibit high strength and ductility in the normally brittle MgZnCa metallic glass system. When the thickness of the amorphous matrix was reduced to the nanometre scale, a low density (ρ≈1.99g/cc) $Mg_{91.5}Zn_{7.5}Ca_1$ alloy exhibited room temperature tensile ductility exceeding 15.6%, yield strength of 215MPa and fracture strength of 478MPa. TEM analysis demonstrated that the alloy consisted of micrometre scale α-Mg solid solution dendrites and nanometre scale amorphous matrix (80-530nm in thickness). The homogeneous deformation of nanometre scale amorphous matrices is believed to be responsible for the high toughness and excellent work-hardening behaviour.

4.1 Introduction

The achievement of both high strength and extended deformability is vital for most structural materials, but these two attributes are generally mutually exclusive [1, 2]. Bulk metallic glasses (BMGs) are a new class of engineering materials which exhibit excellent properties such as high elastic limit, high strength, high hardness and improved wear resistance [1-5]. However, most BMGs have low ductility and fail in a brittle manner due to highly localized deformation processes, such as shear banding, which propagates unhindered since there are no microstructural features in a monolithic metallic glass to impede them [1-3]. Since the discovery of Mg-Ni-Ce BMG by Inoue et al.[4], Mg-based BMGs have become especially attractive in the BMG family due to their excellent glass forming ability, high strength, low density and relative low cost[5]. In comparison with Zr- (or Cu and Pd) based BMG, Mg-based BMGs are more brittle and flaw sensitive [6]. Bulk metallic glass matrix composites (BMGCs) are currently well recognized as leading-edge new materials, because they maintain the useful properties of monolithic metallic glass such as high strength and large elastic strain limit but exhibit high ductility as well [7-9]. Currently, most of the ductile BMGCs are developed from the Ti/Zr-Be-based systems [7-11]. The Ti/Zr-Be-based composites are optimal for BMGC formation due to the lack of stable compounds between the constituents and Be, which prevents heterogeneous nucleation at the dendrites during quenching [10]. Although both in-situ [5, 12-14] and ex-situ [15, 16] Mg-based BMGCs have been developed in several alloy systems, only improvement in compressive ductility has been observed in these Mg-based BMGCs.

Hofmann et al. [7] suggest that the large plastic strain and toughness of these Ti/Zr-Be-based composites are based on the following two principles: (i) introducing dendrites with lower shear modulus compared with the amorphous matrix to initiate local shear banding; and (ii) matching the microstructural length scale such as the interdendritic spacing, λ, with the radius of the plastic zone (Rp) to impede the share band extension. However, the method to design a Be-free metallic glass composite that exactly satisfies the above two principles is currently not clear and subject to debate. Moreover, the Zr/Ti-Be-based BMGCs exhibit a macroscopic strain softening phenomenon with an early onset of necking [9,17], which would limit their usefulness as engineering materials [17]. The early macroscopic softening is believed to be associated with the micrometre scale glass matrix that usually exhibits softening after yielding[9], suggesting that mitigation could be achieved by using this feature size as a design parameter, decreasing the thickness of the glass matrices to nanometre scale. When the sample size is reduced to a critical value (30-100nm for Zr-based BMG)[18], the stress required to propagate a pre-existing shear band is higher than the stress required for homogeneous plastic deformation, so any formed embryonic shear band remains stable while homogenous deformation prevails[18].

4.2 Composition design

In the current work, new Mg-based BMGCs with high tensile ductility and excellent work hardening are developed from a normally brittle MgZnCa ternary BMG by a new composition design method. The compositions mentioned in this work are in atomic percent. These alloys were designed in the following three steps: (i) Identify a Mg-based BMG alloy with robust glass forming ability and restricted solubility of the alloying elements in the equilibrium system. The MgZnCa ternary system was chosen because it exhibits high glass forming ability and Zn and Ca have restricted solubility even at high temperature of the equilibrium close-packed hexagonal (c.p.h.) Mg[6,19]. (ii) Target the composition with highest glass forming ability of the BMG system and use this atomic ratio of alloying elements in the composition. According to Zhao et al.[6], $Mg_{66}Zn_{30}Ca_4$ exhibits the highest glass forming ability (with a critical diameter of 5mm), so this defined the atomic ratio of Zn/Ca as 7.5. (iii) Partially replace the Zn and Ca at the fixed atomic ratio of 7.5 with Mg. By introducing more Mg at the expense of the solute constituents (Zn and Ca), the current Mg alloys ($Mg_{91.5}Zn_{7.5}Ca_1$ 5 and$Mg_{87.25}Zn_{11.25}Ca_{1.5}$indicated as C1 and C2 in Fig4.1a) are substantially hypoeutectic in chemical composition. As a result, α-Mg solid solution will solidify first from the melt. The formation of α-Mg solid solution is extremely difficult to suppress even with a high cooling rate since there is a strong thermodynamic driving force and rapid formation kinetics in the hypoeutectic compositions [5].Zn and Ca have restricted solubility even at high temperature in the equilibrium c.p.h. Mg and thus are expected to partition preferentially to the remaining liquid during the initial stage of solidification, such that the remaining super-cooled liquid becomes enriched in Zn and Ca with an atomic ratio close to 7.5. When the remaining super-cooled liquid is close enough to the (near) eutectic bulk glass forming composition, as shown in Fig4.1b, the formation of the eutectic structure can be fully suppressed and an amorphous phase could be formed in the remaining liquid. Therefore, according to Fig4.1b, the volume fraction and size of both dendrite and amorphous matrix can be tuned by varying composition.

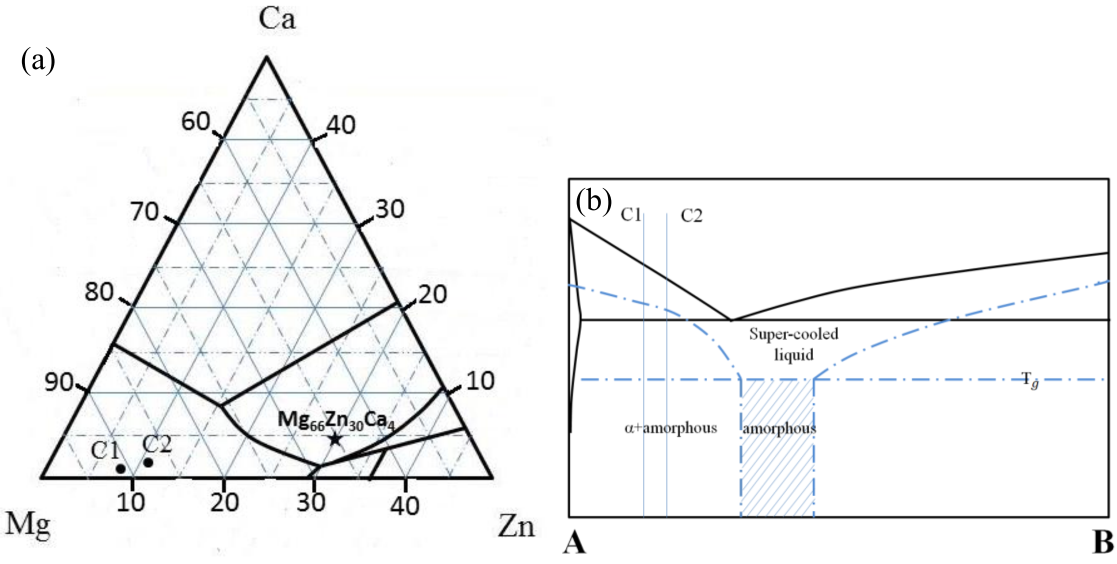

Fig4.1 (a) Pseudo-ternary MgZnCa diagram showing the alloy compositions studied (indicated by solid circles) and the position of $Mg_{66}Zn_{30}Ca_4$ (indicated by star); black lines in (a) representing the eutectic reaction of ternary MgZnCa alloy in the Mg-rich corner. (b) Schematic diagram showing the solidification process of current hypoeutectic alloys (dashed line in (b) representing the non-equilibrium solidification state occurred in current work)

4.3 Results

4.3.1Microstructure analysis of as-cast Mg-based BMG

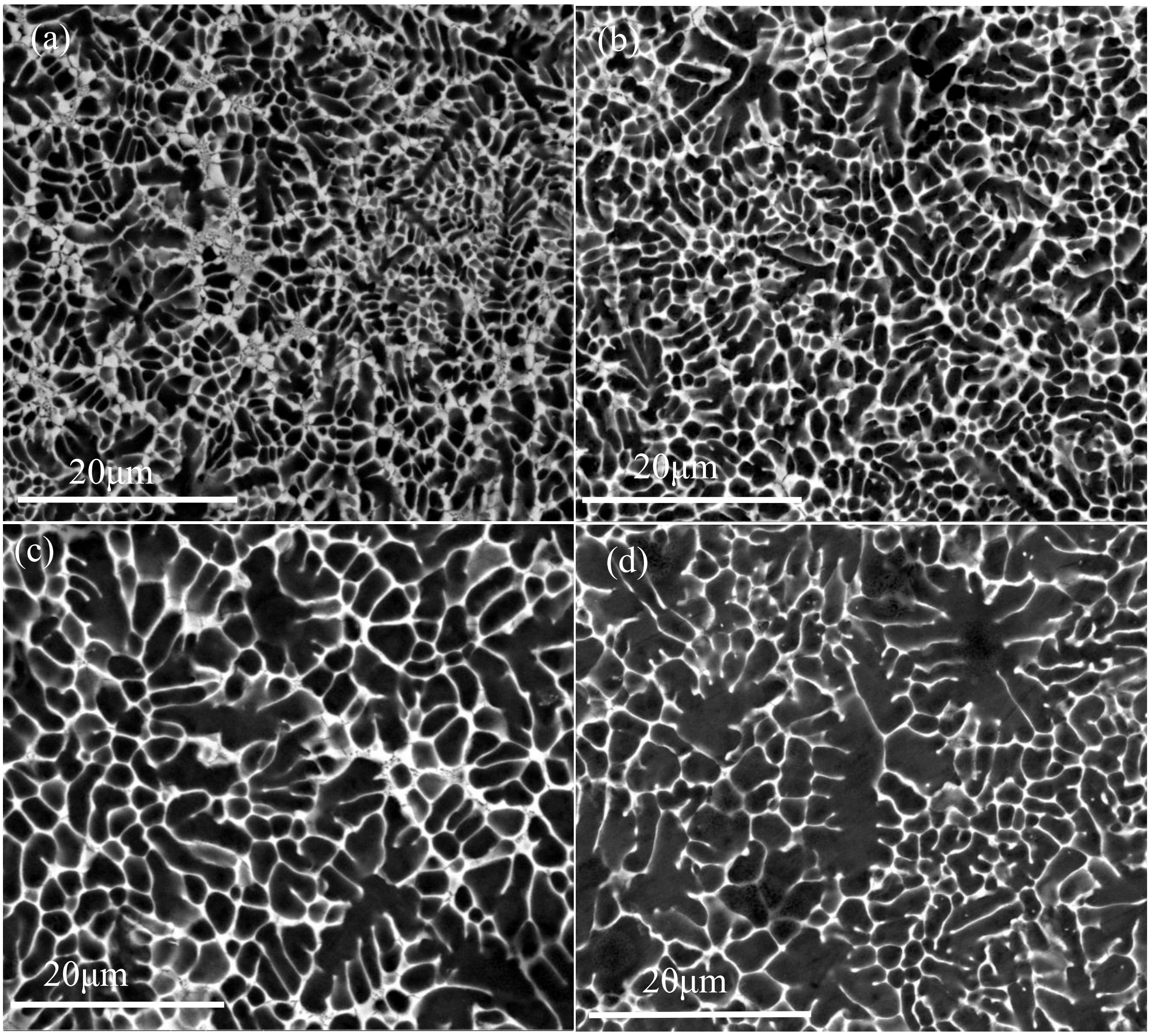

Fig4.2 Back scattered SEM images of as-cast Mg-based BMGCs with 2mm in diameter: $Mg_{78.75}Zn_{18.75}Ca_{2.5}$ (a), $Mg_{83}Zn_{15}Ca_2$ (b), $Mg_{87.25}Zn_{11.25}Ca_{1.5}$ (c) and $Mg_{91.5}Zn_{7.5}Ca_1$ (d).

Fig4.2 shows SEM images taken from the center of the as-cast $Mg_{78.75}Zn_{18.75}Ca_{2.5}$, $Mg_{83}Zn_{15}Ca_2$, $Mg_{87.25}Zn_{11.25}Ca_{1.5}$ and $Mg_{91.5}Zn_{7.5}Ca_1$ alloys. The backscattered electron SEM images show a dendritic phase homogeneously dispersed in a matrix exhibiting bright atomic number contrast. As can be seen from Fig 4.2a-d, both the amount and size of the crystalline dendrites increases with an increase in the concentration of Mg, while the amount

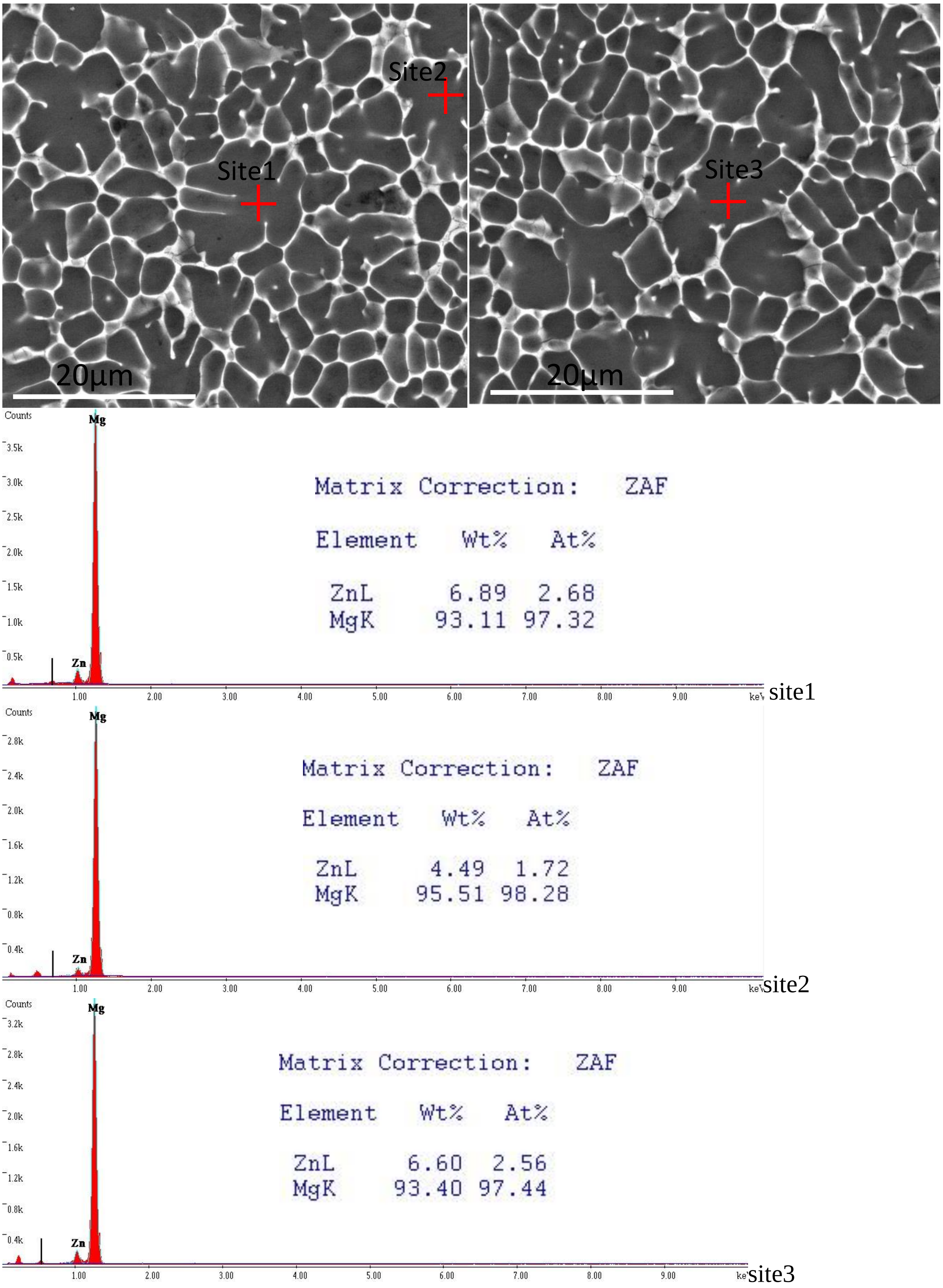

```
Matrix Correction:   ZAF

Element   Wt%   At%

 ZnL      6.89  2.68
 MgK     93.11 97.32
```

```
Matrix Correction:   ZAF

Element   Wt%   At%

 ZnL      4.49  1.72
 MgK     95.51 98.28
```

```
Matrix Correction:   ZAF

Element   Wt%   At%

 ZnL      6.60  2.56
 MgK     93.40 97.44
```

Fig4.3 EDS spectra taken from the centre of dendrites of $Mg_{91.5}\,Zn_{7.5}\,Ca_1$.

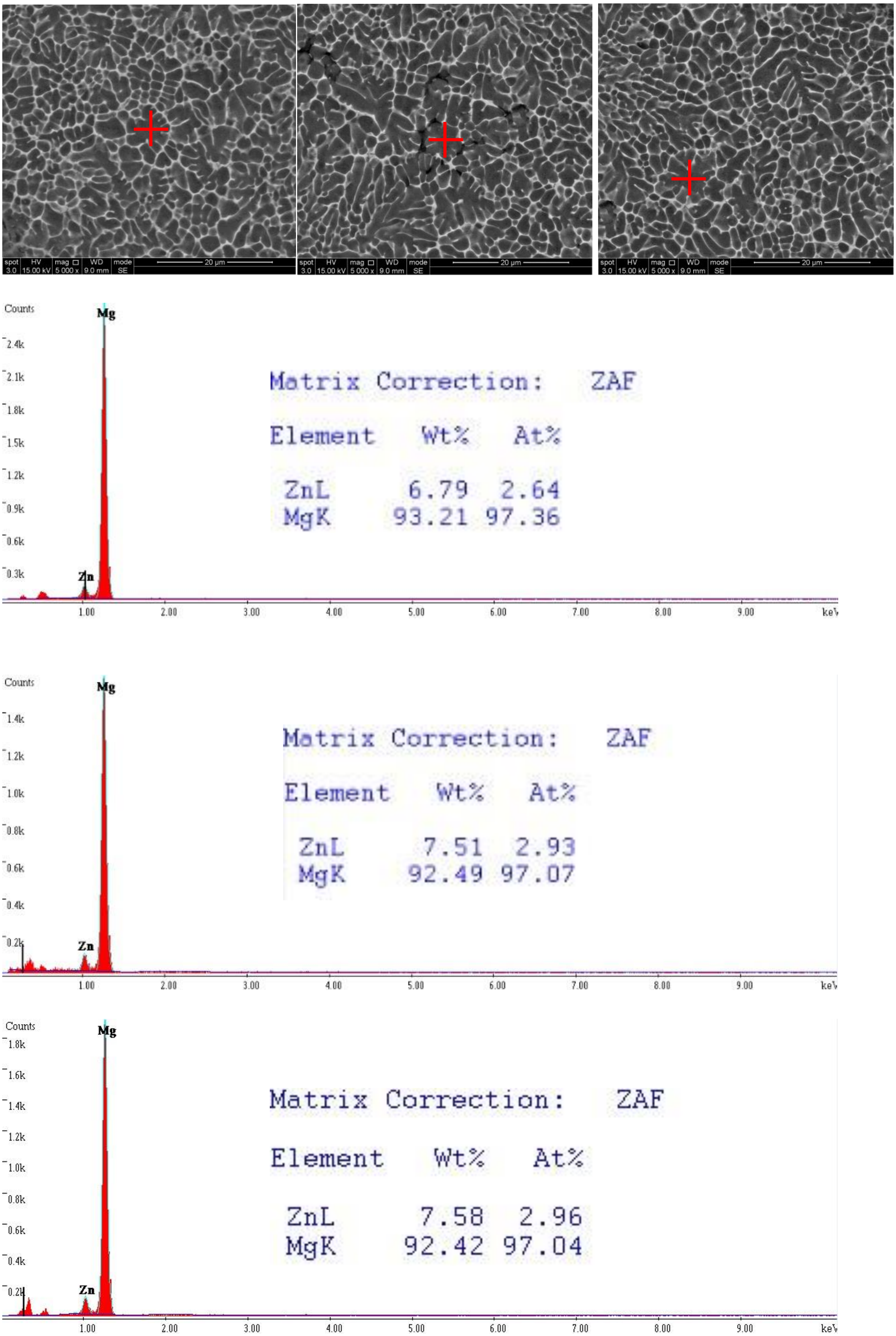

Matrix Correction: ZAF

Element	Wt%	At%
ZnL	6.79	2.64
MgK	93.21	97.36

Matrix Correction: ZAF

Element	Wt%	At%
ZnL	7.51	2.93
MgK	92.49	97.07

Matrix Correction: ZAF

Element	Wt%	At%
ZnL	7.58	2.96
MgK	92.42	97.04

Fig4.4 EDS spectra of as-cast $Mg_{87.25}Zn_{11.25}Ca_{1.5}$.

and thickness of matrix decreases. Image analysis from Fig4.2c and d indicates that the volume fraction volume fraction of crystalline dendrites for $Mg_{87.25}Zn_{11.25}Ca_{1.5}$ and $Mg_{91.5}$ - $Zn_{7.5}$ $Ca_1$was ~85.1% and ~90.5%, respectively. The dendrite size for $Mg_{91.5}$ $Zn_{7.5}$ Ca_1 varies between 1– 22µm while the inter-dendrite spacing varies over 80-530nm. For the $Mg_{87.25}Zn_{11.25}Ca_{1.5}$alloy, the dendrite size ranges between 0.4-15.3µm, whereas the inter-dendrite spacing ranges between 0.3-6.6µm. The EDS spectra taken from the right center of the relatively larger dendrites show that the dendrite composition for $Mg_{91.5}$ $Zn_{7.5}$ Ca_1 alloy ranges between $Mg_{97.3-98.3}$ $Zn_{1.7-2.7}$ (Fig4.3), while the composition of the dendrite in $Mg_{87.25}Zn_{11.25}Ca_{1.5}$ is in the range $Mg_{96.7-97.4}$ $Zn_{2.6-3.3}$ (Fig4.4).

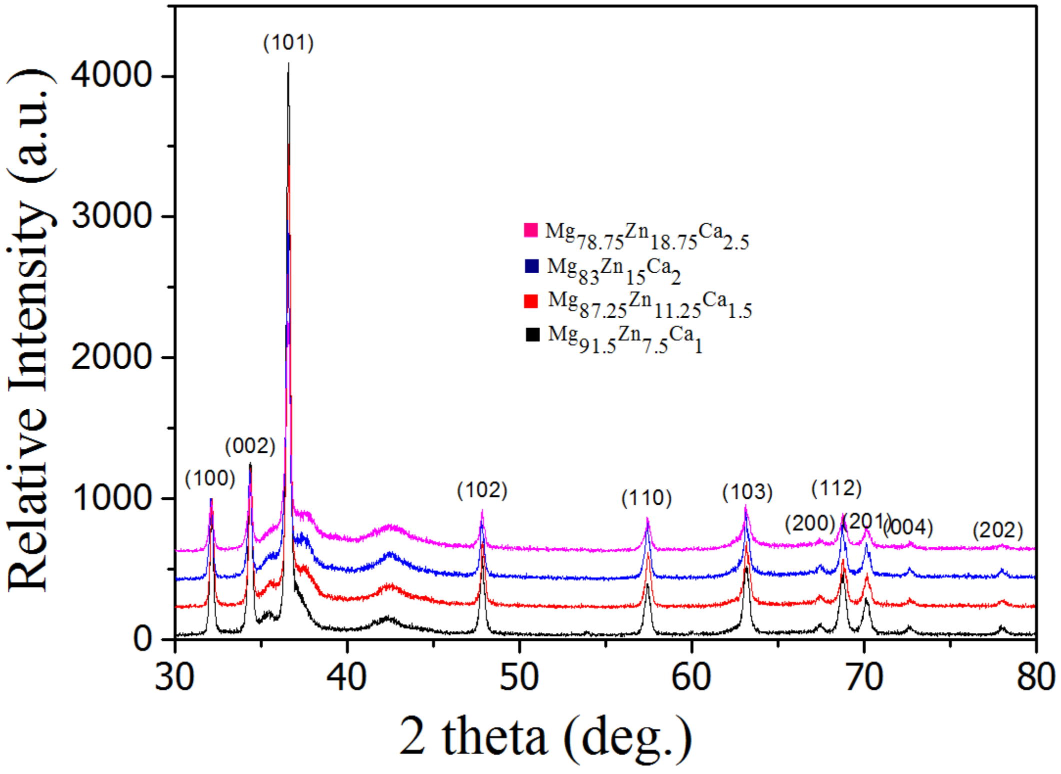

Fig4.5 XRD patterns of as-cast Mg-based BMGCs.

The XRD patterns shown in Fig4.5 indicate that the peaks (labeled with (h k l) values) for c.p.h. α-Mg solid solution are superimposed on the broad diffuse-scattering amorphous maxima, further identifying the two phase structure. As the volume fraction of amorphous matrix increases with an increase in the amount of alloying elements, the broad halo peak, corresponding to the amorphous phase, becomes more obvious for $Mg_{78.75}Zn_{18.75}Ca_{2.5}$, $Mg_{83}Zn_{15}Ca_{2}$, and $Mg_{87.25}Zn_{11.25}Ca_{1.5}$. The broad diffraction peak observed in the 2θ range of 40-45° could be attributed to the formation of MgO on the disc surface of XRD samples.

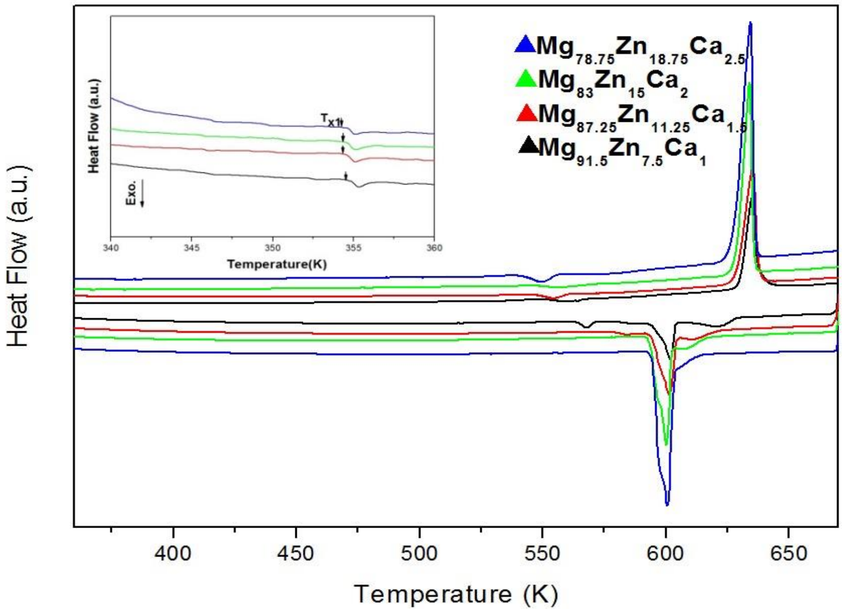

Fig4.6 DSC scans of as-cast Mg-based BMGCs specimens, with a heating rate of 20k/min; (inset) the crystallization stage.

The DSC analysis shown in Fig4.6 further confirms that an amorphous phase exists as the matrix. The DSC curves show that, with a variation of the alloy composition, both the onset temperature of crystallization (T_{x1} shown in the inset of Fig4.6) and the onset temperature of melting (T_m) remain almost constant at 354K and 625K, respectively. Moreover, the T_{x1} and T_m of these four alloys are very close to the T_{x1} (356K) and T_m(611k) of the monolithic BMG of $Mg_{71}Zn_{25}Ca_{4}$ alloy [6]. During the cooling process, several exothermic peaks corresponding to their solidifying event appeared with an onset temperature of 620K. With an increase of the alloying content, both the endothermic and exothermic peaks become stronger. Therefore, it may be inferred that T_m represents the ternary eutectic temperature.

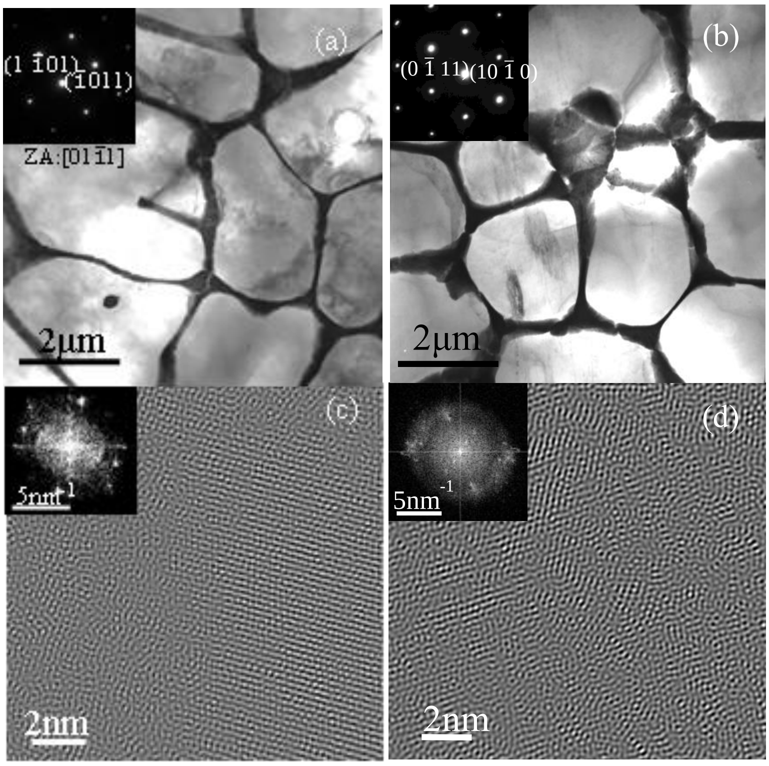

Fig4.7 Bright field TEM images of microstructures of (a) $Mg_{91.5}Zn_{7.5}Ca_1$ and (b) $Mg_{87.25}Zn_{11.25}Ca_{1.5}$; (inset) selected area diffraction pattern taken from c.p.h. dendrites. (c), IFFT image from the interface between amorphous matrix (left hand side) and c.p.h. dendrite (right hand side) of $Mg_{91.5}Zn_{7.5}Ca_1$; (inset) corresponding FFT pattern. (c), IFFT image from the middle of the amorphous matrix of $Mg_{91.5}Zn_{7.5}Ca_1$; (inset) corresponding FFT pattern confirming the presence of nanocrystals in the amorphous matrix.

To further identify the microstructure, TEM was performed to investigate the as-cast $Mg_{91.5}Zn_{7.5}Ca_1$ and $Mg_{87.25}Zn_{11.25}Ca_{1.5}$ alloys. The bright field TEM images show the c.p.h. dendrite (bright contrast regions in Fig4.7a and b) dispersed in the amorphous matrix (dark contrast regions). The insets in the top-left-hand side in Fig4.7a and b show the selected-area diffraction patterns taken along the $[0\ 1\ \bar{1}1]$ and $[1\ \bar{2}13]$ zone axis of the dendrites, which further conform that the dendritic phase is c.p.h. α-Mg in both alloys. A high resolution TEM

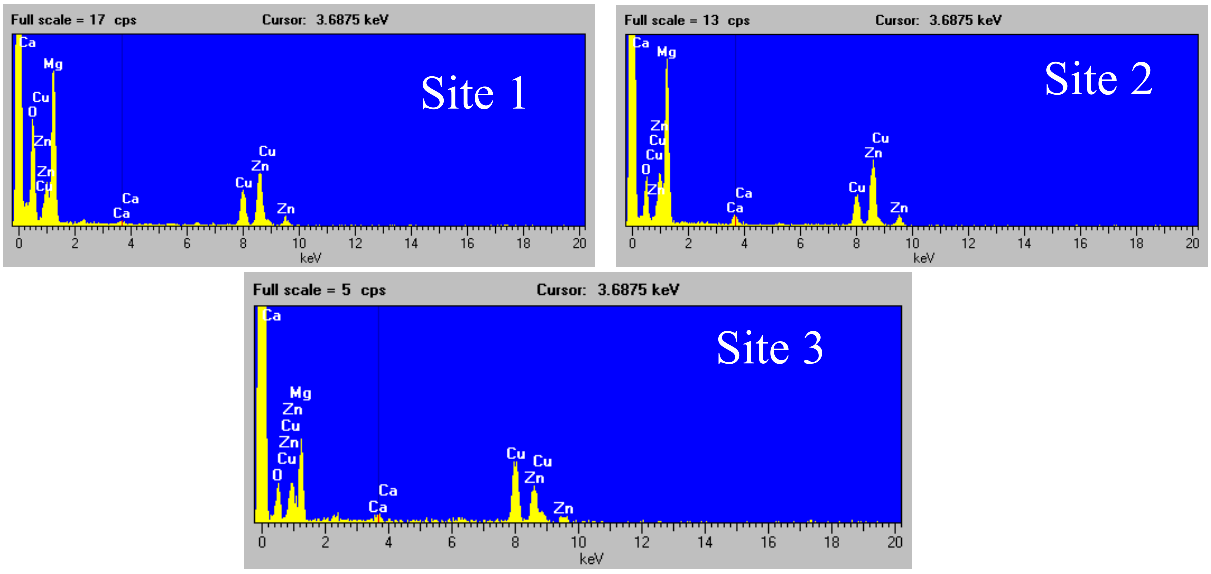

Site 1	Elmt	Peak Area	Stat. Sigma	k Factor	Abs. Corrn.	Element %	Sigma %	Atomic %
	Mg K	5119	131	1.049	1.000	56.84	1.37	77.64
	Ca K	134	42	0.958	1.000	1.36	0.42	1.13
	Zn K	2682	134	1.473	1.000	41.80	1.37	21.24

Site 2	Elmt	Peak Area	Stat. Sigma	k Factor	Abs. Corrn.	Element %	Sigma %	Atomic %
	Mg K	4186	118	1.049	1.000	52.81	1.42	74.34
	Ca K	253	45	0.958	1.000	2.92	0.51	2.49
	Zn K	2499	129	1.473	1.000	44.27	1.45	23.17

Site 3	Elmt	Peak Area	Stat. Sigma	k Factor	Abs. Corrn.	Element %	Sigma %	Atomic %
	Mg K	695	48	1.049	1.000	48.76	3.36	70.49
	Ca K	90	23	0.958	1.000	5.76	1.45	5.05
	Zn K	462	58	1.473	1.000	45.48	3.54	24.46

Fig4.8 HR-TEM EDS spectra of the amorphous matrices of as-cast $Mg_{91.5}Zn_{7.5}Ca_{1}$.

image taken from the interface is shown in Fig4.7c. The micrograph confirms the sharp interface between the two phases. The HRTEM micrograph taken from the middle of the matrix is displayed in Fig4.7d, with corresponding FFT. This shows a predominantly amorphous phase, although there were occasional small nanocrystallites (≤7nm) embedded in the amorphous phase. EDS results revealed that the composition of the matrix region was in the range $Mg_{70.5-77.6}Zn_{21.2-24.5}Ca_{1.1-5.0}$ (Fig4.8), which is similar to $Mg_{71}Zn_{25}Ca_{4}$ alloy, consistent with the DSC results.

4.3.2 Microstructural analysis of the ingots of Mg-based BMGCs.

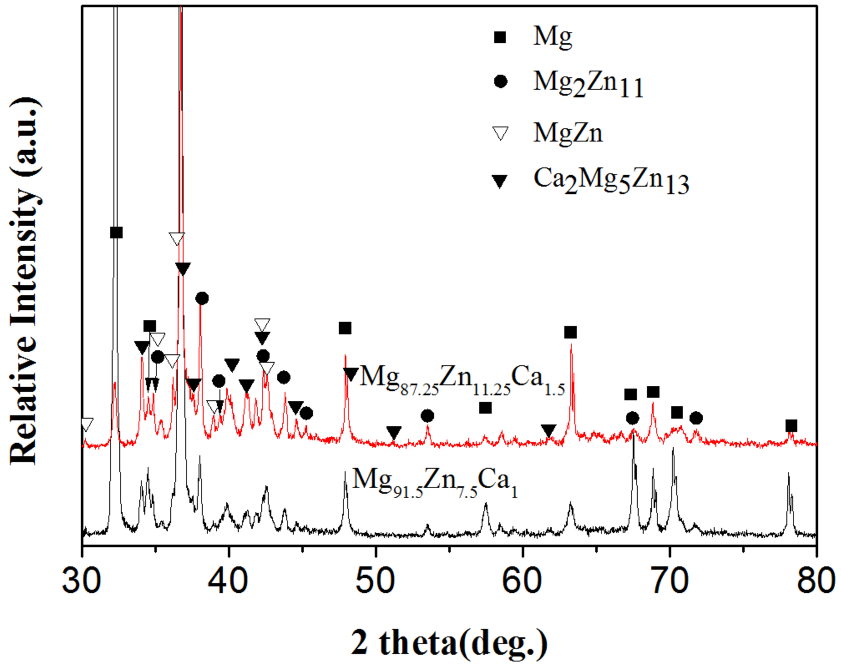

Fig4.9 XRD patterns of $Mg_{91.5}Zn_{7.5}Ca_1$ (a) and $Mg_{87.25}Zn_{11.25}Ca_{1.5}$ (b) taken from their ingot alloys with a diameter of 15mm and 10mm in thickness

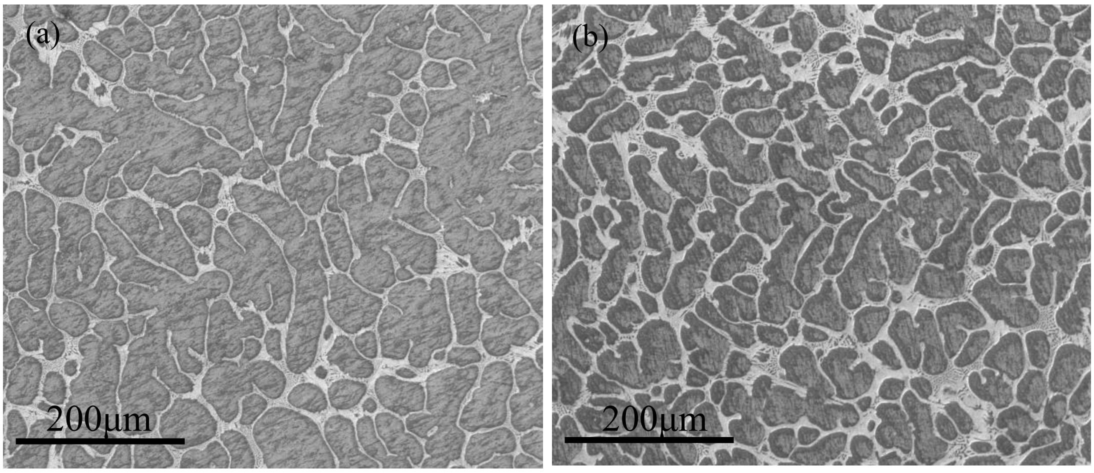

Fig4.10 Secondary electron SEM images of $Mg_{91.5}Zn_{7.5}Ca_1$ (a) and $Mg_{87.25}Zn_{11.25}Ca_{1.5}$ (b) taken from their ingot alloys with a diameter of 15mm and 10mm in thickness.

Table4.1 Summary of XRD results of MgZnCa ingots and BMGCs.

Alloys	Phases
MgZnCa ingots	Mg,Mg_2Zn_{11},MgZn,$Ca_2Mg_5Zn_{13}$
As-cast MgZnCa BMGCs	Mg, Amorphous phase

In order to obtain more information about the solidification procedure of these Mg-based BMGCs, the analysis of the ingots of $Mg_{91.5}Zn_{7.5}Ca_1$ and $Mg_{87.25}Zn_{11.25}Ca_{1.5}$ alloys was also conducted. Fig4.9 and Fig4.10 show the XRD patterns and SEM images of air-cooled $Mg_{91.5}Zn_{7.5}Ca_1$ and $Mg_{87.25}Zn_{11.25}Ca_{1.5}$ alloys with a diameter of 15mm and 10mm in thickness. From the XRD patterns (Fig4.9), it is identified that the microstructures is composed of α-Mg,Mg_2Zn_{11}, MgZn and $Ca_2Mg_5Zn_{13}$(table 4.1). As $Mg_{91.5}Zn_{7.5}Ca_1$ alloy has more Mg addition than $Mg_{87.25}Zn_{11.25}Ca_{1.5}$, the peaks corresponding to α-Mg in $Mg_{91.5}Zn_{7.5}Ca_1$ alloy are stronger than that in $Mg_{87.25}Zn_{11.25}Ca_{1.5}$. However, the peaks corresponding to intermetallic observed in $Mg_{91.5}Zn_{7.5}Ca_1$ are relatively weaker than that in $Mg_{87.25}Zn_{11.25}Ca_{1.5}$ alloy, indicating less intermetallic was formed in $Mg_{91.5}Zn_{7.5}Ca_1$ alloy due to its smaller amount of alloying elements. There are other diffraction peaks that cannot be identified. To further identify the microstructure of the above ingot alloys, we performed SEM and EDS analysis. Fig4.10a and b display SEM images of the ingots of $Mg_{91.5}Zn_{7.5}Ca_1$ and $Mg_{87.25}Zn_{11.25}Ca_{1.5}$ alloys, respectively. It can be seen in both Fig4.10a and b that a dendritic phase homogeneously dispersed in a matrix exhibiting a eutectic structure. Image analysis from these images shows that both the amount and size of the dendrites decreases with an increase in the concentration of alloying elements, while the amount and size of eutectic phases increases. Image analysis from these images indicates that the volume fraction of crystalline dendrites for $Mg_{87.25}Zn_{11.25}Ca_{1.5}$ and $Mg_{91.5}Zn_{7.5}Ca_1$ was ~85.5% and ~89.7%, respectively. The dendrite size for $Mg_{91.5}Zn_{7.5}Ca_1$ varies between 8–207μm.For the

$Mg_{87.25}Zn_{11.25}Ca_{1.5}$ alloy, the dendrite size ranges between 5-164µm. The EDS spectra taken from the right center of the dendrites show that the dendrite composition for $Mg_{91.5}Zn_{7.5}Ca_{1}$alloy ranges between $Mg_{98.5-98.3}Zn_{1.3-1.5}$ (Fig4.11), while the composition of the dendrite in $Mg_{87.25}Zn_{11.25}Ca_{1.5}$ is in the range $Mg_{98.2-98.3}Zn_{1.7-1.8}$ (Fig4.12). The EDS spectra taken from the center of relative large eutectic structure show that the eutectic structure

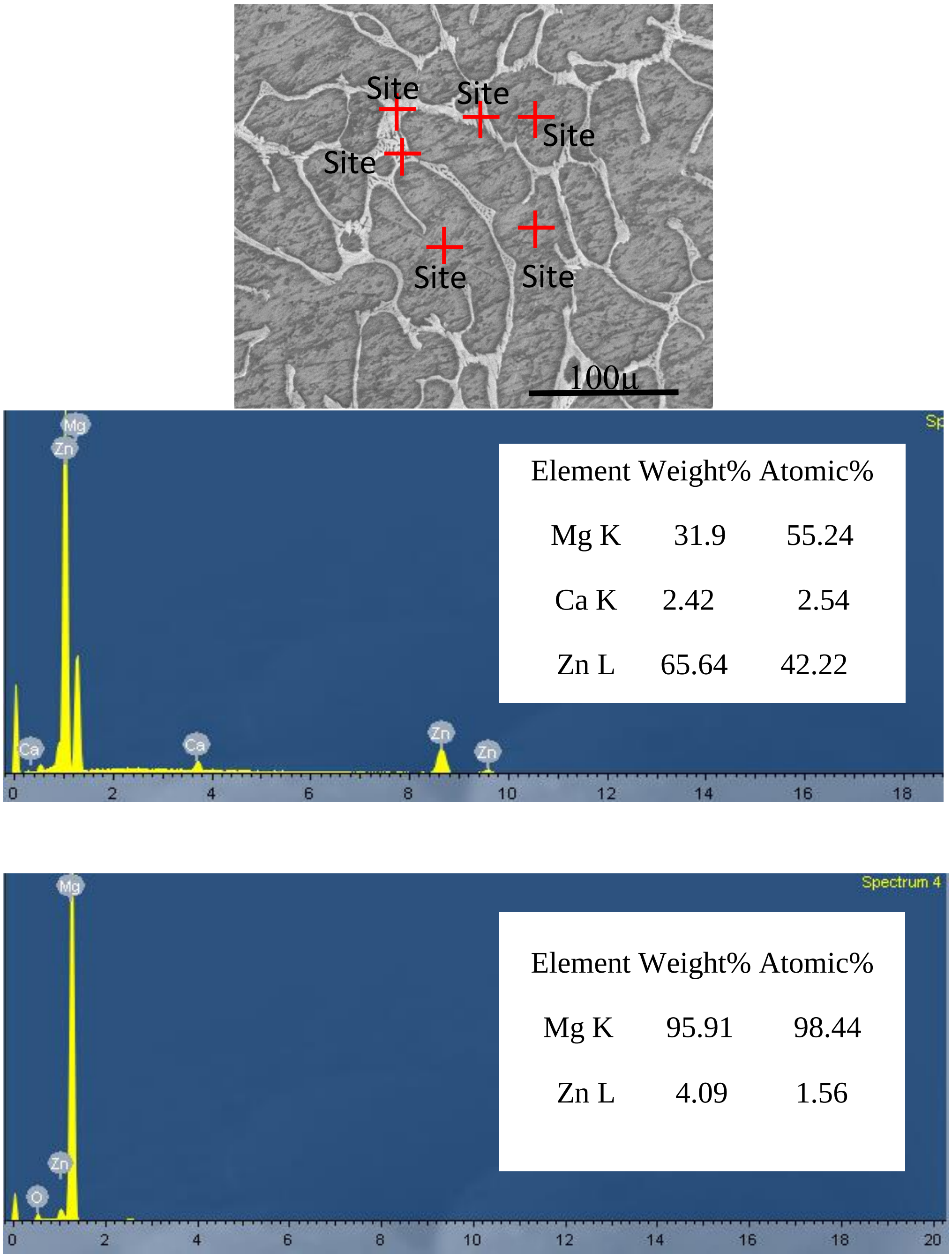

Element	Weight%	Atomic%
Mg K	31.9	55.24
Ca K	2.42	2.54
Zn L	65.64	42.22

Element	Weight%	Atomic%
Mg K	95.91	98.44
Zn L	4.09	1.56

Fig4.11 EDS spectra taken from the center of dendrites of $Mg_{91.5}Zn_{7.5}Ca_{1}$ ingot.

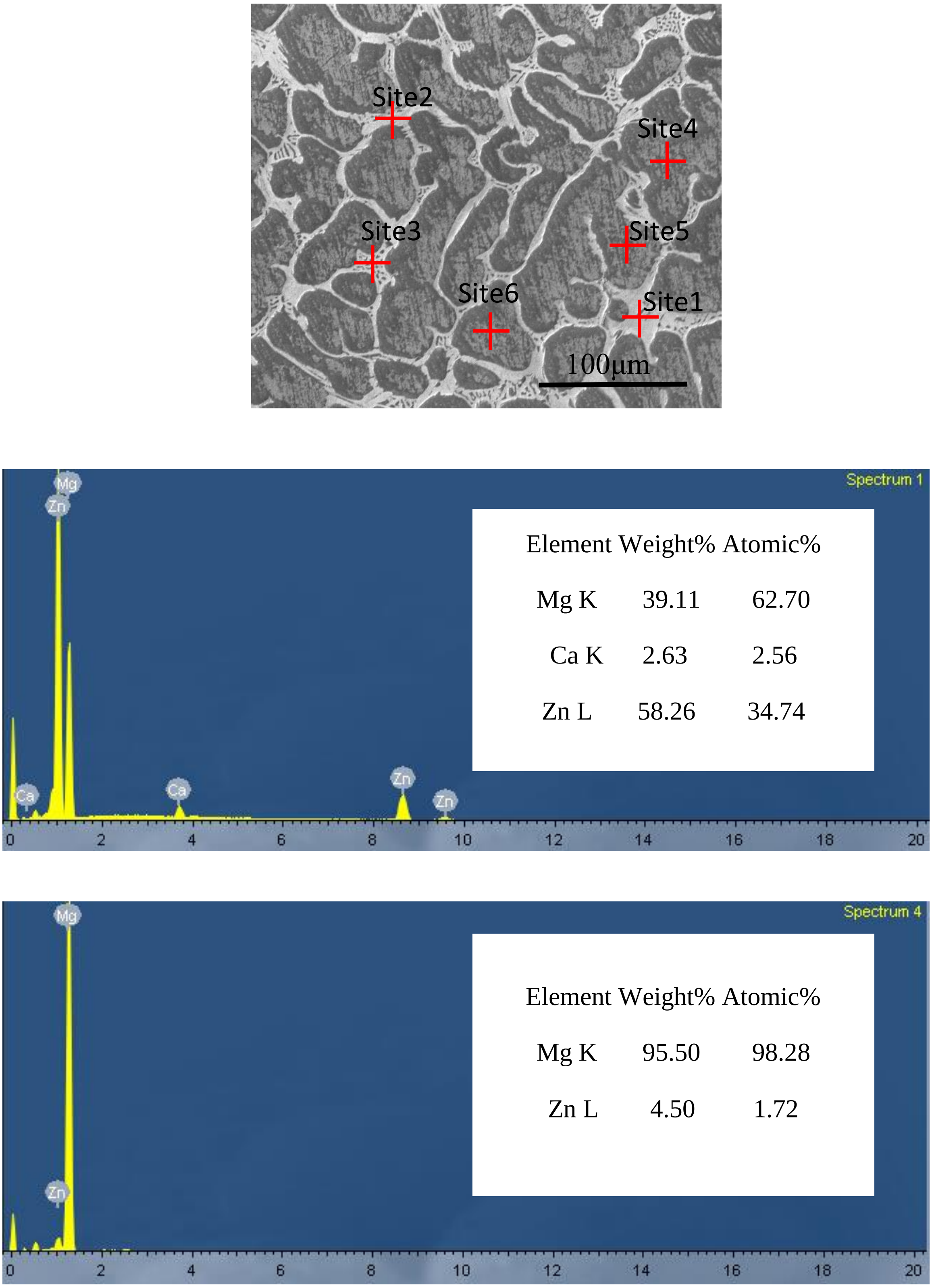

Element	Weight%	Atomic%
Mg K	39.11	62.70
Ca K	2.63	2.56
Zn L	58.26	34.74

Element	Weight%	Atomic%
Mg K	95.50	98.28
Zn L	4.50	1.72

Fig4.12 EDS spectra of $Mg_{87.25}Zn_{11.25}Ca_{1.5}$ ingot.

composition for $Mg_{91.5}Zn_{7.5}Ca_1$ ranges between $Mg_{54.6-56.5}Zn_{41.1-43.0}Ca_{2.4-2.5}$ (Fig4.11), while the composition of the eutectic structure in $Mg_{87.25}Zn_{11.25}Ca_{1.5}$ alloy is in the range of $Mg_{55.7-62.7}Zn_{32.6-42.1}Ca_{2.2-6.2}$ (Fig4.12).

4.3.3 Mechanical properties

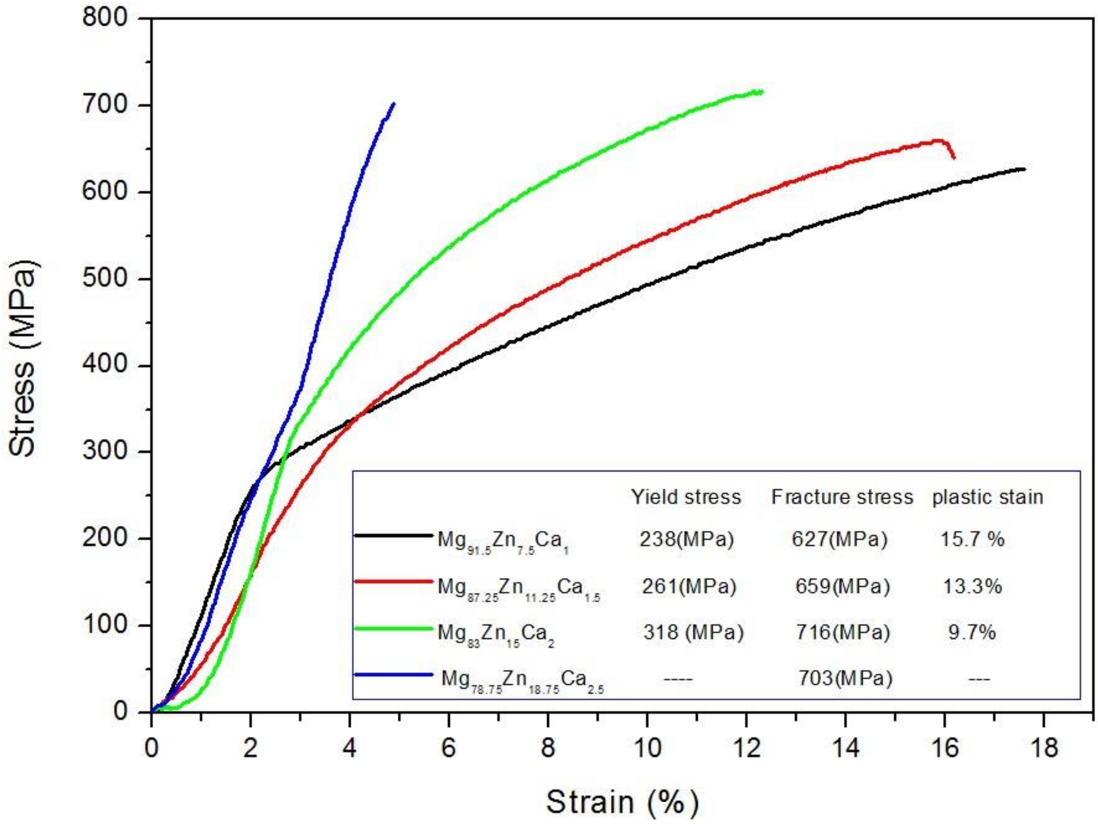

Fig4.13 Compressive stress-strain curves of as-cast Mg-based BMGCs rods at a strain rate of$1.0 \times 10^{-4}s^{-1}$.

The mechanical properties of $Mg_{78.75}Zn_{18.75}Ca_{2.5}$, $Mg_{83}Zn_{15}Ca_2$, $Mg_{87.25}Zn_{11.25}Ca_{1.5}$ and $Mg_{91.5}Zn_{7.5}Ca_1$ were investigated in compression first. The stress-strain curves are displayed in Fig4.13. The $Mg_{78.75}Zn_{18.75}Ca_{2.5}$alloy fractured at 703MPa without any observable plastic deformation. With an increase in the area fraction of α-Mg dendrites, the extent of plasticity prior to failure increases remarkably, but their yield strength and fracture strength decrease accordingly. For $Mg_{87.25}Zn_{11.25}Ca_{1.5}$ alloy, the composite exhibits a yield strength of 318

MPa, a fracture strength of 716MPa and a plastic strain of 9.7%. $Mg_{87.25}Zn_{11.25}Ca_{1.5}$ yields at 261MPa and fractures at 659MPa with a plasticity of 13.3%. $Mg_{91.5}Zn_{7.5}Ca_1$ shows the highest plastic strain of 15.7% with a yield strength of 238MPa and fracture strength of 627MPa. The fact that stress increase with strain indicates that work hardening effect exists in these composites, but not the straining softening as observed in most other BMG composites [20, 21].

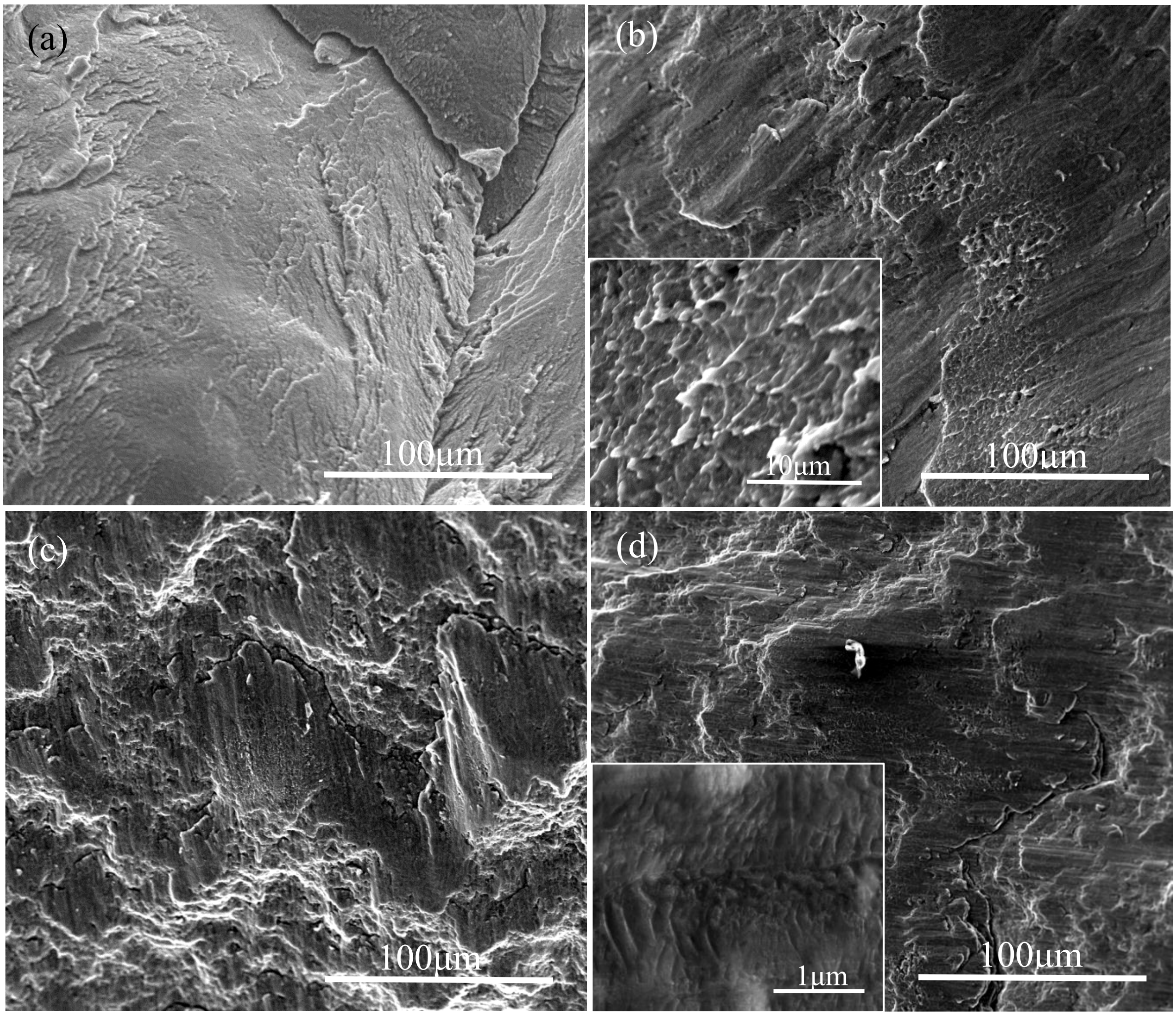

Fig4.14 Compressive fracture morphologies of as-cast: $Mg_{78.75}Zn_{18.75}Ca_{2.5}$ (a), $Mg_{83}Zn_{15}Ca_2$ (b), $Mg_{87.25}Zn_{11.25}Ca_{1.5}$ (c) and $Mg_{91.5}Zn_{7.5}Ca_1$ (d).

The compressive fracture morphologies of the as-cast Mg-based BMGCs are displayed in Fig 4.14. For the $Mg_{78.75}Zn_{18.75}Ca_{2.5}$ alloy, as seen in Fig 4.14a, the smooth and featureless fracture morphology is observed. The large smooth and featherless areas suggest that shear bands propagate in an unimpeded fashion over rather large distances, which is consistent with the shear band propagation behavior of the brittle Mg-based BMG. For the $\mathrm{Mg_{83}\,Zn_{15}\,Ca_2}$ alloy, $\mathrm{Mg_{87.25}Zn_{11.25}Ca_{1.5}}$and $\mathrm{Mg_{91.5}Zn_{7.5}Ca_1}$ alloys, however, well-developed vein patterns have been formed on the fracture surface, but they are not distributed uniformly over the whole fracture surface. Fracture zones of the dendrites isolate the vein pattern into uncontinues zone. With an increase in the volume fraction of dendrites, the area of vein patterns decreases, and the vein pattern becomes finer. At higher magnification, as shown in the inset of Fig4.14b, it can be seen that many molten drops are distributed on the vein pattern, indicating that the composites have undergone extensive melting and resolidification during surface separation. From the inset of Fig 4.14d taken from the fracture region of dendrite, it can be clearly seen that uniformly distributed very fine shear band was observed. These very fine shear bands on the fracture surface demonstrate that the fracture of the composite is controlled not only by the deformation of the glass matrix but also by the deformation of the dendrites [5].

In order to further investigate the deformation behavior of Mg-based BMGCs, nanoindentation and tensile tests were used to study the mechanical properties of$\mathrm{Mg_{87.25}Zn_{11.25}Ca_{1.5}}$ and $\mathrm{Mg_{91.5}Zn_{7.5}Ca_1}$. Nanoindentation results show that the amorphous matrix and the dendrites exhibits huge difference in hardness. As shown in Table4.2 the average hardness, $\mathrm{H_V}$ of the amorphous matrix and dendrites were measured as $\mathrm{H_{V\,amor}}$ 3.55 GPa and $\mathrm{H_{V\,den}}$ 1.38 GPa, respectively.

Table 4.2 Mechanical and material properties of the new composites, hot-extruded pure Mg and WE43 alloy (taken from the literature).

Alloy	UTS(MPa)	ε_{tot}(%)	$R_{P0.2}$(MPa)	E(GPa)	$H_{V\,den}$ (GPa)	$H_{V\,amor}$ (GPa)	$\rho(gcm^{-3})$
$\mathrm{Mg_{91.5}Zn_{7.5}Ca_1}$	466±20.6	14.4±1.6	223±15.6	49	1.38	3.55	1.997±0.033
$\mathrm{Mg_{87.25}Zn_{11.25}Ca_{1.5}}$	455.7±5.7	4.2±0.19	327.3±6.3	54	---	---	2.197±0.041
Hot-extruded Mg	125±4.3	20.1±1.2	30.2±1.5	45	---	---	1.735±0.012
WE43[22],[23]	295	10.7	221	44	---	---	1.84

Fig4.15 shows the true stress-strain curves of tensile tests for the $Mg_{91.5}Zn_{7.5}Ca_1$, $Mg_{87.25}Zn_{11.25}Ca_{1.5}$ and hot-extruded pure Mg. $Mg_{91.5}Zn_{7.5}Ca_1$ alloy yielded at 215MPa. After yielding, this alloy exhibited pronounced work hardening up to a tensile strength 478 MPa and a significant strain of 15.6%. For the $Mg_{87.25}Zn_{11.25}Ca_{1.5}$ alloy, yielding occurred at 332MPa, followed by ~3.9% plastic strain to the ultimate tensile tress of 463MPa. Hot-extruded pure Mg yielded around 30.2MPa and fractured around 125MPa with a strain to failure of 20.1%. The average tensile mechanical properties are summarized in Table 4.1.

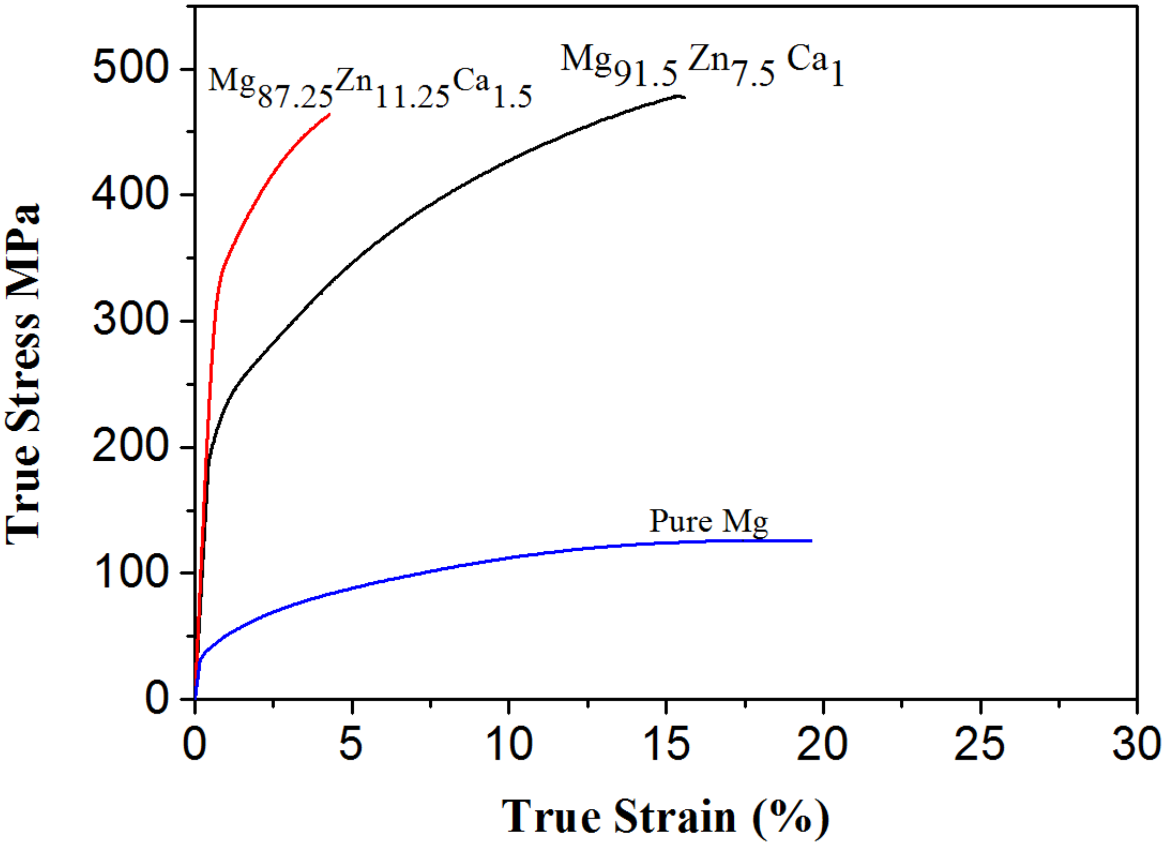

Fig4.15 Room-temperature true stress-strain curves of $Mg_{91.5}Zn_{7.5}Ca_1$, $Mg_{87.25}Zn_{11.25}Ca_{1.5}$ and hot-extruded pure Mg in tension.

A micrograph taken from the fractured tensile $Mg_{91.5}Zn_{7.5}Ca_1$ specimen is shown in Fig4.16a. Dimples were distributed over the whole fracture surface, Fig4.16a, typical of a ductile fracture mechanism. The high magnification image (inset of Fig4.16a) reveals that, instead of the formation of nanometre scale vein pattern observed in Zr-based BMGCs[9], submicron scale dimples were formed. In addition, the dendrites and amorphous/nanocrystalline amorphous/n-

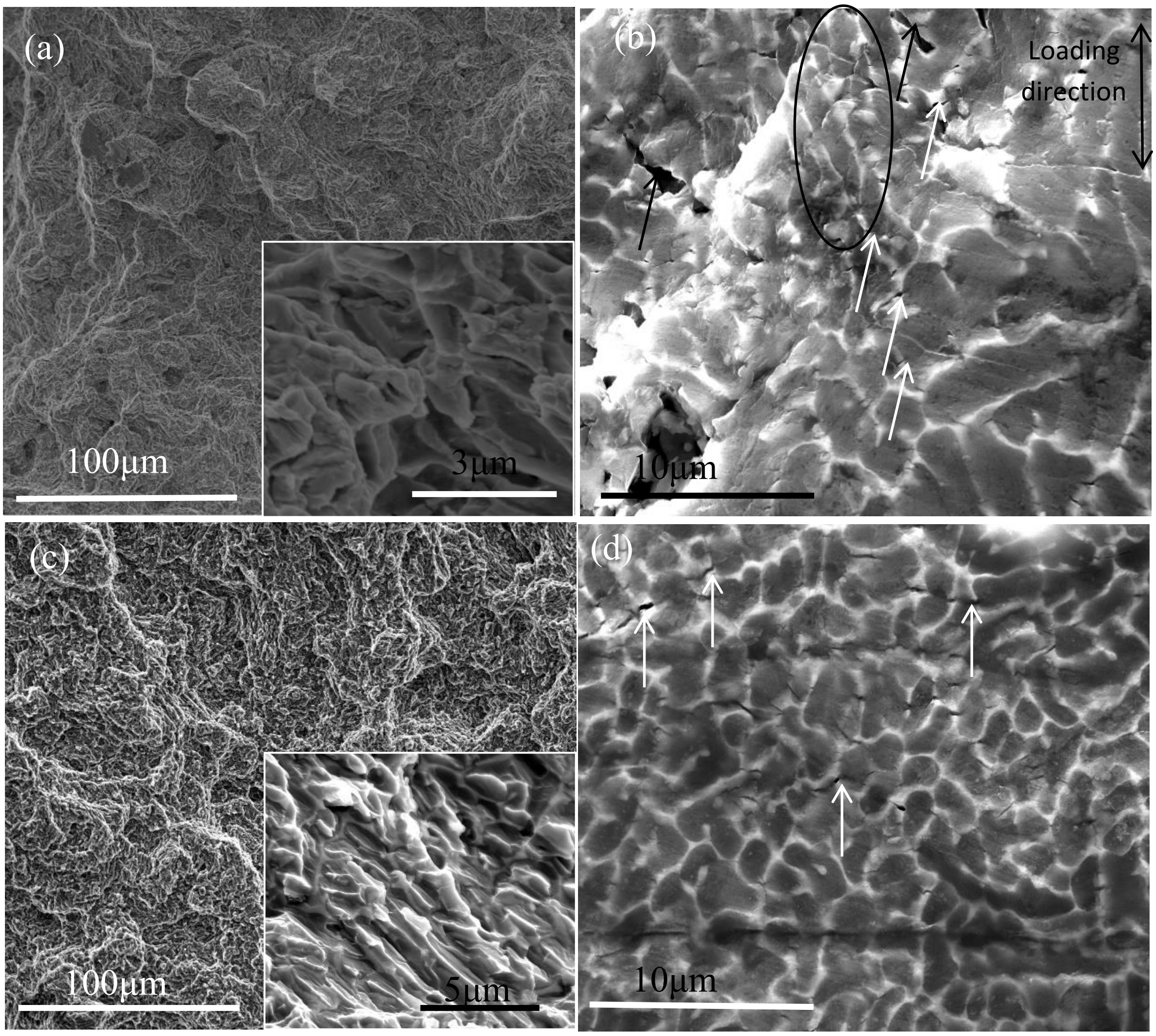

Fig4.16. (a) and (b): $Mg_{91.5}Zn_{7.5}Ca_1$.(a) Dimples distributed over the whole fracture surfaces. (Inset) High magnification micrograph revealing homogenously distributed submicron dimples. (b) Lateral surface microstructure after tension. (c) and (d): $Mg_{87.25}Zn_{11.25}Ca_{1.5}$. (c) Ductile dimple fracture features of $Mg_{87.25}Zn_{11.25}Ca_{1.5}$ at low magnification. (Inset) high magnification micrograph displaying a river pattern fracture surface. (d) Lateral fracture surface revealing that large microcracks formed at relatively thick matrices.

-anocrystalline matrix were elongated (indicated by the black circle in Fig4.16b), suggesting homogeneous deformation. Some microcracks were observed through the amorphous/nanocrystalline matrix Fig4.16b, with this cracking tending to be more frequently in the thicker matrix regions (white arrows). In addition, several large microcracks propagated through the dendrites (indicated by black arrows). The ductile fracture features were also observed in the fracture micrograph of $\mathrm{Mg_{87.25}Zn_{11.25}Ca_{1.5}}$ shown in Fig4.16c at low magnification, but at high magnification (inset of Fig4.16c), instead of the formation of many submicron scale dimples, a river pattern fracture morphology was observed, which suggests a different fracture mechanism to the $\mathrm{Mg_{91.5}\,Zn_{7.5}\,Ca_1}$alloy.

4.4 Discussion

Currently, the dendrite-reinforced ductile BMGCs are generally developed from Zr/Ti-based BMGs, which contain large amount of expensive constituents (Zr,Nb,V etc.) and the toxic Be[7-11]. The addition of Be can prevent the heterogeneous nucleation triggered by the dendrites during quenching [10, 11]. In this chapter a new compositional design approach was used to create tough metallic glass composites consisting of micrometre scale dendrites and nanometre scale amorphous matrices that exhibit high strength and ductility in the normally brittle Be-free MgZnCa metallic glass system. The formation of the microstructure during solidification followed the expected route (shown in Fig4.1b). α-Mg solid solution solidified first from the melt, which is inevitable given the substantial thermodynamic driving force and rapid formation kinetics in the hypoeutectic compositions[5]. Zn and Ca have restricted solubility in the α-Mg, even at high temperature, and therefore they would have partitioned preferentially to the remaining liquid, which can be confirmed by comparing the structure of the ingot alloys with as-cast alloys. Due to the lower cooling rate in the air-cooled ingot alloys, both the size of dendrite and matrix is larger than that of as-cast alloys. The lower cooling rate can facilitate the diffusion of alloying elements during the cooling stage, so a little bit less alloying elements (around 1at%) are observed in the dendrites of the ingot alloys than that in the as-cast alloys. Due to the solubility of both Zn and Ca in c.p.h. Mg is highly restricted even at eutectic temperature, the effect of cooling rate on the partitioning of alloying elements is not quite evident and most of the alloying elements are partitioned to the eutectic structure matrix in ingot alloys and amorphous matrix in as-cast alloys. By controlling the Zn and Ca atomic ratio as close to 7.5 as possible to suppress heterogeneous nucleation of the crystalline matrix, this remaining liquid froze to a predominantly amorphous state instead the formation of the eutectic structure. Fig4.2 shows that the volume fraction of both dendrite and amorphous matrix can be tuned by amount of alloying elements. As the nucleation and growth of a dendrite is time-dependent, the microstructure (size of dendrite and amorphous matrix) can be tuned by varying the composition. The hypoeutectic compositions also imparts low density ($\rho \approx 1.99$g/cc) to the materials by replacing the relatively heavy alloying element with Mg. The formation of nanocrystals in the amorphous matrix was probably unavoidable, but it is likely that a small fraction of nanocrystals increased the strength and global plasticity of the bulk amorphous specimens by promoting the nucleation and multiplication of shear bands [24]. However, an equally important variable is the effect of the thickness of the matrix on deformation mechanisms of the composites, as discussed later.

Fig4.17 summarizes the ultimate strength versus tensile ductility available from the literature for Mg alloys prepared using processing techniques specifically to generate fine structures, including high-ratio differential speed rolling(HRDSR)[25,26],equal channel angular pressing(ECAP)[27,28], cyclic extrusion and compression(CEC)[29],powder metallurgy (PM)[30], hot extrusion(HE)[31,32], accumulative roll bonding(ARB)[33], friction stir processing(FSP)[34], as well as our present tensile result of $\mathrm{Mg}_{91.5}\mathrm{Zn}_{7.5}\mathrm{Ca}_{1}$. The compressive mechanical properties of monolithic $\mathrm{Mg}_{66}\mathrm{Zn}_{30}\mathrm{Ca}_{5}$ and $\mathrm{Mg}_{71}\mathrm{Zn}_{27}\mathrm{Ca}_{4}$ BMGs are also presented in Fig 4.17[6]. As shown in Fig4.17, the majority of the data from the literature are located at the bottom left corner, and a classic trade-off between the strength and ductility is observed in these alloys. The ultrahigh strength is invariably accompanied by very limited ductility in traditional strengthening methods [35] including solid solution atoms, precipitates and dispersed particles, grain boundaries and phase transformation. However, the current result from $Mg_{91.5}Zn_{7.5}Ca_1$ alloy stands out from the trend, suggesting a superior combination of strength and ductility, which indicates that the combination of nanometre scale amorphous matrix with micrometre scale ductile dendrites provides a new way to strengthen materials without significantly sacrificing the ductility. In addition, the mechanical properties of the current alloys compare very favorably with those of conventionally processed Mg alloys. For example, when compared with the well-known rare earth element bearing hot-extruded WE43 alloy, both the tensile strength and ductility of $Mg_{91.5}Zn_{7.5}Ca_1$ are significantly higher

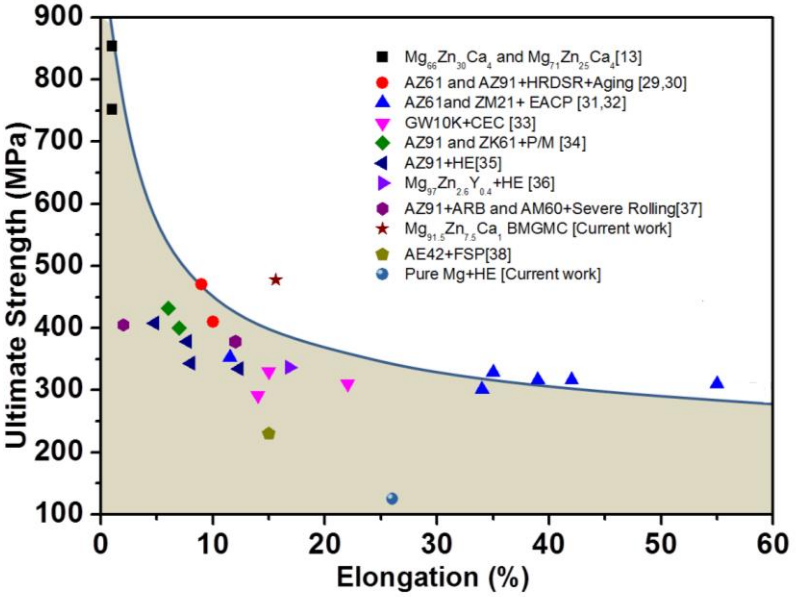

Fig4.17Fracture strength versus tensile ductility of Mg alloys prepared by our current approach and various processing schemes reported in literature. The compressive mechanical properties of Mg_{66} Zn_{30} Ca_4 are also presented.

than that of WE43 alloy, (Table4.1)[22] and moreover, the current BMGC have a density (1.99g/cc) comparable to that of WE43 alloy (1.84g/cc)[23]. To the best of our knowledge, the present $\mathrm{Mg}_{91.5}\,\mathrm{Zn}_{7.5}\,\mathrm{Ca}_{1}$ exhibits the largest plastic strain observed for such materials, even compared with the best Ti-based BMGCs with reported highest tensile fracture strain (~15.5%)[9]. It is the first time that Mg-based BMGCs that exhibit significant tensile ductility have been reported.

The dimples on the fracture surface (Fig4.16a) indicates that the dendrites underwent extensive deformation, giving a similar appearance to the tensile fracture surface of hot-extruded AZ31 alloy [36]. It is well known that the ductility of BMGCs can be ascribed to the ductile dendritic crystalline phase, which stabilizes against the shear localization and propagation of critical shear bands upon loading [37]. However, in the current work, no shear bands were observed on the tensile fracture surface. During the tensile test, the softer dendrite phase is expected to yield first. Qiao et al. reported the tensile curve for a Ti-based BMGCs can be divided into three sections of (1) elastic deformation, (2) work-hardening, and (3) softening[9]. In the first section, both the dendrites and the amorphous matrix deform elastically. Work hardening is then associated with plastic deformation of one phase, but continuing elastic deformation of the other. Finally, softening is associated with plastic deformation in both phases. For the Ti/Zr-based BMGCs, the softening component dominates the tensile deformation and always starts after about 1% plastic strain. This indicates that softening through shear banding is initiated in the amorphous phase at low strains, which leads to continuous necking. In contrast, in the current work, no softening was observed in the tensile test curves, Fig4.15, rather, work hardening prevailed to failure. The high ductility and excellent work-hardening capability of $\mathrm{Mg}_{91.5}\,\mathrm{Zn}_{7.5}\,\mathrm{Ca}_{1}$alloy can be interpreted by considering the BMGCs as a combination of the nanometer scale metallic glass matrix with a ductile dendritic structure. In the initial stage of deformation, the Mg dendrites yield first. The $\mathrm{Mg}_{87.25}\mathrm{Zn}_{11.25}\mathrm{Ca}_{1.5}$ alloy has a smaller dendrite size and higher volume fraction of amorphous matrix, leading to the higher yield strength in tension than observed for the $\mathrm{Mg_{91.5}\,Zn_{7.5}\,Ca_1}$alloy [38,39]. Similar trend can also be found in the compressive stress-strain curves shown Fig4.13. Especially for $\mathrm{Mg_{78.75}\,Zn_{18.75}\,Ca_{2.5}}$alloy, the yielding strength can be a high as 700MPa, due to its fine Mg dendrite structure and large volume fraction of amorphous matrix. With increasing applied stress, the amorphous matrix started to yield (observed in $\mathrm{Mg_{91.5}\,Zn_{7.5}\,Ca_1}$ alloy in tension). However, no evidence was found that the deformation of the nanometer scale amorphous matrix in $\mathrm{Mg_{91.5}\,Zn_{7.5}\,Ca_1}$alloy occurred through the formation of shear-bands, rather, deformation appears to have been homogenous. As proposed by Jang and Volkert[18, 40], the stress required to activate a pre-existing shear band to fracture is:

$$\sigma=\sqrt{\frac{2\sqrt{2}\Gamma\mathrm{E}}{\mathrm{ad}}} \tag{4.1}$$

Where Γ is the energy per unit area of shear band, E is Young's modulus, a is the aspect ratio height over diameter and d is the diameter. The shear band activation stress gradually increases with decreasing specimen diameter. The stress required to initiate homogenous flow is independent of sample size and is in the range of the elastic limit at room temperature and ideal strength (~E/30). In order to estimate the critical diameter (d*) at which the deformation mechanism transfers from shear banding to homogenous flow, the mechanical properties of monolithic $\mathrm{Mg_{66}Zn_{30}Ca_4}$ BMG (yield strength 930MPa, Young's Modulus 48GPa) are used [6, 41]. Γ is estimated to be 3.3 $\mathrm{Jm^{-2}}$ by equating the elastic energy exerted on the column ($\pi\sigma\varepsilon r^2 h/2$) with the increase in shear band energy ($\sqrt{2}\,\pi\, r^2\,\Gamma$)[44]. The d* is calculated to be between ~43 and 129nm by using Γ=3.3 Jm^{-2}, a=4 and E=48GPa, which equates well with the observation of homogeneous deformation in the two alloys in the current study, where the thickness of the amorphous matrices for $\mathrm{Mg_{91.5}\,Zn_{7.5}\,Ca_1}$ alloy varies over 80-530nm. In contrast, the thickness of the amorphous matrix for $\mathrm{Mg_{87.25}Zn_{11.25}Ca_{1.5}}$ alloy was is in the range of 0.4-15.3μm. The evidence was that microcracks were formed immediately after the yielding of amorphous matrix, which leads to the early failure by the rapid propagation of the microcracks from the interface to dendrites (indicated by white arrows in Fig 4.16(d)).

It is worth considering the wider impacts of the current work. The new composition design method is applicable to other BMGCs systems provided several criteria are met: the BMG system has robust glass forming ability and the alloying elemental additions should have restricted solubility in the alloy system. Both the low density and cheap constituent elements will favour these materials in engineering applications. The deformation behavior of $\mathrm{Mg_{91.5}Zn_{7.5}Ca_1}$ alloy consisting of micrometre scale dendrites and nanometre scale amorphous matrix provides a new approach to strengthen materials without significantly sacrificing ductility.

4.5 Conclusions

In this chapter, we proposed a new composition design method to create BMGCs with high strength, large ductility and excellent work hardening from the brittle MgZnCa system. By appropriate choice of alloying elements and composition, the volume fraction, size of both the dendrites and amorphous matrix can be effectively tuned by the variation of the composition, and the yield strength, fracture strength and ductility also varies accordingly. As the current Mg alloys are substantially hypoeutectic in chemical composition, α-Mg solid solution will solidify first from the melt upon solidification. The alloying elements Zn and Ca, which have restricted solubility in the equilibrium α-Mg, partition preferentially to the remaining liquid. The remaining liquid will freeze into an amorphous state when it is close enough to the (near) eutectic bulk glass forming composition. The increase in alloying elements results in an increase in the volume fraction of amorphous matrix and a decrease in the dendrite size, which leads the higher yielding strength but lower ductility. HRTEM analysis demonstrated that the $Mg_{91.5}Zn_{7.5}Ca_1$ alloy consists of micrometre scale α-Mg solid solution dendrites and nanometre scale amorphous matrix. The mechanical properties of current Mg alloy can be interpreted by considering the BMGCs as a combination of the nanometer scale metallic glass matrix with a ductile dendritic structure. The high strength, large ductility and excellent work hardening observed in the $Mg_{91.5}Zn_{7.5}Ca_1$ can be attributed the homogeneous deformation of nanometre scale amorphous matrices, which delays the formation and rapid propagation of microcracks from the interface.

4.6 References

[1] R.O. Ritchie, The conflicts between strength and toughness, Nat. Mater., 10 (2011) 817-822.

[2] D. Jang, J.R. Greer, Transition from a strong-yet-brittle to a stronger-and-ductile state by size reduction of metallic glasses, Nat. Mater., 9 (2010) 215-219.

[3] A. Inoue, Stabilization of metallic supercooled liquid and bulk amorphous alloys, Acta Mater., 48 (2000) 279-306.

[4] M.F. Ashby, A.L. Greer, Metallic glasses as structural materials, Scripta Mater., 54 (2006) 321-326.

[5] W.H. Wang, The elastic properties, elastic models and elastic perspectives of metallic glasses, Prog. Mater. Sci., 57 (2012) 487-656.

[6] A.L. Greer, Metallic glasses: Damage tolerance at a price, Nat. Mater., 10 (2011) 88-89.

[7] S.S. Chen, H.R. Zhang, I. Todd, Phase-separation-enhanced plasticity in a $Cu_{47.2}Zr_{46.5}Al_{5.5}Nb_{0.8}$ bulk metallic glass, Scripta Mater., 72–73 (2014) 47-50.

[8] C.A. Schuh, T.C. Hufnagel, U. Ramamurty, Mechanical behavior of amorphous alloys, Acta Mater., 55 (2007) 4067-4109.

[9] R.L. Narayan, P.S. Singh, D.C. Hofmann, N. Hutchinson, K.M. Flores, U. Ramamurty, On the microstructure–tensile property correlations in bulk metallic glass matrix composites with crystalline dendrites, Acta Mater., 60 (2012) 5089-5100.

[10] J.J. Lewandowski, W.H. Wang, A.L. Greer, Intrinsic plasticity or brittleness of metallic glasses, Phil.Mag.Lett., 85 (2005) 77-87.

[11] A. Inoue, K. Ohtera, K. Kita, T. Masumoto, New amorphous Mg-Ce-Ni alloys with high strength and good ductility, Japanese J. Appl. Phys., 27 (1988) 2248-2251.

[12] X. Hui, W. Dong, G.L. Chen, K.F. Yao, Formation, microstructure and properties of long-period order structure reinforced Mg-based bulk metallic glass composites, Acta Mater., 55 (2007) 907-920.

[13] Y.Y. Zhao, E. Ma, J. Xu, Reliability of compressive fracture strength of Mg–Zn–Ca bulk metallic glasses: Flaw sensitivity and Weibull statistics, Scripta Mater., 58 (2008) 496-499.

[14] D.C. Hofmann, J.-Y. Suh, A. Wiest, G. Duan, M.-L. Lind, M.D. Demetriou, W.L. Johnson, Designing metallic glass matrix composites with high toughness and tensile ductility, Nature, 451 (2008) 1085-1089.

[15] F. Guo, H.J. Wang, S.J. Poon, G.J. Shiflet, Ductile titanium-based glassy alloy ingots, Appl.Phys.Lett., 86 (2005)091907-3.

[16] J.W. Qiao, A.C. Sun, E.W. Huang, Y. Zhang, P.K. Liaw, C.P. Chuang, Tensile deformation micromechanisms for bulk metallic glass matrix composites: From work-hardening to softening, Acta Mater., 59 (2011) 4126-4137.

[17] D.C. Hofmann, Bulk Metallic Glasses and Their Composites: A Brief History of Diverging Fields, J. Mater., 2013 (2013)1- 8.

[18] D.C. Hofmann, Shape Memory Bulk Metallic Glass Composites, Science, 329 (2010) 1294-1295.

[19] W. Xu, R. Zheng, K.J. Laws, S.P. Ringer, M. Ferry, In situ formation of crystalline flakes in Mg-based metallic glass composites by controlled inoculation, Acta Mater., 59 (2011) 7776-7786.

[20] Y.Y. Zhao, H. Men, D. Estévez, Y. Liu, X. Wang, R.-W. Li, C. Chang, Mg-based bulk metallic glass composite containing in situ microsized quasicrystalline particles, Scripta Mater., 78–79 (2014) 21-24.

[21] G. Chen, X.L. Zhang, C.T. Liu, High strength and plastic strain of Mg-based bulk metallic glass composite containing in situ formed intermetallic phases, Scripta Mater., 68 (2013) 150-153.

[22] Y.K. Xu, H. Ma, J. Xu, E. Ma, Mg-based bulk metallic glass composites with plasticity and gigapascal strength, Acta Mater., 53 (2005) 1857-1866.

[23] D.G. Pan, H.F. Zhang, A.M. Wang, Z.Q. Hu, Enhanced plasticity in Mg-based bulk metallic glass composite reinforced with ductile Nb particles, Appl.Phys.Lett., 89 (2006) 261904-3.

[24] Y. Wu, Y. Xiao, G. Chen, C.T. Liu, Z. Lu, Bulk Metallic Glass Composites with Transformation-Mediated Work-Hardening and Ductility, Adv. Mater., 22 (2010) 2770-2773.

[25] S. Wasiur-Rahman, M. Medraj, Critical assessment and thermodynamic modeling of the binary Mg–Zn, Ca–Zn and ternary Mg–Ca–Zn systems, Intermetallics, 17 (2009) 847-864.

[26] T.G. Nieh, J. Wadsworth, C.T. Liu, T. Ohkubo, Y. Hirotsu, Plasticity and structural instability in a bulk metallic glass deformed in the supercooled liquid region, Acta Mater., 49 (2001) 2887-2896.

[27] C. Fan, H. Li, L.J. Kecskes, K. Tao, H. Choo, P.K. Liaw, C.T. Liu, Mechanical Behavior of Bulk Amorphous Alloys Reinforced by Ductile Particles at Cryogenic Temperatures,Phys. Rev. Lett., 96 (2006) 145506-4.

[28] X. Zhang, G. Yuan, L. Mao, J. Niu, W. Ding, Biocorrosion properties of as-extruded Mg–Nd–Zn–Zr alloy compared with commercial AZ31 and WE43 alloys, Mater. Lett., 66 (2012) 209-211.

[29] Y. Chen, Z. Xu, C. Smith, J. Sankar, Recent advances on the development of magnesium alloys for biodegradable implants, Acta Biomater., 10 (2014) 4561-4573.

[30] Das J.Kim KB, Wei BC, Zhang ZF, Wang WH, et al, Dutile metallic glass in supercooled martensic alloy, Mater. Trans. JIM 47 (2006) 2606–2609

[31] W.J. Kim, S.I. Hong, Y.H. Kim, Enhancement of the strain hardening ability in ultrafine grained Mg alloys with high strength, Scripta Mater., 67 (2012) 689-692.

[32] W.J. Kim, I.B. Park, S.H. Han, Formation of a nanocomposite-like microstructure in Mg–6Al–1Zn alloy, Scripta Mater., 66 (2012) 590-593.

[33] W.J. Kim, S.I. Hong, Y.S. Kim, S.H. Min, H.T. Jeong, J.D. Lee, Texture development and its effect on mechanical properties of an AZ61 Mg alloy fabricated by equal channel angular pressing, Acta Mater., 51 (2003) 3293-3307.

[34] Q. Ge, D. Dellasega, A.G. Demir, M. Vedani, The processing of ultrafine-grained Mg tubes for biodegradable stents, Acta Biomater., 9 (2013) 8604-8610.

[35] T. Peng, Q. Wang, J. Lin, M. Liu, H.J. Roven, Microstructure and enhanced mechanical properties of an Mg–10Gd–2Y–0.5Zr alloy processed by cyclic extrusion and compression, Mater. Sci. Eng.: A, 528 (2011) 1143-1148.

[36] K. Kubota, M. Mabuchi, K. Higashi, Review Processing and mechanical properties of fine-grained magnesium alloys, J. Mater. Sci., 34 (1999) 2255-2262.

[37] H. Somekawa, A. Singh, T. Mukai, High fracture toughness of extruded Mg–Zn–Y alloy by the synergistic effect of grain refinement and dispersion of quasicrystalline phase, Scripta Mater., 56 (2007) 1091-1094.

[38] K.K. Mamoru Mabuchi, Kenji Higashi, New Recycling Process by Extrusion for Machined Chips of AZ91 Magnesium and Mechanical Properties of Extruded Bars Materials, Mater.Trans.JIM, 36 (1995) 1249-1254.

[39] M.T. Pérez-Prado, J.A. del Valle, O.A. Ruano, Achieving high strength in commercial Mg cast alloys through large strain rolling, Mater. Lett. 59 (2005) 3299-3303.

[40] H.S. Arora, H.S. Grewal, H. Singh, B.K. Dhindaw, D. McPhail, B. Shollock, R. Chater, S. Mukherjee, Microstructure-Property Relationship for Friction Stir Processed Magnesium Alloy Adv. Eng. Mater., 16 (2014) 94-102.

[41] H. Kou, J. Lu, Y. Li, High-Strength and High-Ductility Nanostructured and Amorphous Metallic Materials, Adv. Mater., 26 (2014) 5518-5524.

[42] L. Lu, T. Liu, Y. Chen, Z. Wang, Deformation and fracture behavior of hot extruded Mg alloys AZ31,Mater. Charact., 67 (2012) 93-100.

[43] C.C. Hays, C.P. Kim, W.L. Johnson, Microstructure Controlled Shear Band Pattern Formation and Enhanced Plasticity of Bulk Metallic Glasses Containing in situ Formed Ductile Phase Dendrite Dispersions, Phys. Rev. Lett., 84 (2000) 2901-4.

[44] F. Abdeljawad, M. Haataja, Continuum Modeling of Bulk Metallic Glasses and Composites,Phys. Rev. Lett., 105 (2010) 125503-4.

[45] F. Abdeljawad, M. Fontus, M. Haataja, Ductility of bulk metallic glass composites: Microstructural effects, Appl.Phys.Lett., 98 (2011) 031909-3.

[46] C.A. Volkert, A. Donohue, F. Spaepen, Effect of sample size on deformation in amorphous metals, J. Appl. Phys., 103 (2008) 083539-6.

[47] B. Zberg, P.J. Uggowitzer, J.F. Loffler, MgZnCa glasses without clinically observable hydrogen evolution for biodegradable implants, Nat. Mater., 8 (2009) 887-891

Chapter 5

Inhomogeneous structure mediated work hardening and uniform elongation in in-situ-cast nanostructured CuZrTi alloy

Abstract

Bulk nanostructured materials (NMs) have ultrahigh strength but low ductility, especially in tension. NMs generally undergo inhomogeneous plastic deformation under loading at room temperature due to plastic instability originating from the lack of an effective hardening mechanism. In this chapter, a new strategy is presented to design defect-free in-situ-cast two-phase nanostructured CuZrTi alloys by appropriate choice of alloying elements and compositions. X-ray diffraction (XRD) and transmission electron microscopy (TEM) analysis showed that the alloys consisted of softer Cu solid solution with numerous uniformly distributed $\mathrm{Cu_3Ti}$ intragranular nanoprecipitates and harder nanoscale $\mathrm{Cu_{51}Zr_{14}}$ matrix embedded with some retained $\mathrm{Cu_5Zr}$. The $\mathrm{Cu_{90.5}Zr_{7.5}Ti_2}$ alloy exhibited a yield strength of 787MPa, a fracture strength of 1221MPa and room temperature tensile uniform ductility of 5.16%, exhibiting ultrahigh strength and large uniform elongation simultaneously. The average hardness of the softer Cu solid solution and harder $\mathrm{Cu_{51}Zr_{14}}$ phase was measured by nanoindentation as 3.30±0.55GPa and 9.17±0.64GPa, respectively. The specific structure of these alloys, namely the uniform distribution ultrafine softer Cu with frequent intragranular nanoprecipitates in the nanoscale harder $\mathrm{Cu_{51}Zr_{14}}$ matrix embedded with$\mathrm{Cu_5Zr}$, is responsible for the large uniform elongation accompanied with ultrahigh strength.

5.1 Introduction

Since nanostructured materials (NMs) (a microstructure less than 100nm in at least one dimension) were first defined by Gleiter[1, 2], study in NMs has flourished over the last three decades[1]. Bulk NMs are generally produced either through a multiple processing steps such as the synthesis and consolidation of nanoparticles (e.g. via inert-gas condensation)[2,3] or nanocrystalline powders (e.g. via ball milling or cryomilling)[1, 4], or by employing techniques that are not easily commercially viable such as severe plastic deformation[5-7]. NMs produced by multiple processing steps often have defects, such as porosity, incomplete bonding and impurities, which cause premature failure under tension, sometimes even before the onset of yielding[3]. In comparison, severe plastic deformation, such as equal channel angle extrusion (ECAP) and high pressure torsion (HPT), can synthesize flaw-free NMs that exhibit higher ductility than those synthesized by a multiple-step approach [8]. However, even these fully dense NMs often exhibit a very low or near-zero uniform tensile elongation (strain before necking) due to their poor strain hardening capacity [9]. Uniform elongation can more accurately represent the real ductility of NMs than elongation to failure because uniform elongation is less affected by the gauge length [10]. The large post-necking strain often imparts a false impression of high ductility in NMs as most of them have a very short gauge length. A high work-hardening rate is essential for improving the uniform elongation because it can help delay localized deformation under tensile stress [10]. However, NMs often have a low or no work-hardening because dislocation multiplication/accumulation is severely confined by the nanometre-scale geometries [11, 12] and the absence of defects in grain interior to interact with dislocations [13]. Upon straining, the dislocations present in a small volume can run out of the sample body freely, causing dislocation starvation [13], so that continued plastic deformation can be expected to be source-controlled.

Recently, various strategies have been reported to improve the ductility and toughness of NMs, such as bimodal grain size [9, 14], nanopreciptates[10, 15-17], nanoparticles[18] and pre-existing growth twins (PGTs)[19]. Among these, PGTs and intragranular nanoprecipitates[10, 20] are the most widely studied because they possess specific interactions with the dislocation motion like the conventional grain boundary or precipitates to enhance the strength[21, 22], and it is also a slip plane, which could accommodate or be penetrated by dislocations to improve the ductility[11, 21]. Intragranular nanoprecipitates help with the multiplication and storage of dislocations, which increases the work-hardening rate [10, 20]. Nevertheless, it still remains challenging to enhance the uniform tensile elongation in bulk NMs due to the difficulties to embed toughening mechanisms such as PGTs and nanoprecipites in bulk NMs[23]. In practice, PGTs often occur in eletrodeposited thin films and the characterized non-equilibrium grain boundaries in ultrafine alloys or precipitation in NMs will predominantly be intergranular instead of intragranular precipitation even at room temperature [17].

5.2 Alloys Design

In the current work, a general approach is presented for designing defect-free two-phase NMs in CuZrTi alloy by controlling of diffusion growth of primary Cu phase through appropriate choice of alloying elements and composition. CuZr system has been well known to form metallic glass in a wide composition range (25 at% to 72 at% copper), indicating the high content of Zr tends to stabilize the CuZr liquid even at low temperature. Atomistic simulation shows the atom mobility exhibits strong compositional dependence in CuZr alloy, with both Cu and Zr atoms exhibiting minimum diffusivities at ~70at% Cu at 1100K (at least slowed by one magnitude for Cu atoms)[24]. The atom mobility in supercooled CuZr alloys are significantly slowed by icosahedral-coordinated clusters [25, 26], which tends to agglomerate and form medium-range order, thereby further reducing atomic mobility in the liquid[27].

Zr has negligible solubility in the equilibrium face centred cubic (f.c.c.) Cu (the maximum Zr solubility in Cu is 0.12 at.% at 972 ℃)[28, 29]. The current CuZr alloys ($Cu_{92.5}Zr_{7.5}$, $Cu_{90.5}Zr_{7.5}Ti_2$ and $Cu_{90}Zr_8Ti_2$) are slightly hypereutectic in chemical composition in the light of CuZr phase diagram (eutectic point $Cu_{92.8}Zr_{7.2}$) [29]. However, according to the CuTi phase diagram[30, 31], the eutectic point in the Cu rich corner is around 20at.% Ti, so the alloys ($Cu_{90.5}Zr_{7.5}Ti_2$ and $Cu_{90}Zr_8Ti_2$) in this work are substantially hypoeutectic in chemical composition in the CuTi phase diagram. Therefore, the primary Cu dendrites tend to solidify first from the melt with 2at.% Ti. Ti content is fixed at 2at.% under the flowing three considerations: (i) the addition of 2at.% Ti is enough to form supersaturated Cu solid solution as the solubility of Ti in Cu is less than 1at% at 500℃; (ii) according to our results, 2at.% Ti is effectively enough to stabilize the primary Cu dendrites during solidification and without the formation of any coarse CuTi intermetallic. It is believed that a large quantity of Ti atoms are dissolved into the Cu lattice to form super solid solution due to the high cooling rate and are beneficial in the formation of nano-precipitates of Cu dendrites. Zr has negligible solubility at the eutectic temperature in the equilibrium f.c.c. Cu and thus is expected to partition preferentially to the remaining liquid during the initial stage of solidification, so that the remaining liquid becomes enriched in Zr, which should restrict the growth of primary Cu dendrites due to the poor mobility of Cu and Zr in the supercooled Zr-rich liquid. The solidification of ultrafine/nanoscale Cu crystals in the remaining Zr-rich liquid is expected to proceed after the solidification of the primary Cu dendrites due to the increase of viscosity (poorer mobility of Zr and Cu) in the remaining liquid. The formation of nanometre Cu crystals further leads to the enrichment of alloying elements in the rest liquid, which should freeze into a hard CuZr phase.

5.3 Results

5.3.1 Microstructures of ingots CuZrTi alloys

Figs5.1 and 5.2 shows the SEM images and XRD patterns of the $Cu_{90.5}Zr_{7.5}Ti_2$ (a), $Cu_{90}Zr_8Ti_2$ (b) and $Cu_{92.5}Zr_{7.5}$ (c and d) ingots. All ingots with a weight of 3g were alloyed in a water-cooled Cu crucible by arc melting. The ingot pellets had a nominal diameter of 10mm and a height of 4mm. The backscattered electron SEM image of $Cu_{90.5}Zr_{7.5}Ti_2$ shows a coarse dendritic phase dispersed in ultrafine/fine structure regions (indicated in Fig5.1a). For the $Cu_{90.5}Zr_{7.5}Ti_2$ alloy (Fig5.1a), the microstructure was mainly composed of coarse primary Cu solid solution dendrites, typical binary ultrafine (indicated by black circles in Fig5.1a) and fine structures (indicated by blue circles in Fig5.1a). The ultrafine structure adopted a lamellar shape. From the XRD pattern shown in Fig5.2a, it is shown that the microstructure was composed of f.c.c.(face-centred cubic) Cu and Cu_5Zr. The fine structure region was generally distributed between the ultrafine structure and coarse primary Cu dendrites, as shown in Fig5.1a. The size of primary Cu dendrites for $Cu_{90.5}Zr_{7.5}Ti_2$ varied between 10 and 36μm while the size of Cu in the fine structure varies over 0.5-15μm. The thicknesses of lamellar Cu and Cu_5Zr in the ultrafine structure were around 0.7μm and 0.5μm respectively. Fig5.1b shows the microstructure of $Cu_{90}Zr_8Ti_2$ alloy. The $Cu_{90}Zr_8Ti_2$alloy had a similar structure to the $Cu_{90.5}Zr_{7.5}Ti_2$ alloy, comprising coarse primary Cu dendrites, fine and ultrafine structure but the coarse primary Cu dendrites (with width ranges from 0.6μm to 3.9μm) and fine structure are much smaller than that of $Cu_{90.5}Zr_{7.5}Ti_2$. Instead of the formation lamella, an ultrafine structure was observed in the $Cu_{90.5}Zr_{7.5}Ti_2$ alloy, approximately spherical ultrafine Cu solid solution (0.8μm-1.5μm in diameter) uniformly distributed in the Cu_5Zr matrix was observed (shown in the inset of Fig5.1b). As can be seen in Fig5.1b, the ingot of $Cu_{90}Zr_8Ti_2$ alloy was mainly composed of fine structure. XRD patterns shown in Fig5.2 shows that both alloys are comprised of the same phases (Cu+Cu_5Zr). In order to further identify the microstructure,

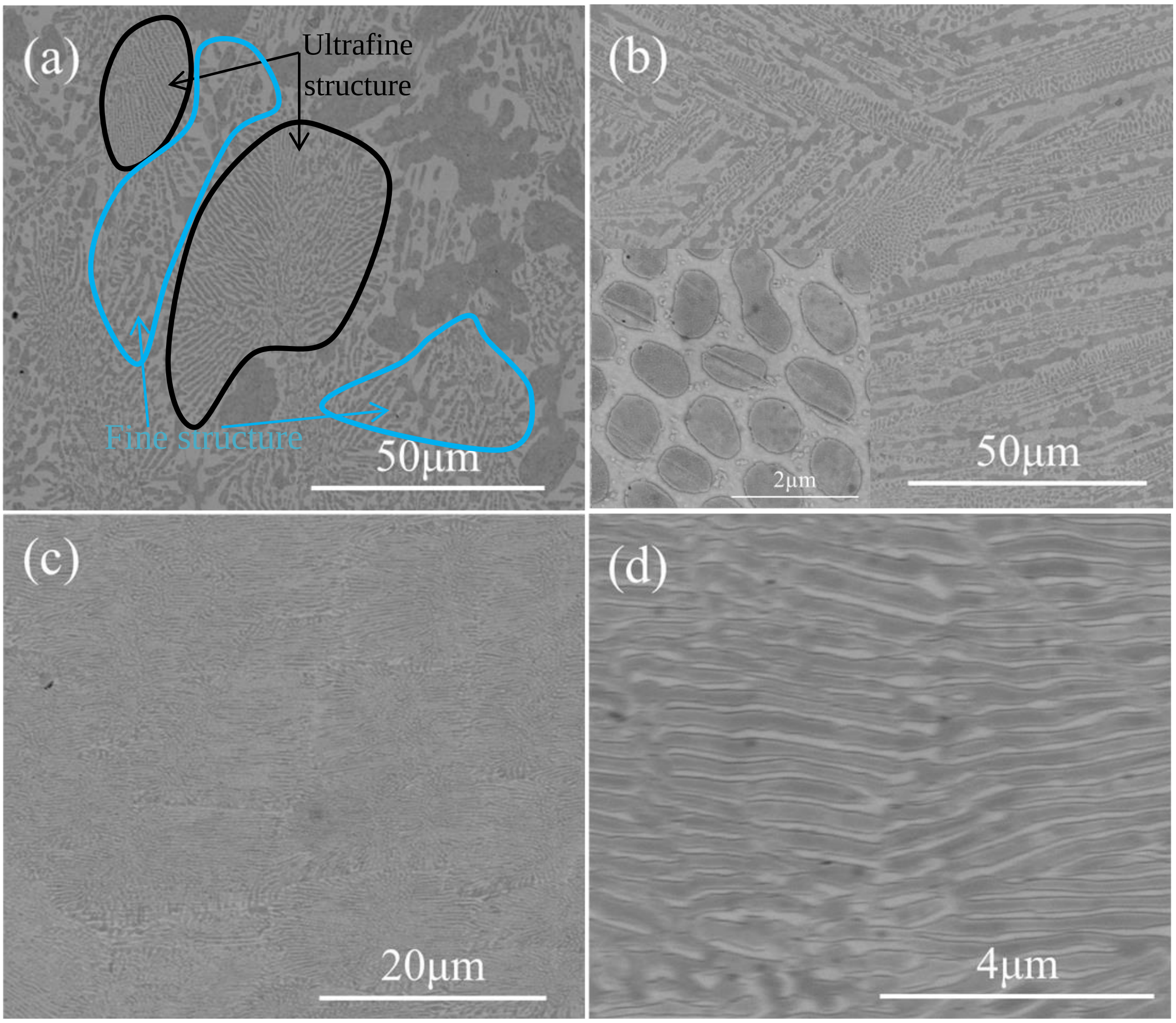

Fig5.1. Back-scattered SEM micrographs of ingot samples:(a) $Cu_{90.5}Zr_{7.5}Ti_2$; (b) $Cu_{90}Zr_8Ti_2$;(c)and(d) $Cu_{92.5}Zr_{7.5}$,(c) low magnification, (d)high magnification.

EDS analysis was performed on $Cu_{90.5}Zr_{7.5}Ti_2$ ingot alloy. According to the data shown in table 5.1, the coarse grey phase had a composition of $Cu_{96.1\pm0.7}Zr_{0.6\pm0.2}Ti_{3.3\pm0.6}$, while the relatively lighter phase had a composition of $Cu_{78.4\pm0.8}Zr_{17.8\pm0.2}Ti_{3.88\pm0.5}$. These EDS analysis further confirmed that the coarse grey phase is a Cu solid solution, while the relatively lighter phase is Cu_5Zr as the atomic percentage of Zr is 17.8%, which is very close with the stoichiometry of the Cu_5Zr phase. The microstructure of the $Cu_{92.5}Zr_{7.5}$ is presented in Fig5.1c and d. As can be observed in Fig5.1c and d, $Cu_{92.5}Zr_{7.5}$ shows an ultrafine typical lamella eutectic structure. The thickness of the Cu lamella varied over 100nm to 300nm, while the Cu_5Zr lamellar ranged over 60-120nm in thickness. Although 2at.% more Cu was added to the $Cu_{92.5}Zr_{7.5}$ alloy, the peaks corresponding to f.c.c. Cu are not as strong as that in $Cu_{90.5}Zr_{7.5}Ti_2$ (Fig5.2), which could be attributed to the much finer eutectic structure of $Cu_{92.5}Zr_{7.5}$ alloy and the formation of coarse primary Cu dendrites in the $Cu_{90.5}Zr_{7.5}Ti_2$ alloy due to the addition of Ti.

Table 5.1 EDS results for the phases in the ingot of $Cu_{90.5}Zr_{7.5}Ti_2$ alloy.

Phase	**Cu(at%)**	**Zr(at%)**	**Ti(at%)**
Grey	96.1±0.7	0.7±0.3	3.3±0.6
Bright	78.4±0.8	17.8±0.2	3.9±0.5

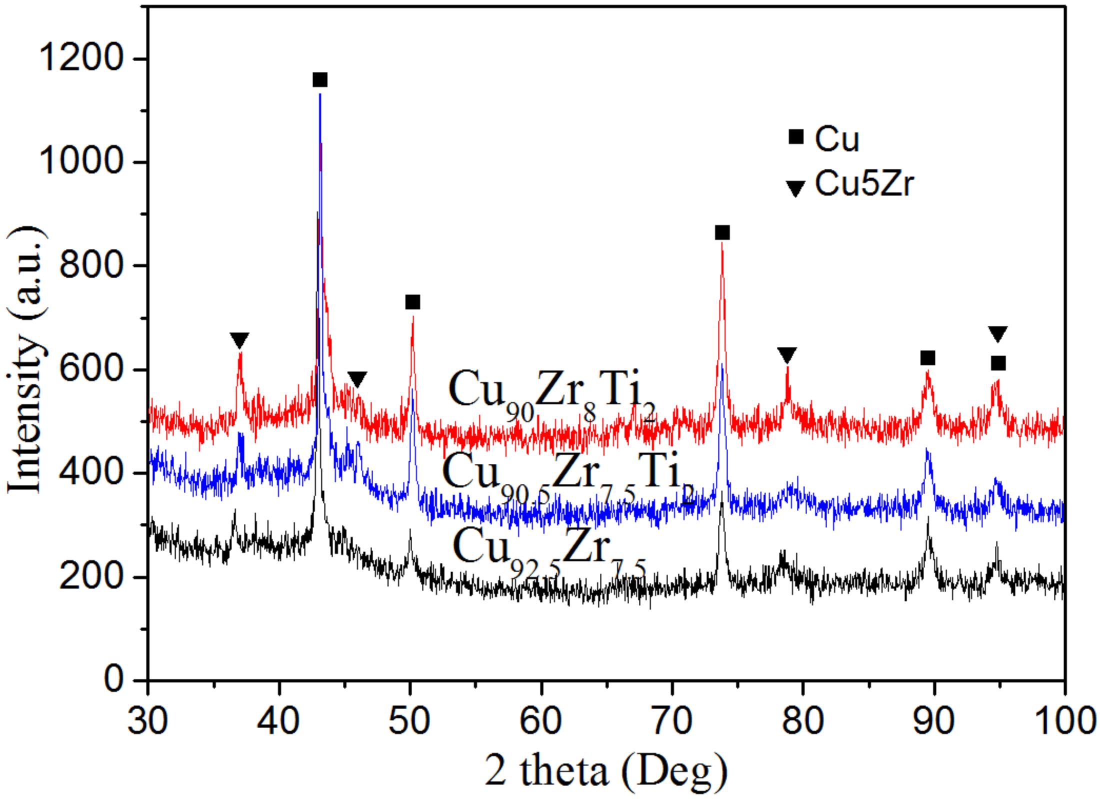

Fig5.2. XRD patterns of the ingots of $Cu_{90}Zr_8Ti_2$, $Cu_{90.5}Zr_{7.5}Ti_2$ and $Cu_{92.5}Zr_{7.5}$ alloys with a diameter of 10mm and a height of 4mm.

5.3.2 Microstructures of as-cast 2mm-diameter CuZrTi alloys

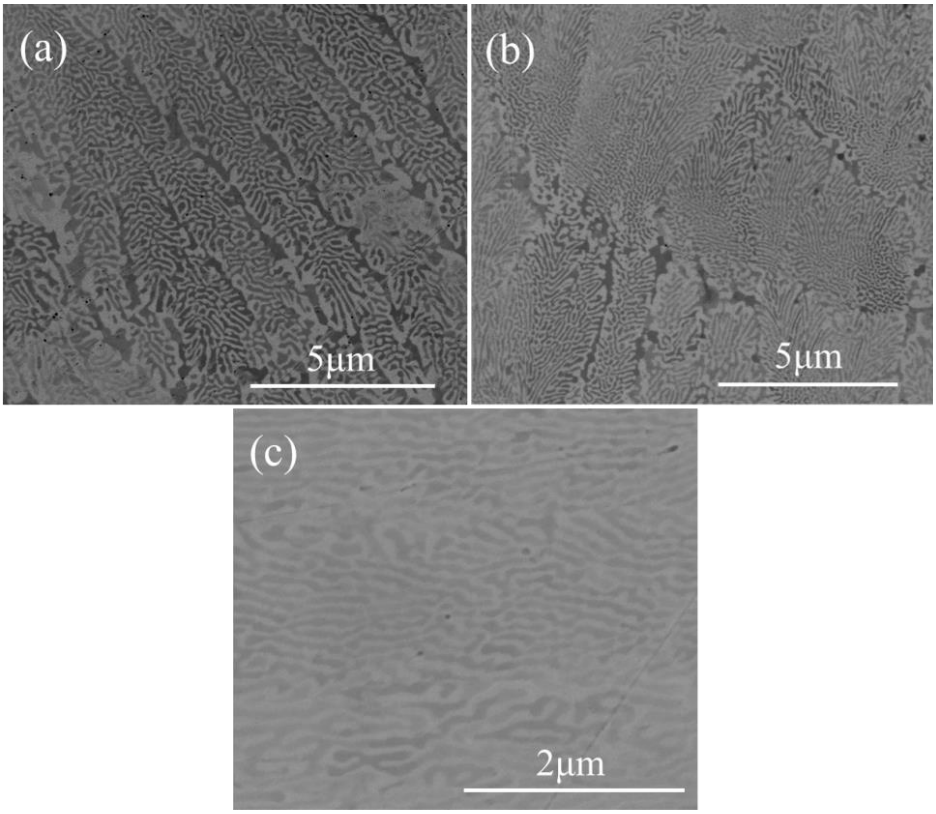

Fig5.3. SEM micrographs of as-cast samples with 2mm diameter:(a) $Cu_{90.5}Zr_{7.5}Ti_2$; (b) $Cu_{90}Zr_8Ti_2$ (c) $Cu_{92.5}Zr_{7.5}$.

Fig5.3 presents the backscattered SEM images from the centre of the 2mm-diameter $Cu_{90.5}Zr_{7.5}Ti_2$, $Cu_{90}Zr_8Ti_2$and $Cu_{92.5}Zr_{7.5}$ alloys. For the $Cu_{90.5}Zr_{7.5}Ti_2$alloy, two levels of structures were observed: primary Cu dendrites, 90-330nm in width and 1.5-2.3μm in length, and Cu solid solution in ultrafine cluster zone, 60-180nm in width and 0.12-2.16μm in length. The primary Cu dendrites were distributed uniformly and parallel with each other in the ultrafine clusters. The interdendritic spacing of the parallel primary Cu dendrites ranged between 1.5-1.8μm, which is the same width as the ultrafine cluster zones. Due to the fast cooling, the further growth of primary Cu solid solution dendrites was successfully suppressed. Fig5.3b gives the microstructure of $Cu_{90}Zr_8Ti_2$ alloy. The $Cu_{90}Zr_8Ti_2$ alloy exhibits similar microstructure with $Cu_{90.5}Zr_{7.5}Ti_2$ alloy: primary Cu solid solution dendrites and ultrafine clusters, but both the primary Cu dendrites and the features of ultrafine clusters are much finer than that in $Cu_{90.5}Zr_{7.5}Ti_2$ alloy. The distribution of primary Cu dendrites was apparently random in the 2D section taken (no parallel distribution). The primary Cu dendrites range over 0.59-2.5μm in length and 59-480nm in width, while the Cu solid solution in the ultrafine clusters ranges over 30-200nm in width and 0.05-0.96μm in length. Typical lamella eutectic structure was observed in the $Cu_{92.5}Zr_{7.5}$ alloy (shown in Fig5.3c), which is quite different with the ultrafine clusters in $Cu_{90.5}Zr_{7.5}Ti_2$ and $Cu_{90}Zr_8Ti_2$ alloys. The size of ultrafine Cu solid solution varied over 40-100nm in thickness and 0.14-1.61μm in length, while the thickness of their interspacing ranges was in the range 30-90nm. In comparison with the microstructure of the ingot $Cu_{92.5}Zr_{7.5}$ alloy (100nm to 300nm in thickens of Cu solid solution), as expected a high cooling rate produced much finer structure in the as-cast $Cu_{92.5}Zr_{7.5}$ alloy.

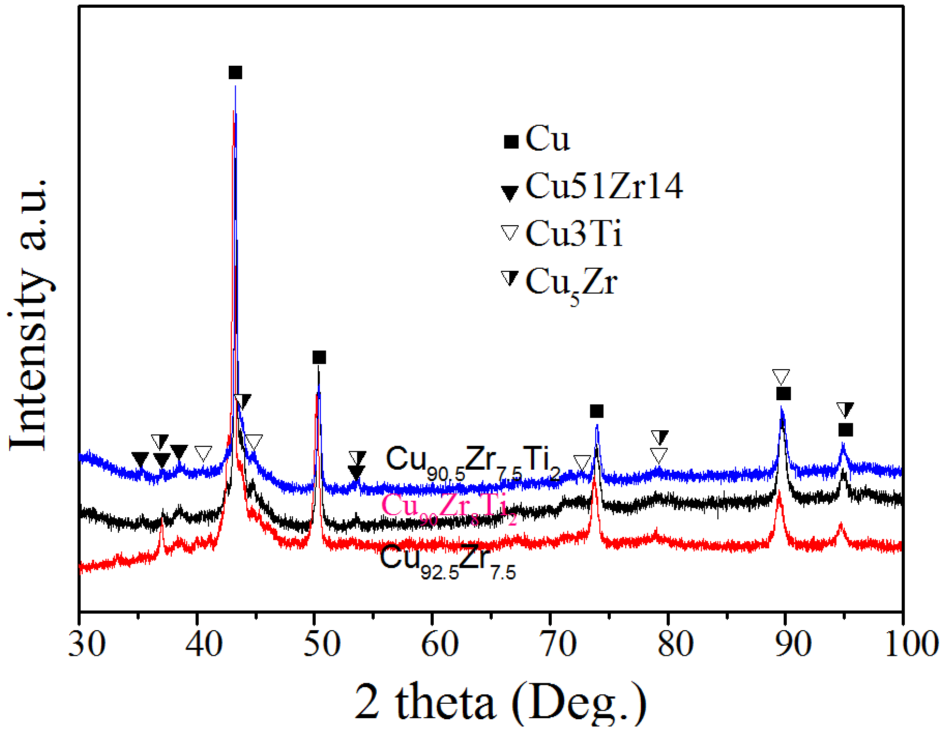

Fig5.4. XRD patterns of the as-cast$Cu_{90}Zr_8Ti_2$, $Cu_{90.5}Zr_{7.5}Ti_2$ and $Cu_{92.5}Zr_{7.5}$ alloys with a diameter of 2mm.

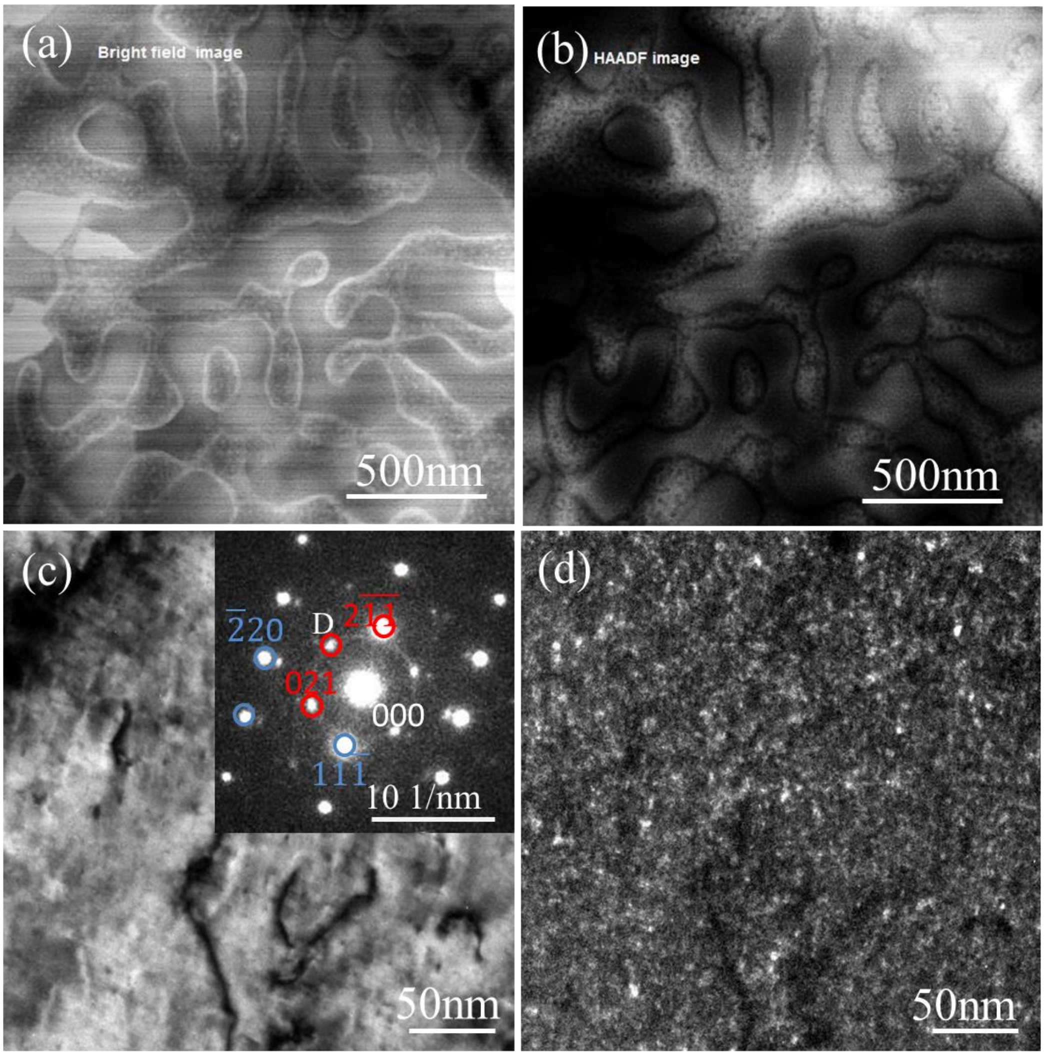

Fig5.5 TEM micrographs of $Cu_{90.5}Zr_{7.5}Ti_2$ alloy. Bright field scanning transmission electron microscopy (BF-STEM) image (a) shows the ultrafine microstructure and high-angle annular dark field scanning transmission electron microscopy (HAADF-STEM) (b) confirms the formation of numerous intragranular nanoprecipitates in Cu. Bright field TEM image (c) taken along Cu[112] zone axis and its corresponding dark field image (d) further confirms the present of nanoprecipitates. Inset of (c): selected diffraction pattern taken from the Cu dendrites identifies that the nanoprecipitates are Cu_3Ti.

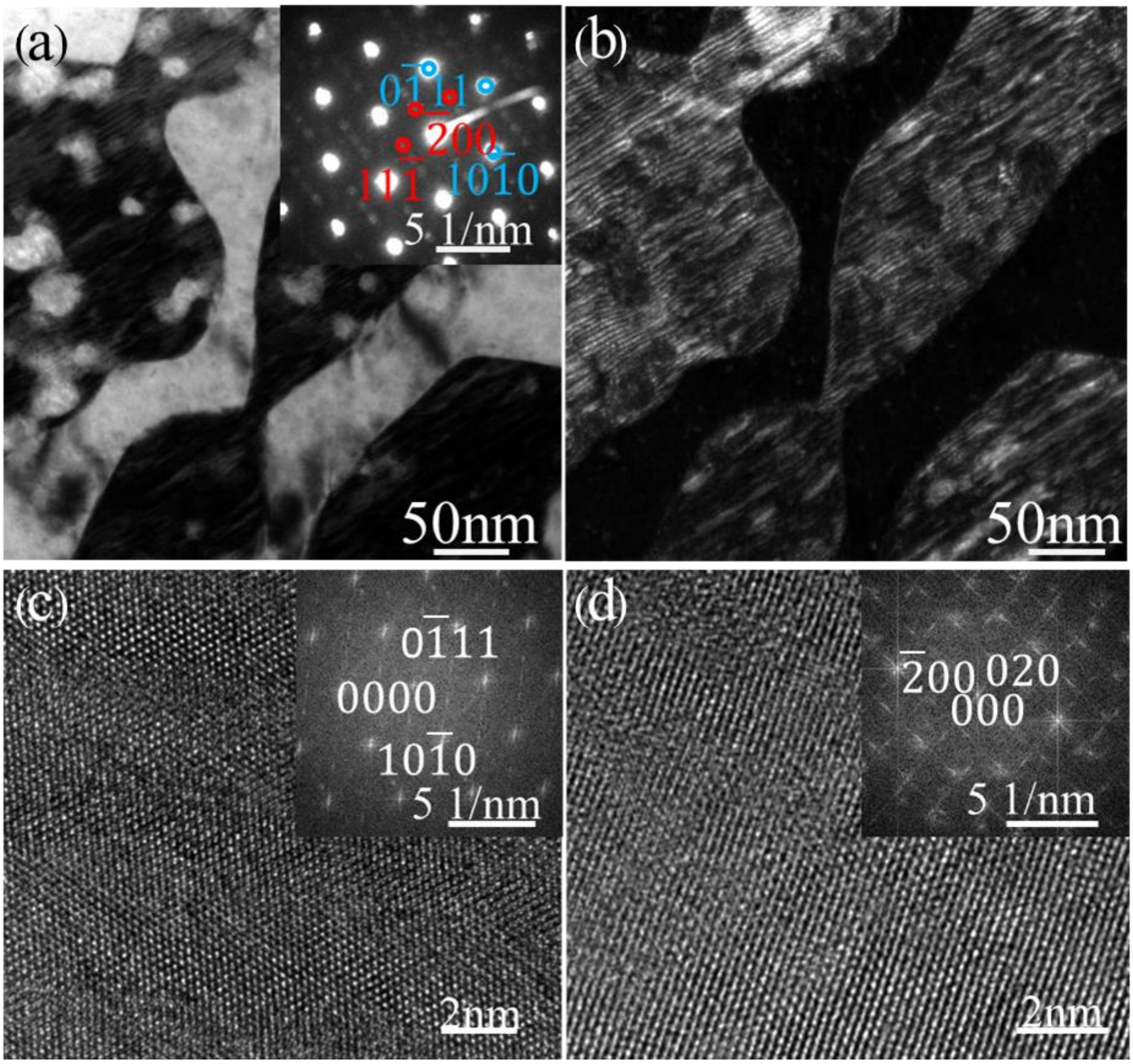

Fig5.6 Bright field TEM micrograph (a) of $Cu_{90.5}Zr_{7.5}Ti_2$ alloy and the selected area diffraction pattern taken from the dark $Cu_{51}Zr_{14}$ phase. Dark field TEM image (b) using the diffraction spot of $Cu_{51}Zr_{14}$ $(0\bar{1}11)$ shows the nanoscale lamella structure. (c) HRTEM image taken from the dark $Cu_{51}Zr_{14}$ phase. Inset: fast Fourier transformation (FFT) image showing the diffraction of $Cu_{51}Zr_{14}$ zone axis $[1\bar{2}13]$ of hexagonal crystalline system. (d) HRTEM image taken from the dark $Cu_{51}Zr_{14}$ phase. Inset: FFT image showing the diffraction of a zone axis [001] of f.c.c. crystal (Cu_5Zr).

Fig5.4 gives XRD patterns of the as-cast $Cu_{90.5}Zr_{7.5}Ti_2$, $Cu_{90}Zr_8Ti_2$and $Cu_{92.5}Zr_{7.5}$ alloys. As can be seen from the Fig5.4, Cu solid solution, Cu_5Zr and$Cu_{51}Zr_{14}$ phases were observed for all the three alloys. For $Cu_{90.5}Zr_{7.5}Ti_2$ and $Cu_{90}Zr_8Ti_2$ alloy, Cu_3Ti was also observed.

In order to further identify the microstructure, TEM was employed to investigate the $Cu_{90.5}Zr_{7.5}Ti_2$ alloy. The bright-field STEM image (Fig5.5a) shows the ultrafine Cu uniformly distributed in $Cu_{51}Zr_{14}$ matrix. The size (thickness) of both phases was in the range 40-190nm, corresponding well with the SEM observation. HAADF-STEM was applied to obtain high Z-contrast image to investigate the distribution of precipitates. As observed in Fig5.5b, numerous intragranular nanoprecipitates are dispersed in a Cu solid solution. Fig5.5c shows a bright field TEM image taken from the Cu solid solution and the inset in the top-right hand side displays its corresponding selected area diffraction pattern taken along [112] zone axis of Cu. Two sets of diffraction patterns were observed in the inset of Fig5.5c. The diffraction with relatively brighter spots (highlighted by blue circles) corresponds to the diffraction of the Cu [112] zone axis, while the extra weak diffraction spots (highlighted by red circles) matches well with the diffraction of Cu_3Ti $[\bar{1}\ 2\ \bar{4}]$ zone axis. The interplaner spacing of (021), (210) and $(2\bar{1}\bar{1})$ atomic planes and interplanner angle between (021) and $(2\bar{1}\bar{1})$ of Cu_3Ti are calculated as 0.196nm, 0.196nm, 0.222nm and 124.9° respectively, which corresponds to our measured values 0.194nm, 0.195nm 0.225nm and 124.2°. The interplanner angle between (021) and (210) of our measured value (67.5°) also equates well with the calculated value (67.2°). The dark-field image (Fig5.5d) taken from diffraction spot of (210) illustrates the uniform distribution of Cu_3Ti precipitates, equating well the HAADF-STEM image (Fig5.5b).

Fig5.6a shows the bright field image take along the zone axis $[1\bar{2}13]$ of the $Cu_{51}Zr_{14}$ phase, which displays a very sharp contrast attributed to diffraction contrast and Z contrast. The rel-

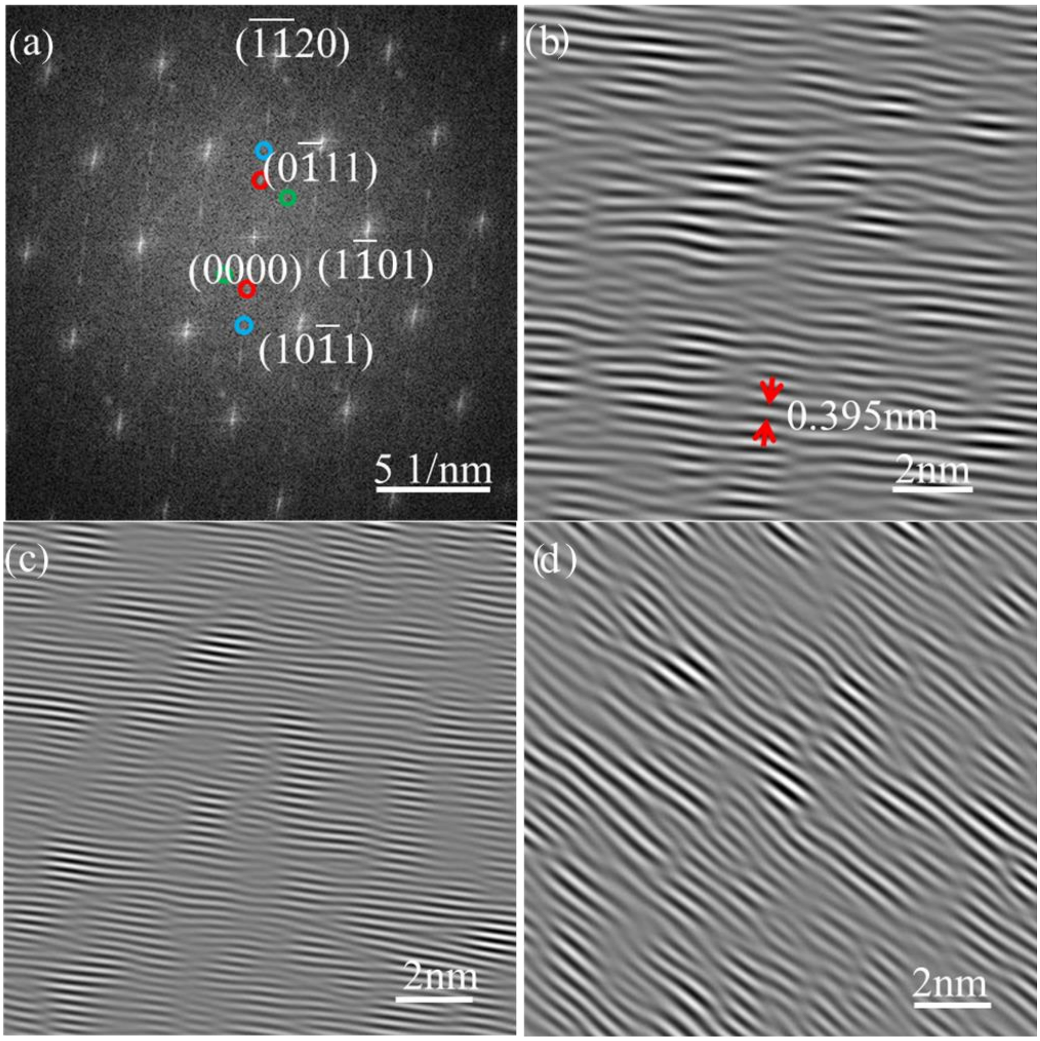

Fig5.7. (a) FFT image taken from HRTEM image shown in Fig4.6c; two sets of extra spots was observed in reciprocal vectors of $\overrightarrow{g_1}$= $[\overline{1}\overline{1}21]$ and $\overrightarrow{g_2}$ =$[0\overline{1}11]$. (b) IFFT image filtered using one pair of spots located at 1/3 of $\overrightarrow{g_1}$ (indicated by one pair of red circles in (a)). (c) IFFT image filtered using one pair of spots located at 1/2 of $\overrightarrow{g_1}$ (indicated by one pair of blue circles in (a)). (d) IFFT image filtered using one pair of spots located at 1/2 of $\overrightarrow{g_2}$ (indicated by one pair of green circles in (a)).

-atively brighter spots highlighted by blue circles in the inset of Fig5.6a are identified from the diffraction of $[1\overline{2}13]$ zone axis of $Cu_{51}Zr_{14}$ phase. There are three extra weak diffraction spots in the $Cu_{51}Zr_{14}$ diffraction pattern with a reciprocal vector ($\overrightarrow{g_1}$= $[\overline{1}\overline{1}21]$), which are located at

$[\frac{\bar{1}}{3}\frac{\bar{1}}{3}0\frac{1}{3}]$, $[\frac{\bar{1}}{2}\frac{\bar{1}}{2}0\frac{1}{2}]$ and $[\frac{\bar{2}}{3}\frac{\bar{2}}{3}0\frac{2}{3}]$ in reciprocal space. Further analysis shows that the extra diffraction spots located at 1/3 and 2/3 of the reciprocal vector $\overrightarrow{g_1}$ are from the diffraction of [011] zone axis of one f.c.c. phase, which corresponds to Cu_5Zr phase. The interplanar spacing of $(\bar{2}00)$, $(\bar{1}1\bar{1})$ and $(11\bar{1})$ atomic planes and the interplanar angle between $(\bar{2}00)$ and $(11\bar{1})$ of Cu_5Zr are calculated as 0.344nm, 0.397nm, 0.397nm and 125.26°, which matches well with our measured values 0.337, 0.391nm, 0.391nm and 124.90°. The interplanner angle between $(\bar{1}1\bar{1})$ and $(11\bar{1})$ of our measured value (70.40°) also corresponds well with the calculated value (70.50°). The extra spot located at 1/2 of could be attributed to formation of modulated variants in $Cu_{51}Zr_{14}$ phase and there is another set of extra weak diffraction spots located at a reciprocal vector ($\overrightarrow{g_2}$ = $[0\bar{1}11]$). Dark field TEM image (Fig5.6b) using the diffraction spot $(0\bar{1}11)$ of $Cu_{51}Zr_{14}$ presents the nanoscale lamella structure of $Cu_{51}Zr_{14}$. The black contrast between each layer of lamella structures conforms the present of Cu_5Zr in $Cu_{51}Zr_{14}$ phase. FFT image in the inset of Fig5.6d is identified from the diffraction of a zone axis [001] of f.c.c. crystal, which further confirms the formation of Cu_5Zr in $Cu_{51}Zr_{14}$ .Because the crystalline structures shown in the HRTEM images of Fig5.6c and d are too complicated to interpret, inverse fast Fourier transformation (IFFT) images filtered using specific pairs of diffraction spots is employed (Fig5.7). The observation of some bright contrast regions (12nm-35nm) in the dark $Cu_{51}Zr_{14}$ phase shown in bright-filed image of Fig5.6 (a) is attributed to the high energy ion milling damage, which will be analysed in Fig5.8.

The FFT image shown in Fig5.7a is taken directly from the HRTEM image shown in Fig5.6c. In order to further confirm that the extra diffraction spots located at 1/3 and 2/3 of the reciprocal vector $\overrightarrow{g_1}$ are from the diffraction of zone axis [011] of Cu_5Zr, one pair of diffraction spots located at 1/3 of $\overrightarrow{g_1}$ (indicated by red circles in Fig5.7a) were used to obtain

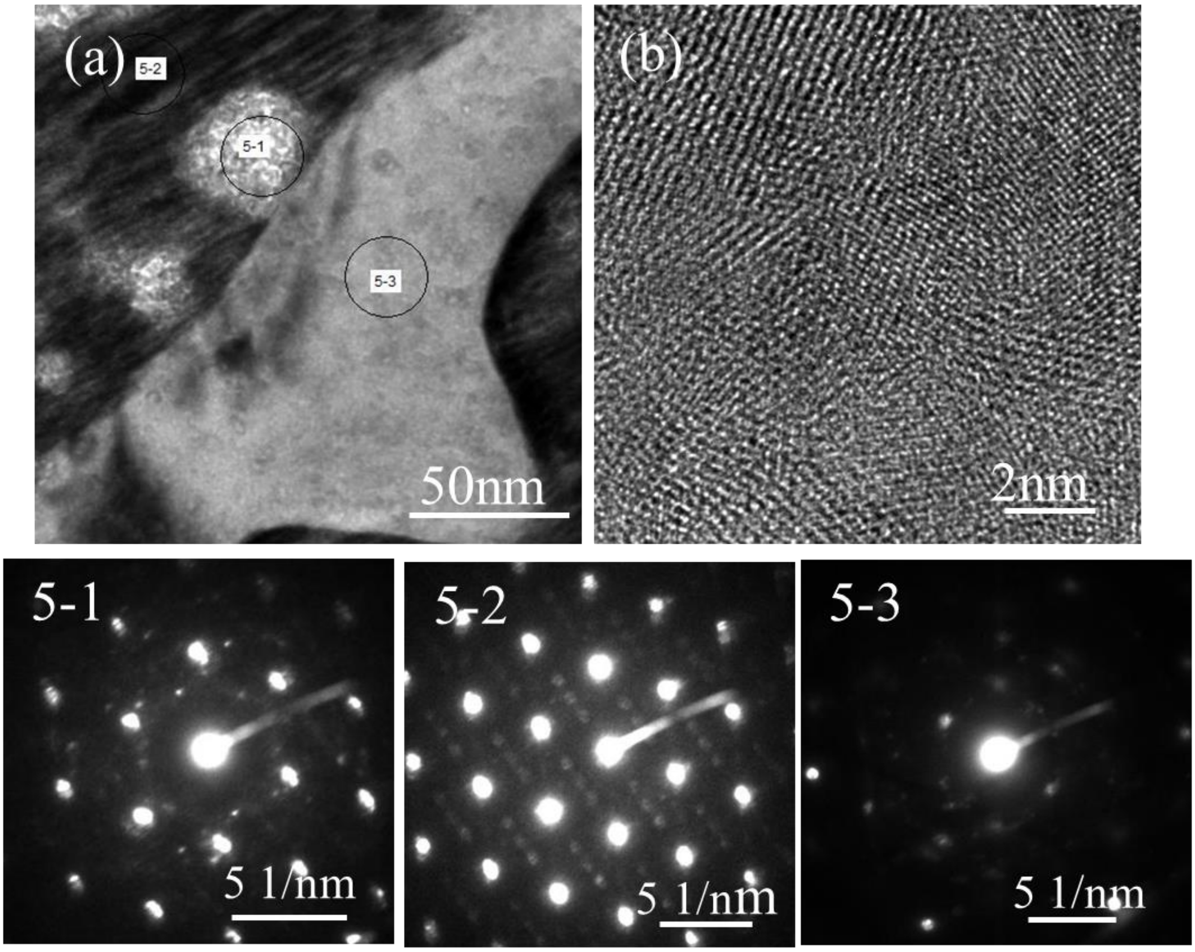

Fig5.8 TEM analysis of the ion milling damaged regions during preparation of the thin foil samples. (a) Bright-field image and the corresponding microbeam diffraction patterns taken from the circled area indicated as 5-1,5-2 and 5-3 in (a). (b) HRTEM image taken from area 5-1 shown in (a) presents the formation of nanocrystalline structure.

the IFFT image. Fig5.7b shows modulated atomic plane distribution of the selected pair of diffraction spots. As identified in Fig5.6a, the selected diffraction spots correspond to $(\bar{1}1\bar{1})$ atomic plane of Cu_5Zr. We also measured the interplanar spacing (0.395nm) from the IFFT image (Fig5.7b), which matches well with the calculated value (0.397nm). Fig5.7c and d show the IFFT images filtered by one pair of diffractions spots located at 1/2 of $\overrightarrow{g_1}$ (indicated by blue circles in Fig5.7a) and one pair of diffraction spots located at 1/2 of $\overrightarrow{g_2}$ (indicated by green circles in Fig5.7a), respectively. The fluctuation of the fringes in Fig5.7c and d indicates the modulation and lattice distortion displacement, which could be attributed to the formation of variants as observed in the martensitic transformation of Ni_2FeGa alloy [32]. The formation of these modulated structures could be attributed the eutectoid decomposition reaction: Cu_5Zr →f.c.c.Cu + $Cu_{51}Zr_{14}$ occurs between 802 and 955 K[33].

The bright contrast regions in the dark $Cu_{51}Zr_{14}$ phase in Fig5.8a share similar contrast with the Cu solid solution in Fig5.6a. In order to further investigate the crystalline structure, microbeam diffraction and HRTEM analysis were conducted. As shown in the diffraction pattern of the bright region marked as 5-1, the relatively brighter diffraction spots can be identified as the diffraction of $Cu_{51}Zr_{14}$ $[1\bar{2}13]$ zone axis. However, the periodical distribution of extra weak spots in the reciprocal vector ($\overrightarrow{g_1}$= $[\overline{11}21]$) were not observed, indicating the microstructure has been damaged by ion milling. The formation of the polycrystalline diffraction ring is attributed to the formation of nanocrytalline by ion-milling damage. The HRTEM image shown in Fig5.8b further confirms the formation of nanocrystalline in the 5-1 region. The diffraction pattern taken from the region marked as 5-2 shows the crystalline structure as observed in Fig5.6a, without any ion-milling damage. The diffraction pattern (5-3) was taken from the Cu solid solution. Because the diffraction pattern was not taken from any zone axis of Cu, we do not observe a proper set of diffraction pattern.

5.3.3 Mechanical properties

The engineering stress-strain curves of as-cast $Cu_{90.5}Zr_{7.5}Ti_2$, $Cu_{90}Zr_8Ti_2$ alloys and hot-extruded pure Cu are shown in Fig5.9. As shown in Fig5.9, in comparison with hot-extruded pure Cu, a significant improvement in mechanical properties has been achieved in the as-cast $Cu_{90.5}Zr_{7.5}Ti_2$ and $Cu_{90}Zr_8Ti_2$ alloys. The $Cu_{90}Zr_8Ti_2$ alloy exhibits a yield stress $R_{P0.2} \approx$ 886MPa, fracture strength, $\sigma_f = 1062$MPa and a total strain to failure, $\varepsilon_{tot} = 2.1\%$. For the $Cu_{90.5}Zr_{7.5}Ti_2$alloy, pronounced plastic deformation with a uniform strain $\varepsilon_{tot} = 5.16\%$ was observed. The yield stress reaches $R_{P0.2} \approx$ 787MPa, which is relatively lower than that in $Cu_{90}Zr_8Ti_2$alloy. The ultimate stress arrives at σ_f=1221MPa. Hot-extruded pure Cu yielded around $R_{P0.2} \approx$ 244MPa. After yielding, this alloy exhibited work hardening up to a tensile strength 322MPa at a strain of 0.7%, followed by ~16% softening plastic deformation. The pronounced work hardening behaviour after yielding observed in the as-cast nanostructured $Cu_{90.5}Zr_{7.5}Ti_2$ and $Cu_{90}Zr_8Ti_2$ alloy is abnormal in nanostructured alloys, as reported in Refs[11-13], the absence of dislocation multiplication is attributed to the poor work hardening ability of nanostructured alloys.

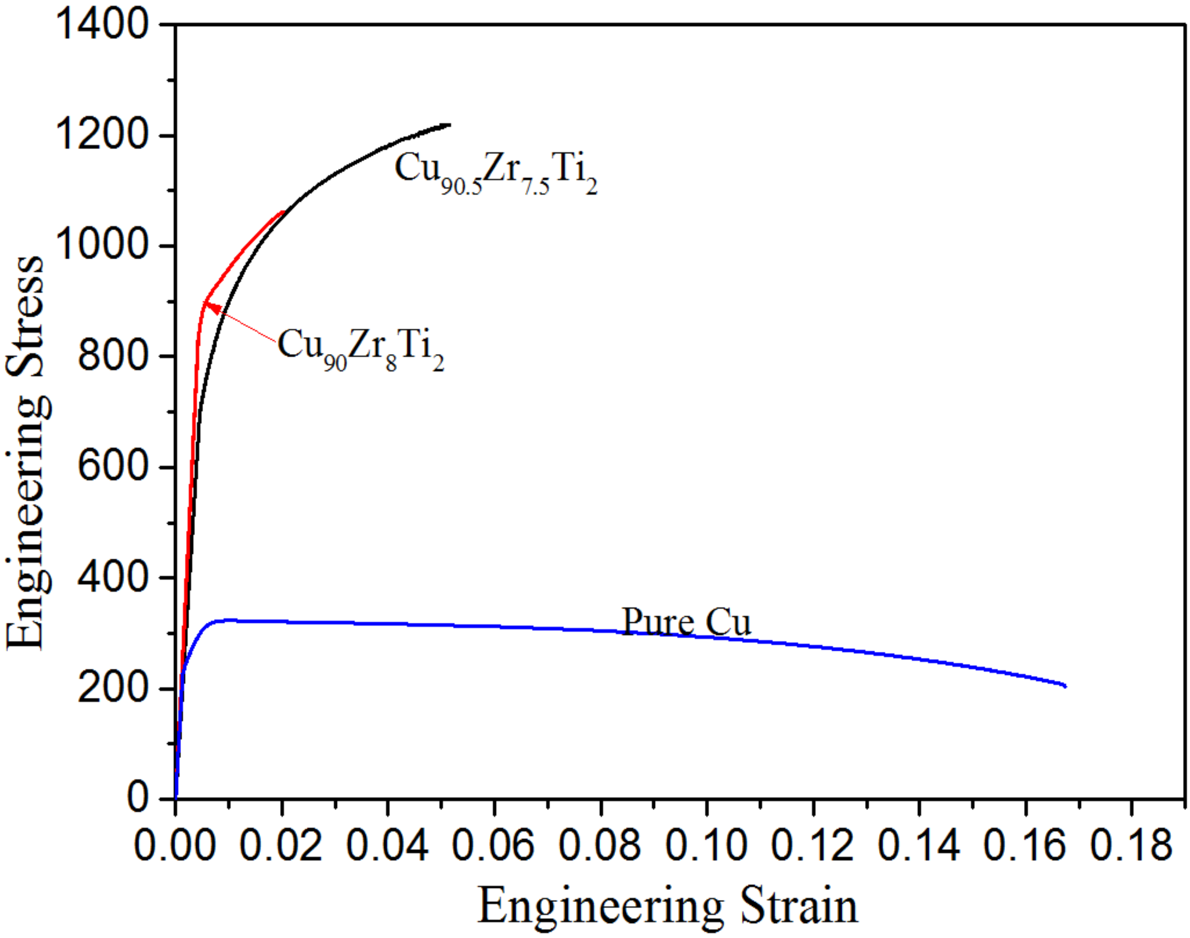

Fig5.9 Room-temperature tensile stress-strain curves for hot-extruded pure Cu, as-cast $Cu_{90.5}Zr_{7.5}Ti_2$ and $Cu_{90}Zr_8Ti_2$ alloys at a strain rate of$10^{-4}s^{-1}$.

In order to evaluate the mechanical property difference between the ultrafine softer Cu solid solution and the surrounded harder $Cu_{51}Zr_{14}$, nanoindentation was employed to study the mechanical properties of each phase in $Cu_{90.5}Zr_{7.5}$ Ti_2alloy. As shown in Table5.2, the average harnesses of the Cu solid solution and $Cu_{51}Zr_{14}$ composite was measured as 3.30±0.55GPa and 9.17±0.64GPa, respectively. Fig5.10 shows that the indents in Cu solid solution and$Cu_{51}Zr_{14}$, which exhibit a huge difference in indent size, directly confirming the huge difference in hardness between these two phases. Difference in the reduced modulus (Er) was also observed between Cu solid solution (137GPa) and surrounded $Cu_{51}Zr_{14}$ phase (161GPa) (shown in Table5.2).

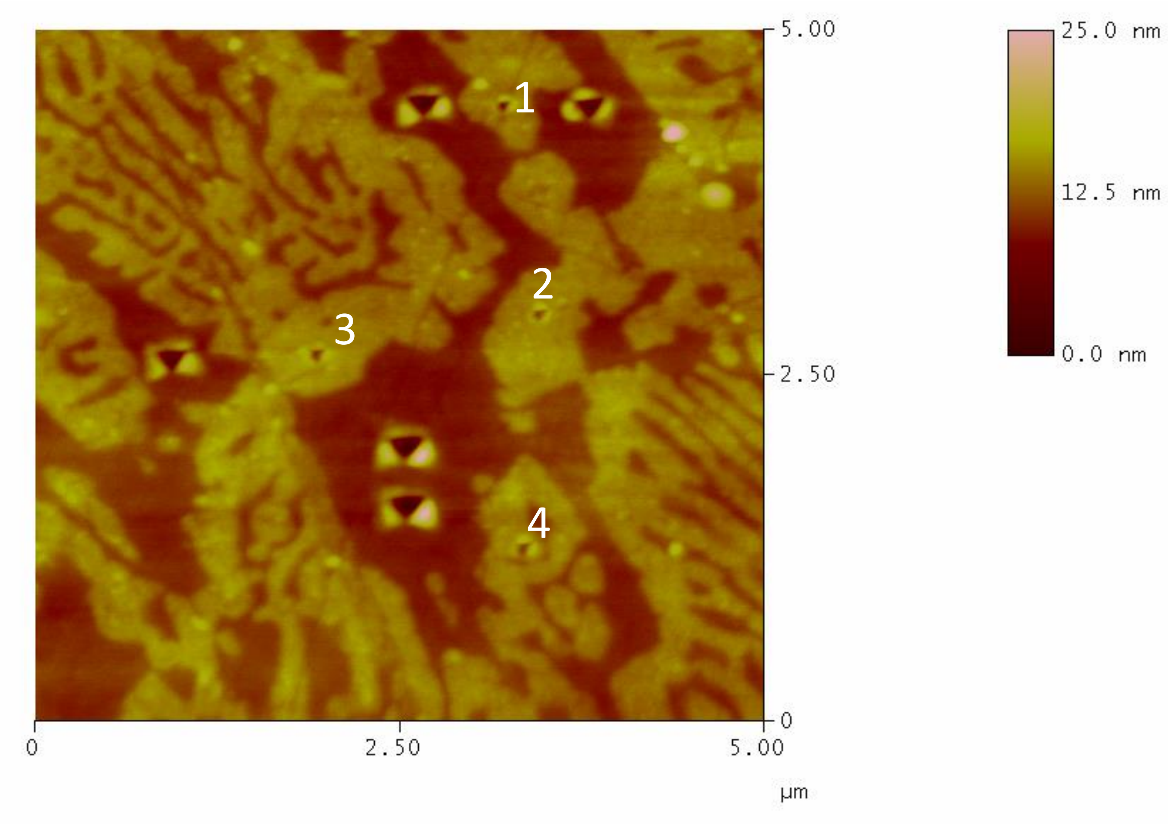

Fig5.10. Atomic force microscope (AFM) micrograph of $Cu_{90.5}$ $Zr_{7.5}$ Ti_2after nanoidentation tests. Nanoindentation results of $Cu_{90.5}$ $Zr_{7.5}$ Ti_2shows a huge difference in hardness between the dark phase (Cu) and bright phase (CuZr intermetallic).

Table 5.2 Nanoindentation results for Cu solid solution dendrites and $Cu_{51}Zr_{14}$ phases of the as-cast $Cu_{90.5}Zr_{7.5}Ti_2$ alloy.

	Er (GPa)	Hardness (GPa)
Dark Area (Cu)	137.07±9.43	3.30±0.55
Bright Area (intermetallic)	161.05±6.16	9.17±0.64

5.4 Discussion

5.4.1 Formation of diffusion controlled nanostructured CuZr alloy

NMs have obtained extensive interest attributed to the unique set of properties unachievable by coarse-grained polycrystalline materials [34]. However, the synthesis of these NMs into bulk parts is often very challenging, attributed in part to limitations in processing methods that are not easily scalable such as electrodeposition[19, 35] and HPT[36] or due to the current processing methods such as consolidation of nano-grained powders[34] and severe plastic deformation [37] that are either costly or introduce inherent flaws, such as porosity, impurities and internal stresses, making it difficult to mass-produce very strong bulk alloys[12].

Effective control of phase growth during material synthesis and processing is vital to achieve desired properties for materials [38-40]. In this work diffusion control was successfully introduced during the solidification to fabricate in-situ-cast NMs by appropriate choice of alloying elements and composition in CuZr alloys. The CuZr system has received extensive attention for metallic glass study largely because of the strong compositional dependence of its glass forming ability coupled with the alloy's ability to yield adequately large amorphous samples to facilitate experimental study [24, 41, 42]. Therefore, a large body of research has been conducted to explore the mechanism of enhanced glass forming ability in certain compositions of CuZr system. Mendelev et al. [24] conducted molecular dynamics simulations of diffusion in CuZr alloys in their equilibrium liquid and supercooled liquid states. Their simulations revealed that the atom mobility of both Cu and Zr exhibits strong compositional dependence and both elements exhibiting minimum diffusivities at ∼ 70 at.% Cu, which is very close to the best glass forming composition ($Cu_{64.5}Zr_{35.5}$)[41]. The current work used these simulation results to successfully design an in-situ-cast nanostructured CuZrTi alloy with ultrahigh strength and large uniform elongation. According to the phase diagram of CuZr[33, 43, 44], there is a dispute on the eutectic composition at the Cu-rich corner. Arias and Abriata[43] reported that the eutectic reaction occurs at $Cu_{91.4}Zr_{8.6}$ (at.%) (L↔Cu+Cu_9Zr_2 (Cu_5Zr), while, recently, Zhou and Napolitano[33] reported that the eutectic reaction occurs at $Cu_{92.8}Zr_{7.2}$ (at.%) (L↔Cu+Cu_5Zr). In this work, typical lamella eutectic structure is observed in the ingot and as-cast $Cu_{92.5}Zr_{7.5}$ alloys, while in the $Cu_{90.5}Zr_{7.5}Ti_2$ alloy (Fig5.1a and Fig5.3a) coarse Cu dendrites were uniformly distributed in the ultrafine structure. Therefore, it seems that the addition of Ti stabilizes the primary Cu dendrite solid solution, but there are no reports confirming that the addition of Ti in Cu alloys can stabilize f.c.c. Cu. According to the CuTi phase diagram [30, 31], the eutectic point in the Cu rich corner is around 20at.%Ti, so the alloys ($Cu_{90.5}Zr_{7.5}Ti_2$ and $Cu_{90}Zr_8Ti_2$) are substantially hypoeutectic in chemical composition in the CuTi phase diagram. Therefore, the primary Cu dendrites tend to solidify first from the melt with 2at.%Ti, while for the $Cu_{92.5}Zr_{7.5}$ alloy, a typical eutectic structure was observed as the composition is very close to the eutectic point of CuZr phase diagram. According to the phase diagrams of the CuZr system, the maximum solubility of Zr in Cu is 0.12 at. % at 979 ℃ [29]. Zirconium has negligible solubility in Cu even at the eutectic temperature, thus it is expected to partition preferentially to the remaining liquid during the initial stage of solidification, so that the remaining liquid becomes enriched in Zr. The mobility of both Cu and Zr atoms is significantly minimized with an increase of Zr content [38], which can substantially block further growth of the initially formed Cu nuclei as the growth of Cu requires large amount of Zr and Cu diffusion and enable a continuous nucleation in the remaining melt. In order to more clearly present the solidification procedure of this CuZrTi alloys, Fig5.11 displays the schematic diagrams of solidification procedure for both CuZrTi alloy in this work and the conventional alloy for comparison. In the conventional system shown in Fig5.11a, the nucleation only occurs at the early stage of solidification. The initially formed nuclei tend to grow fast, which consumes the supersaturated solute in the surrounding melt, leading to an increase in the temperature of the surrounding melt by releasing latent heat [38]. Subsequently, the remaining melt does not have chance to form new nuclei due to a lack of sufficient undercooling and supersaturation [38]. Thus, in the conventional alloy system (Fig5.11a), the total number of the nuclei is mostly limited to the number of the nuclei initially formed at the early stage of solidification. By contrast, with the effective diffusional growth restriction by the surrounding melt rich in Zr and the negligible solubility of Zr in Cu (requiring large amount of Zr atoms partitioning for the further growth of Cu), the surrounding melt can gain sufficient undercooling and supersaturation for a continuous nucleation of new nuclei. This is because the remaining melt is stabilized by Zr and Ti to further increase the extent of supercooling, as observed in CuZrTi bulk metallic glass system [45]. Thus, the total number of the nuclei formed in the CuZrTi system is substantially higher than that in the conventional system (shown in Fig5.11a), which results in a much finer microstructure. The microstructure observed in Fig5.3a can further confirm our explanation of the solidification procedure of the $Cu_{90.5}Zr_{7.5}Ti_2$alloy. Fig5.3a shows that there are two levels of structure in the as-cast $Cu_{90.5}Zr_{7.5}Ti_2$ alloy: the primary Cu dendrites solid solution and ultrafine Cu solid solution embedded in the ultrafine $Cu_{51}Zr_{14}$ matrix. As mentioned above, the primary Cu dendrites solidified first from the melt (Fig5.11b), leading to the remaining melt rich in Zr and Ti, which solidified into the ultrafine structure due to the continuous nucleation of Cu in stabilized supercooled liquid (Fig5.11b).

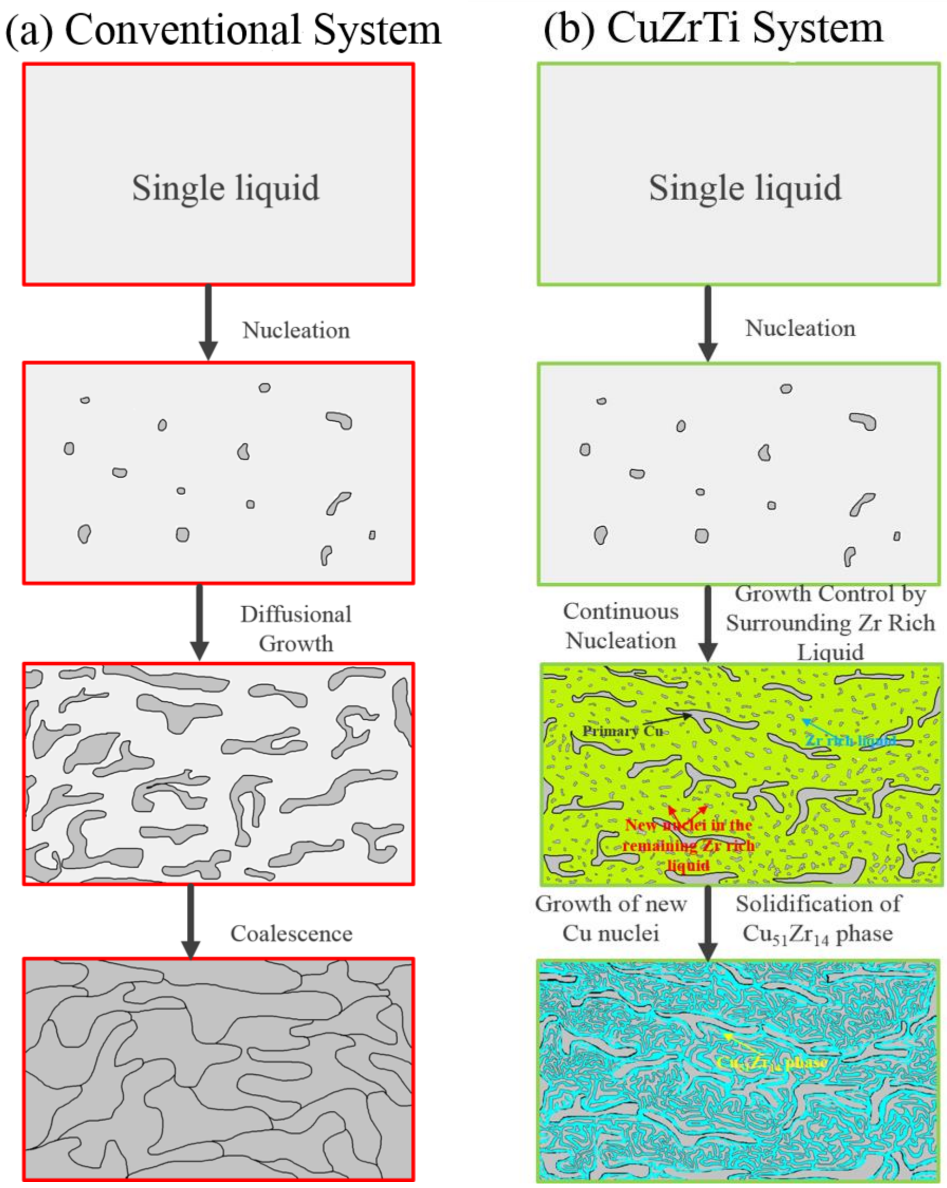

Fig5.11. Schematic of the structure evolution during solidification of a conventional alloy (a) and the current CuZrTi alloy (b). Above the melting point, both alloys exhibit a single liquid phase. Upon cooling, only very limited nuclei form for both alloys at the initial stage. After nucleation, the nuclei in conventional alloy grow rapidly while the growth of primary Cu in CuZrTi alloy is restricted by the surrounding remaining liquid which is stabilized by the high content of Zr. At this stage, numerous new Cu nuclei start formation in the remaining supercooled liquid. The final growth of these new Cu nuclei and the solidification of the

$Cu_{51}Zr_{14}$ results in the two levels microstructure: primary Cu dendrite phase and the ultrafine structure between them.

The ultrafine and fine structure observed in the ingot alloys shown in Fig5.1a and b can also corroborate the fact that the remaining melt rich in Zr can supress the growth of Cu dendrites by the reduced atom mobility of both Cu and Zr. As the cooling rate of ingot alloys is not as high as that of suction cast alloys during the solidification, before the formation of the ultrafine binary structure, fine binary structure was formed because both Zr and Cu atoms have a much longer time to diffuse. The solidification of $Cu_{92.5}Zr_{7.5}$ alloy should follow the typical eutectic solidification process [46]: the leading phase nucleates and these crystal nuclei act as a basis for nucleation of the second phase, and then branching and symbiotic growth takes place progressively to form eutectic structure. The EDS results shown in table 5.3 show that the average chemical composition of the phase with grey contrast (primary Cu) is around $Cu_{97.5\pm0.09}Zr_{0.6\pm0.1}Ti_{1.9\pm0.23}$ which further confirms the negligible solubility of Zr in Cu, while the average chemical composition of the bright matrix ($Cu_{51}Zr_{14}$) is $Cu_{75.3\pm1.7}Zr_{19.8\pm1.4}Ti_{5.0\pm0.4}$ which is close to the composition of $Cu_{70}Zr_{30}$ that exhibits minimum mobility of both Zr and Cu as observed in by Chen [38].

According to Refs [33, 47, 48], there remains considerable uncertainty with regard to the relative stability between the Cu_5Zr and $Cu_{51}Zr_{14}$ phases. Ghosh [49] reported that $Cu_{51}Zr_{14}$ phase is only metastable at 0 K, while the Cu_5Zr phase is stable. Zhou and Napolitano [33] conducted a series of experimental and modelling work on $Cu_{89.1}Zr_{10.9}$ alloy to study the relative stability of Cu_5Zr and $Cu_{51}Zr_{14}$ phases. XRD analysis showed that the as-cast alloys are comprised of Cu_5Zr, $Cu_{51}Zr_{14}$ and fcc-Cu phases. They found that after a heat treatment of 955 K for 114 hours, followed by a water quench, the microstructural constituents were identified as Cu_5Zr and f.c.c.-Cu (without $Cu_{51}Zr_{14}$), which is consistent with the results of

Glimois et al.[50] who observed Cu_9Zr_2 (Cu_5Zr) in $Cu_{83.1}Zr_{16.9}$ alloy after treated at 1223 K for 500h. However, after heat treatment at 802 K for 138 h, followed by a water quench, the presence of the $Cu_{51}Zr_{14}$ phase except the Cu_5Zr and f.c.c.-Cu was observed in $Cu_{89.1}Zr_{10.9}$ alloy. Therefore, the eutectoid decomposition reaction: $Cu_5Zr \rightarrow$f.c.c.Cu + $Cu_{51}Zr_{14}$ occurs between 802 and 955 K. In the current work, the Cu_5Zr phase was observed in addition to the more stable $Cu_{51}Zr_{14}$ and f.c.c.Cu phases, Fig5.4. The observation of Cu_5Zr in the as-cast rod could be attributed the high cooling rate and low-temperature short-time remelting before casting, which suggests that the eutectoid decomposition reaction was not complete. As mentioned above, the ingots of $Cu_{90.5}Zr_{7.5}$ Ti_2 and $Cu_{90}Zr_8$ Ti_2 alloys were composed of Cu andCu_5Zr , which could be attributed the high-temperature long-time melting (to enhance material homogeneity) that makes the formation of relatively stable Cu_5Zr phase at high temperature. The Cu_5Zr phase was retained to room temperature due to high cooling rate of water-cooled crucible, like the quenched sample in Ref [33].

Table 5.3 EDS results for the phases in the as-cast of $Cu_{90.5}Zr_{7.5}$ Ti_2alloy.

Phase	Cu(at%)	Zr(at%)	Ti(at%)
Grey (Cu)	97.5±0.1	0.6±0.1	1.9±0.3
Bright (Cu51Zr14)	75.3±1.7	19.8±1.4	5.0±0.4

5.4.2 Deformation mechanism of nanostructured CuZrTi alloy

In comparison with ultrafine/nanostructured materials, coarse-grained materials have enough space for dislocations slip and multiplication, leading to materials' plastic deformation [11]. Therefore, the mechanical properties such as yield strength and work hardening behaviour of coarse-grained materials are controlled by dislocation slip. However, when the grain sizes reduces into the nanometre regime, conventional deformation mechanisms cease to operate [11]; both the nucleation and motion of dislocations are effectively suppressed by nanometre crystallites [51]. Therefore, NMs usually exhibit ultra-high strength with a very limited tensile ductility (uniform elongation within few percent) and almost no work-hardening before catastrophic failure [4, 11, 14, 36, 52]. This case is especially applicable in single-phase NMs with almost monodispersed grain size [6], because strain hardening tends to be absent owing to the inability to accumulate dislocations in these tiny identical grains [51]. In comparison with elongation to failure[10], uniform elongation can more accurately present the real deformability of NMs because the large post-necking strain often imparts a false impression of high ductility in NMs as most of them have a very short gauge length (small sample size). The

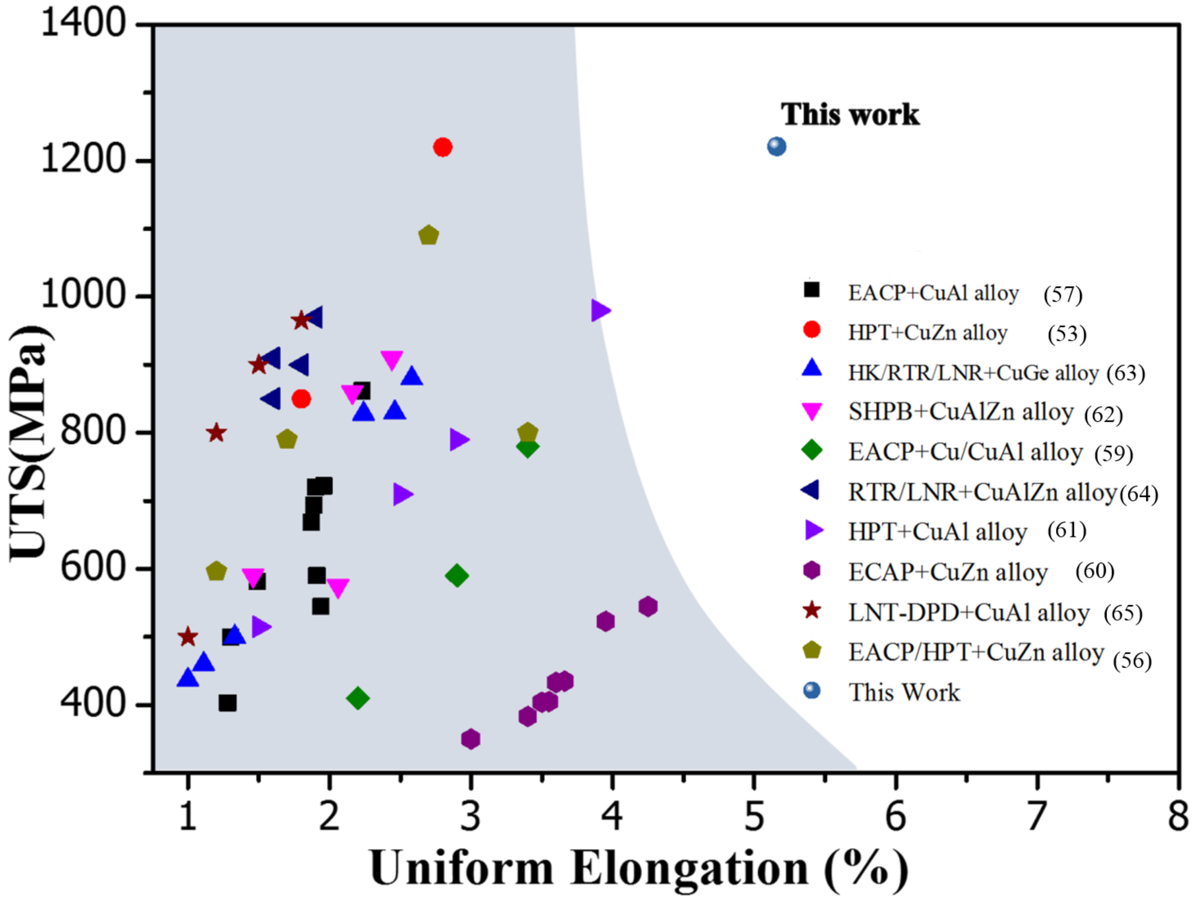

Fig5.12. Ultimate tensile strength versus uniform elongation of $Cu_{90.5}Zr_{7.5}$ Ti_2 alloy in comparison with ultrafine and nanostructured Cu and Cu alloys available in literature. In comparison with materials from literature (the shaded region), $Cu_{90.5}Zr_{7.5}$ Ti_2 alloy exhibits ultrahigh strength and uniform elongation simultaneously.

high strain hardening rate is essential for achieving large uniform elongation without pronounced strain localization such as necking [52]. Some strategies have been proposed to improve the tensile ductility of bulk ultrafine materials or NMs, including bimodal microstructure [51], nanoscale growth twins [19, 53] and multiphase alloys [54, 55].

It is reported that when a bimodal or multimodel structure was created on the nano/micro-scale, a large gain in work hardening and uniform strain was achieved, with only a small loss of strength [6, 9]. In these bimodal or multimodal alloys, the larger (softer) grains accommodate strains preferentially [4, 6, 9, 51]. With an increase of uniform strain (up to 30% in pure Cu), these larger grains had accumulated large numbers of twin boundaries, dislocations and subgrain boundaries such that the microstructure was refined to a level similar to the nanocrystalline/ultrafine grained matrix[9]. As identified by the nanoidentation results shown in Fig5.10 and table5.2, the hardness of $\mathrm{Cu_{51}Zr_{14}}$ matrix is around 9.17±0.64GPa, which is roughly three times harder than that of Cu solid solution phase (3.30±0.55GPa). Similar to the deformation mechanism of bimodal or multimodal structure, the deformation of softer grains (Cu solid solution) is used to achieve a much higher strain hardening rate than that usually observed in coarse grained alloys, owing to an excessive large number of geometrically necessary dislocation that are forced to be present to accommodate the large strain gradient[4, 9]. Fig5.12 summarizes the ultimate tensile strength versus uniform elongation available from the literature for ultrafine or nanostructured Cu and Cu alloys produced using processing techniques specifically to generate fine structures, including ECAP[56-60], HPT[53, 56, 61], rolling at room temperature (RTR)[62-64], rolling at liquid nitrogen temperature (LNR)[58, 63, 64], Split Hopkinson Pressure Bar impact (HK)[62, 63], dynamic plastic deformation at cryogenic temperature (DPD)[65] as well as our present tensile results of $\mathrm{Cu_{90.5}Zr_{7.5}\,Ti_2}$alloy. As shown in Fig5.12, the majority of the data from the literature is located at the bottom left corner and most of the materials exhibit a uniform elongation within 2%. Although some of the materials listed in Fig5.12 display a uniform elongation above 2% due to the occurrence of twinning in the materials [56, 58, 60, 61], their uniform elongations are still less than 4.5%. In Fig5.12 only the mechanical properties are listed of ultrafine and nanostructured Cu and Cu alloys processed by severe plastic deformation (SPD) because SPD processed materials are free of voids and possible to conduct tensile tests due to their relatively large sample size [51]. However, the large dislocation density in the grain interior and at grain boundaries after SPD tends to hinder dislocation gliding and multiplication during plastic deformation [51]. Although subsequent heat treatments can relieve these numerous defects to some extent, after heat treatment dislocations tends to accumulate around grain boundaries [51]. Zhao et al. observed that[58], after tensile testing, the dislocation density of ECAP-pressed Cu reduced from 4.3×10^{14} to $3.0\times 10^{14}\ \mathrm{m}^{-2}$, indicating that the poor dislocation accumulation capacity of SPD processed materials is responsible for the early necking (negligible working hardening). However, the as-cast $\mathrm{Cu_{90.5}Zr_{7.5}Ti_2}$ alloy exhibits a better combination of strength and uniform elongation. This indicates that the specific structure of the alloys developed in this work, namely, the uniform distribution ultrafine softer Cu with numerous intragranular nanoprecipitates in the nanoscale harder $\mathrm{Cu_{51}Zr_{14}}$ matrix embedded with f.c.c. $\mathrm{Cu_5Zr}$, provides a new way to strengthen NMs with ultrahigh strength and large uniform elongation. Fig5.13 displays the fracture morphologies of $\mathrm{Cu_{90.5}Zr_{7.5}Ti_2}$ alloys. The low magnification image shown in Fig5.13a exhibits a rough fracture surface, and the corresponding high magnification image shown in Fig5.13b clearly shows ductile fracture as the dimples extend across the whole fracture surface. The dimple size in the circled area varies over 80-230nm, which equates well with the size of Cu solid solution size (60-180nm) in the ultrafine clusters. Although $\mathrm{Cu_{51}Zr_{14}}$ is supposed to be a brittle phase, no brittle fracture characteristics were seen in the fracture surface, so the nanosized $\mathrm{Cu_{51}Zr_{14}}$ embedded with f.c.c.$\mathrm{Cu_5Zr}$ appears to have undergone ductile fracture mechanism. As observed in metallic glasses [66, 67], when sample size is reduced to a critical value (30–100 nm for Zr-based metallic glass), the brittle metallic glass tends to deform via homogenous flow instead of localized shear banding. The relative large dimples around the circled area range from 100 to 750nm, which matches well with the size of the primary Cu solid solution (90-330nm). The observation of the fine dimples distributed around these relatively large dimples (indicated by green arrows in Fig5.13b) could be attributed to the accumulation of large amounts of dislocations and subgrain boundaries during plastic deformation, which refine the large grains to a similar level of the fine grains area [9].

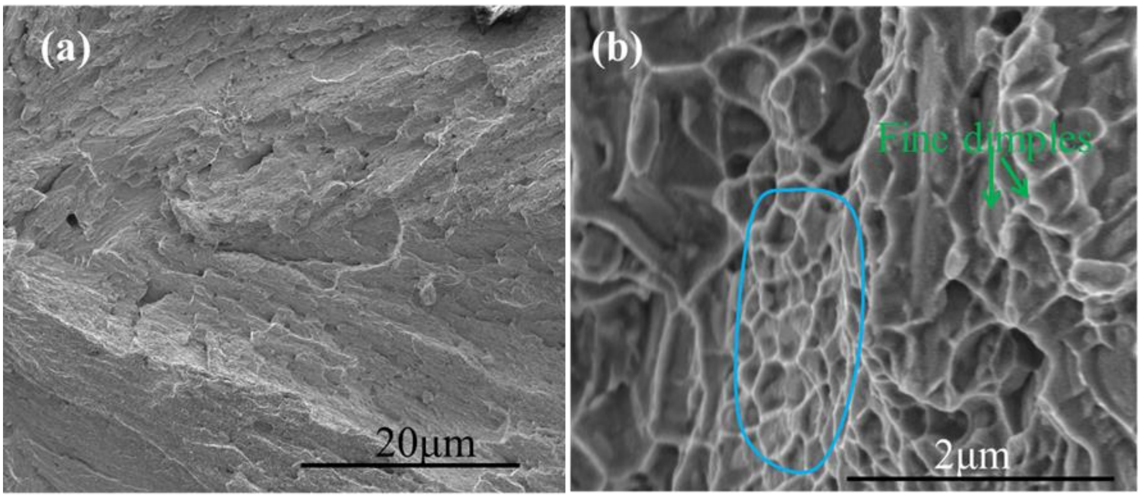

Fig5.13 Fracture morphologies of as-cast $Cu_{90.5}Zr_{7.5}Ti_2$alloy: (a) low magnification and (b) high magnification images.

In order to further investigate the deformation behaviour of $Cu_{90.5}Zr_{7.5}Ti_2$alloy, a thin foil sample taken from the fracture surface of $Cu_{90.5}Zr_{7.5}Ti_2$alloy was investigated by TEM. Fig5.14a presents the microstructure of interface between Cu and after tensile tests. As shown in Fig5.14a and b, numerous waved deformation bands with a width of 2.1nm were observed in the softer Cu, indicating severe plastic deformation occurred before final failure. In order to further characterize the deformed microstructure, STEM was performed and the bright field STEM micrograph and its corresponding HAADF-STEM are shown in Fig5.14c and d. In the bright field STEM micrograph (Fig5.14c), a large number of dislocations were observed in the softer copper after tensile testing. In Fig5.14d, these dislocations were absent in the HAADF-

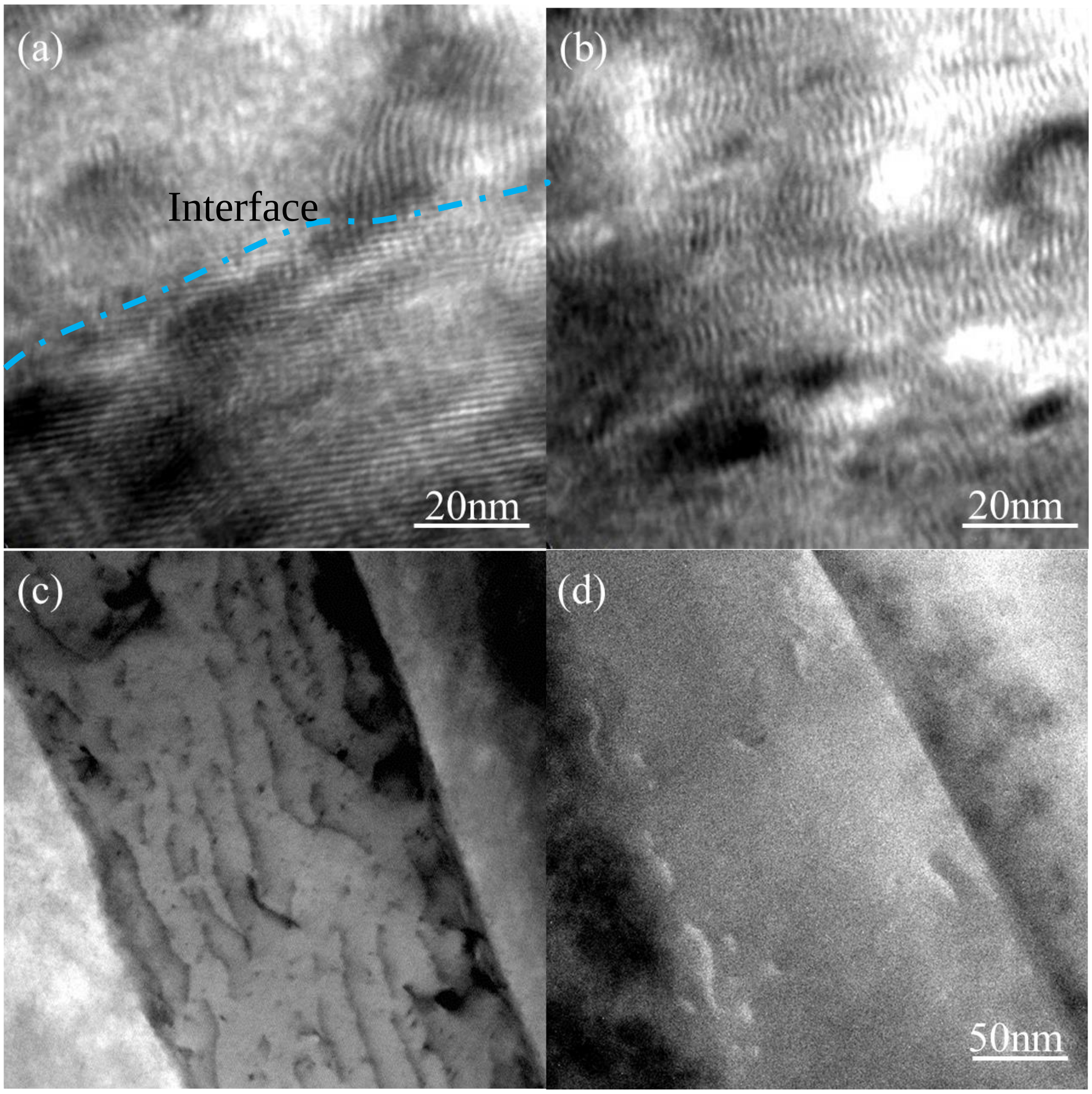

Fig5.14 TEM micrographs taken from the fracture surface of $Cu_{90.5}$ $Zr_{7.5}$ Ti_2alloy after tensile test. (a) Bright field TEM micrograph taken from the interface between Cu and $Cu_{51}Zr_{14}$ after tensile test. (b) Bright field TEM micrograph taken from softer Cu dendrites exhibits the formation of numerous deformation bands after tensile tests. (c) Bright field STEM presents the formation of a large numbers of dislocations in the softer copper after tension and the interaction between dislocations and intragranular nanoprecipitates. (d) The corresponding HAADF-STEM of (c).

STEM micrograph, which further confirms the formation of dislocations after tensile tests (the contrast of dislocation observed in Fig5.14c is from crystal defects). In Figure5.14c, the interaction between intragranular nanoprecipitates and dislocations is also observed in Cu, which hinders dislocation slip and promotes dislocation multiplication, thereby increasing working hardening rate. Thus the deformation procedures in tension of the CuZrTi alloy can be summarized as follows: (i) in the initial stage of plastic deformation, the relatively softer (larger) primary Cu dendrites are believed to yield first, leading to large amount of dislocation accumulation in these dendrites due to the uniform distribution of numerous intragranular nanoprecipitates (Fig5.14a); (ii) with further increase of loading, the ultrafine Cu solid solution in the ultrafine clusters starts yielding and dislocation multiplication commences in this ultrafine Cu and meanwhile, the formation of deformation bands are supposed to start due the severe plastic deformation in the primary Cu dendrites as observed in Fig5.14a and b, both of which contributes the work hardening and uniform plastic deformation; (iii) finally, the harder $Cu_{51}Zr_{14}$ matrix commences plastic deformation and upon further loading, and then cracks initiate from the interface, leading to final failure. Moreover, the formation of geometrically dislocations[4, 9] required by the inhomogeneous microstructure such as large grain size difference or two phases with huge difference in hardness could also contribute to the exceptionally high work hardening rate.

5.5 Conclusions

In the current work, a series of in-situ-cast nanostructured CuZrTi alloys were successfully designed by appropriate choice of alloying elements and compositions. XRD and TEM analysis shows that the alloys consist of softer Cu solid solution with numerous uniformly distributed intragranular Cu_3Ti nanoprecipitates and harder nano-scale $Cu_{51}Zr_{14}$ matrix embedded with retained Cu_5Zr . The $Cu_{90.5}Zr_{7.5}Ti_2$ alloy exhibited a yield strength of 787MPa, a fracture strength of 1221MPa and room temperature uniform tensile elongation of 5.16%, exhibiting simultaneous ultrahigh strength and large uniform elongation. The specific structure of these alloys, the uniform distribution ultrafine softer Cu phase with numerous intragranular nanoprecipitates in the nanoscale harder $\mathrm{Cu_{51}Zr_{14}}$ matrix embedded with $\mathrm{Cu_5Zr}$, is responsible for the large uniform elongation accompanied with ultrahigh strength. During tensile tests, the relatively softer (larger) primary Cu dendrites with numerous intragranular nanoprecipitates are believed to yield first, leading to large amount of dislocation accumulation due to their relatively large grain size and the uniform distribution of numerous intragranular nanoprecipitates. With further increase in loading, the ultrafine Cu solid solution in the ultrafine clusters starts yielding and dislocation multiplication commences in this ultrafine Cu, and meanwhile, the formation deformation bands is supposed to start in the primary Cu dendrites due their severe plastic deformation, both of which further contribute to the work hardening and uniform plastic deformation. Finally, the hard $\mathrm{Cu_{51}Zr_{14}}$ matrix commences plastic deformation and upon further loading, cracks start formation from the interface, leading to the final failure.

This work has several implications for the design of new ultrafine/nanostructured materials and their practical applications. First, the NMs in this work are produced by directly casting from liquid, so this approach are simple, cost-effective and can produce defect free materials, in comparison with the ultrafine/nanostructured materials produced by consolidation of nano-grained powders, or by severe plastic deformation. Second, the high work hardening rate coupled with large uniform elongation and ultrahigh strength of the $\mathrm{Cu_{90.5}Zr_{7.5}Ti_2}$ alloy is very exciting, which is attributed to its specific structure. Moreover, our proposed diffusion control composition design strategy is also insightful for the development new ultrafine/nanostructured alloys.

5.6 References

[1] M.A. Meyers, A. Mishra, D.J. Benson, Mechanical properties of nanocrystalline materials,Prog. Mater. Sci., 51 (2006) 427-556.

[2] H. Gleiter, Nanocrystalline materials, Prog. Mater. Sci., 33 (1989) 223-315.

[3] M. Dao, L. Lu, R.J. Asaro, J.T.M. De Hosson, E. Ma, Toward a quantitative understanding of mechanical behavior of nanocrystalline metals,Acta Mater., 55 (2007) 4041-4065.

[4] C.C. Koch, Optimization of strength and ductility in nanocrystalline and ultrafine grained metals, Scripta Mater., 49 (2003) 657-662.

[5] X. Huang, N. Hansen, N. Tsuji, Hardening by Annealing and Softening by Deformation in Nanostructured Metals, Science, 312 (2006) 249-251.

[6] E. Ma, Eight routes to improve the tensile ductility of bulk nanostructured metals and alloys, J.Mater., 58 (2006) 49-53.

[7] R.Z. Valiev, T.G. Langdon, Principles of equal-channel angular pressing as a processing tool for grain refinement, Prog. Mater. Sci., 51 (2006) 881-981.

[8] Y.T. Zhu, X. Liao, Nanostructured metals: Retaining ductility, Nat. Mater., 3 (2004) 351-352.

[9] Y. Wang, M. Chen, F. Zhou, E. Ma, High tensile ductility in a nanostructured metal, Nature, 419 (2002) 912-915.

[10] Y.H. Zhao, X.Z. Liao, S. Cheng, E. Ma, Y.T. Zhu, Simultaneously Increasing the Ductility and Strength of Nanostructured Alloys, Adv. Mater., 18 (2006) 2280-2283.

[11] X. Li, Y. Wei, L. Lu, K. Lu, H. Gao, Dislocation nucleation governed softening and maximum strength in nano-twinned metals, Nature, 464 (2010) 877-880.

[12] E. Ma, Nanocrystalline materials: Controlling plastic instability, Nat. Mater., 2 (2003) 7-8.

[13] E. Ma, T.D. Shen, X.L. Wu, Nanostructured metals: Less is more, Nat. Mater., 5 (2006) 515-516.

[14] Y. Zhao, T. Topping, J.F. Bingert, J.J. Thornton, A.M. Dangelewicz, Y. Li, W. Liu, Y. Zhu, Y. Zhou, E.J. Lavernia, High Tensile Ductility and Strength in Bulk Nanostructured Nickel, Adv. Mater., 20 (2008) 3028-3033.

[15] Y. Kimura, T. Inoue, F. Yin, K. Tsuzaki, Inverse Temperature Dependence of Toughness in an Ultrafine Grain-Structure Steel,Science, 320 (2008) 1057-1060.

[16] Z. Horita, K. Ohashi, T. Fujita, K. Kaneko, T.G. Langdon, Achieving High Strength and High Ductility in Precipitation-Hardened Alloys, Adv. Mater., 17 (2005) 1599-1602.

[17] Y. Huang, J.D. Robson, P.B. Prangnell, The formation of nanograin structures and accelerated room-temperature theta precipitation in a severely deformed Al–4wt.% Cu alloy Acta Mater., 58 (2010) 1643-1657.

[18] G. Liu, G.J. Zhang, F. Jiang, X.D. Ding, Y.J. Sun, J. Sun, E. Ma, Nanostructured high-strength molybdenum alloys with unprecedented tensile ductility, Nat. Mater., 12 (2013) 344-350.

[19] L. Lu, X. Chen, X. Huang, K. Lu, Revealing the Maximum Strength in Nanotwinned Copper, Science, 323 (2009) 607-610.

[20] L. Jiang, J.K. Li, P.M. Cheng, G. Liu, R.H. Wang, B.A. Chen, J.Y. Zhang, J. Sun, M.X. Yang, G. Yang, Microalloying Ultrafine Grained Al Alloys with Enhanced Ductility,Sci. Rep., 4 (2014)3605-6.

[21] L. Lu, Y. Shen, X. Chen, L. Qian, K. Lu, Ultrahigh Strength and High Electrical Conductivity in Copper, Science, 304 (2004) 422-426.

[22] K. Lu, L. Lu, S. Suresh, Strengthening Materials by Engineering Coherent Internal Boundaries at the Nanoscale, Science, 324 (2009) 349-352.

[23] H. Kou, J. Lu, Y. Li, High-Strength and High-Ductility Nanostructured and Amorphous Metallic Materials, Adv. Mater., 26 (2014) 5518-5524.

[24] M.I. Mendelev, M.J. Kramer, R.T. Ott, D.J. Sordelet, Molecular dynamics simulation of diffusion in supercooled Cu–Zr alloys Phil.Mag., 89 (2009) 109-126.

[25] Y.Q. Cheng, H.W. Sheng, E. Ma, Relationship between structure, dynamics, and mechanical properties in metallic glass-forming alloys Phys.Rev.B, 78 (2008) 014207-014213.

[26] Y.Q. Cheng, E. Ma, H.W. Sheng, Atomic Level Structure in Multicomponent Bulk Metallic Glass, Phys. Rev. Lett., 102 (2009) 245501-245504.

[27] S.G. Hao, C.Z. Wang, M.Z. Li, R.E. Napolitano, K.M. Ho, Dynamic arrest and glass formation induced by self-aggregation of icosahedral clusters in Zr1-xCux alloys, Phys.Rev.B, 84 (2011) 064203-064206.

[28] N. Wang, C. Li, Z. Du, F. Wang, W. Zhang, The thermodynamic re-assessment of the Cu–Zr system,Calphad, 30 (2006) 461-469.

[29] H. Okamoto, Cu-Zr (Copper-Zirconium), J. Phase Equilib. Diff., 33 (2012) 417-418.

[30] J.L. Murray, The Cu−Ti (Copper-Titanium) system, Bull. Alloy Phase Diagr., 4 (1983) 81-95.

[31] W.A. Soffa, D.E. Laughlin, High-strength age hardening copper–titanium alloys: redivivus ,Prog. Mater. Sci., 49 (2004) 347-366.

[32] H. Zhang, C. Ma, H. Tian, G. Wu, J. Li, Martensitic transformation of Ni 2 FeGa ferromagnetic shape-memory alloy studied via transmission electron microscopy and electron energy-loss spectroscopy., Phys.Rev.B, 77 (2008) 214106-12.

[33] S.H. Zhou, R.E. Napolitano, Phase stability for the Cu–Zr system: First-principles, experiments and solution-based modeling, Acta Mater., 58 (2010) 2186-2196.

[34] K.A. Darling, M.A. Tschopp, R.K. Guduru, W.H. Yin, Q. Wei, L.J. Kecskes, Microstructure and mechanical properties of bulk nanostructured Cu–Ta alloys consolidated by equal channel angular extrusion, Acta Mater., 76 (2014) 168-185.

[35] S. Cheng, Y. Zhao, Y. Guo, Y. Li, Q. Wei, X.-L. Wang, Y. Ren, P.K. Liaw, H. Choo, E.J. Lavernia, High Plasticity and Substantial Deformation in Nanocrystalline NiFe Alloys Under Dynamic Loading, Adv. Mater., 21 (2009) 5001-5004.

[36] P.V. Liddicoat, X.Z. Liao, Y. Zhao, Y. Zhu, M.Y. Murashkin, E.J. Lavernia, R.Z. Valiev, S.P. Ringer, Nanostructural hierarchy increases the strength of aluminium alloys ,Nat. Commun., 1 (2010) 63-7.

[37] Y. Zhao, T. Topping, J.F. Bingert, J.J. Thornton, A.M. Dangelewicz, Y. Li, W. Liu, Y. Zhu, Y. Zhou, E.L. Lavernia, High tensile ductility and strength in bulk nanostructured nickel., Adv. Mater., 20 (2008) 3028-3033.

[38] L.Y. Chen, J.Q. Xu, H. Choi, H. Konishi, S. Jin, X.C. Li, Rapid control of phase growth by nanoparticles, Nat. Commun., 5 (2014)3879-9.

[39] T. Chookajorn, H.A. Murdoch, C.A. Schuh, Design of stable nanocrystalline alloys,Science, 337 (2012) 951-954.

[40] R.P. Shi, C.P. Wang, D. Wheeler, X.J. Liu, Y. Wang, Formation mechanisms of self-organized core/shell and core/shell/corona microstructures in liquid droplets of immiscible alloys,Acta Mater., 61 (2013) 1229-1243.

[41] D. Wang, Y. Li, B.B. Sun, M.L. Sui, K. Lu, E. Ma, Bulk metallic glass formation in the binary Cu–Zr system, Appl.Phys.Lett., 84 (2004) 4029-3.

[42] Y. Wu, H. Wang, H.H. Wu, Z.Y. Zhang, X.D. Hui, G.L. Chen, D. Ma, X.L. Wang, Z.P. Lu, Formation of Cu–Zr–Al bulk metallic glass composites with improved tensile properties,Acta Mater., 59 (2011) 2928-2936.

[43] D. Arias, J.P. Abriata, Cu-Zr (Copper-Zirconium)， Bull. Alloy Phase Diagr., 11 (1990) 452-459.

[44] H. Okamoto, Cu-Ti (Copper-Titanium)，J. Phase Equilib. Diff., 29 (2008) 204-204.

[45] A. Inoue, W. Zhang, T. Zhang, K. Kurosaka, Thermal and mechanical properties of Cu-based Cu-Zr-Ti bulk glassy alloys， Mater. Trans., 42 (2001) 1149-1151.

[46] L.I. Shunpu, Z. Shengxu, P.A.N. Mingxiang, Z. Deqian, C. Xichen, O.M. Barabash, Solidification process of nonfaceted--faceted eutectic alloys， J. Mater. Sci. Lett., 16 (1997) 171-173.

[47] S.V. Meschel, O.J. Kleppa, hermochemistry of some binary alloys of noble metals (Cu, Ag, Au) and transition metals by high temperature direct synthesis calorimetry， J. Alloys Compd., 350 (2003) 205-212.

[48] T.P. Weihs, T.W. Barbee Jr, M.A. Wall, A low-temperature technique for measuring enthalpies of formation， J. Mater. Res., 11 (1996) 1403-1409.

[49] G. Ghosh, First-principles calculations of structural energetics of Cu–TM (TM = Ti, Zr, Hf) intermetallics， Acta Mater., 55 (2007) 3347-3374.

[50] J.L. Glimois, P. Forey, J.L. Feron, Etudes structurales et physiques d'alliages riches en cuivre dans le systeme CuZr， J. Less Common Met., 113 (1985) 213-224.

[51] R. Valiev, Nanostructuring of metals by severe plastic deformation for advanced properties， Nat. Mater., 3 (2004) 511-516.

[52] Y.H. Zhao, X.Z. Liao, S. Cheng, E. Ma, Y.T. Zhu, Simultaneously increasing the ductility and strength of nanostructured alloys， Adv. Mater.,18 (2006) 2280-2283.

[53] H. Bahmanpour, K.M. Youssef, J. Horky, D. Setman, M.A. Atwater, M.J. Zehetbauer, R.O. Scattergood, C.C. Koch, Deformation twins and related softening behavior in nanocrystalline Cu–30% Zn alloy， Acta Mater., 60 (2012) 3340-3349.

[54] G. He, J. Eckert, W. Loser, L. Schultz, Novel Ti-base nanostructure-dendrite composite with enhanced plasticity， Nat. Mater., 2 (2003) 33-37.

[55] K. Ma, H. Wen, T. Hu, T.D. Topping, D. Isheim, D.N. Seidman, E.J. Lavernia, J.M. Schoenung, Mechanical behavior and strengthening mechanisms in ultrafine grain precipitation-strengthened aluminum alloy， Acta Mater., 62 (2014) 141-155.

[56] P. Zhang, X. An, Z. Zhang, S. Wu, S. Li, Z. Zhang, R. Figueiredo, N. Gao, T. Langdon, Optimizing strength and ductility of Cu–Zn alloys through severe plastic deformation，Scripta Mater., 67 (2012) 871-874.

[57] S. Qu, X.H. An, H.J. Yang, C.X. Huang, G. Yang, Q.S. Zang, Z.G. Wang, S.D. Wu, Z.F. Zhang, Microstructural evolution and mechanical properties of Cu–Al alloys subjected to equal channel angular pressing， Acta Mater., 57 (2009) 1586-1601.

[58] Y.H. Zhao, J.F. Bingert, X.Z. Liao, B.Z. Cui, K. Han, A.V. Sergueeva, A.K. Mukherjee, R.Z. Valiev, T.G. Langdon, Y.T. Zhu, Simultaneously Increasing the Ductility and Strength of Ultra-Fine-Grained Pure Copper，Adv. Mater., 18 (2006) 2949-2953.

[59] X. An, S. Wu, Z. Wang, Z. Zhang, Enhanced cyclic deformation responses of ultrafine-grained Cu and nanocrystalline Cu–Al alloys， Acta Mater., 74 (2014) 200-214.

[60] Z. Zhang, Q. Duan, X. An, S. Wu, G. Yang, Z. Zhang, Microstructure and mechanical properties of Cu and Cu–Zn alloys produced by equal channel angular pressing, Mater. Sci. Eng.: A, 528 (2011) 4259-4267.

[61] X.H. An, Q.Y. Lin, S.D. Wu, Z.F. Zhang, R.B. Figueiredo, N. Gao, T.G. Langdon, The influence of stacking fault energy on the mechanical properties of nanostructured Cu and Cu–Al alloys processed by high-pressure torsion, Scripta Mater., 64 (2011) 954-957.

[62] S. Ren, C. Wen, X. Wu, Y. Gong, Y. Long, L. Cheng, X. Zhu, Influence of stacking fault energy and strain rate on the mechanical properties in Cu and Cu–Al–Zn alloys, Mater. Sci. Eng.: A, 585 (2013) 174-177.

[63] Y.L. Gong, C.E. Wen, X.X. Wu, S.Y. Ren, L.P. Cheng, X.K. Zhu, The influence of strain rate, deformation temperature and stacking fault energy on the mechanical properties of Cu alloys, Mater. Sci. Eng.: A, 583 (2013) 199-204.

[64] S. Zhou, W. Lv, P. Li, Y. Gong, J. Tao, L. Cheng, X. Zhu, Mechanical properties and deformation kinetics of bulk Cu–Al–Zn alloy subjected to rolling and annealing, Mater. Sci. Eng.: A, 609 (2014) 217-221.

[65] Y. Zhang, N. Tao, K. Lu, strain rate and temperature on microstructure and strength of nanostructured Cu–Al alloys subjected to plastic deformation,Acta Mater., 59 (2011) 6048-6058.

[66] D. Jang, J.R. Greer, Transition from a strong-yet-brittle to a stronger-and-ductile state by size reductionofmetallicglasses, Nat. Mater., 9 (2010) 215-219.

[67] J. Gao, J. Sharp, D. Guan, W.M. Rainforth, I. Todd, New compositional design for creating tough metallic glass composites with excellent work hardening,Acta Mater., 86 (2015) 208-215.

Chapter 6

Summary and Conclusions

The objective of the current project was to design new alloys with a superior combination of high strength, high ductility and work hardening in tension. Most of the important discoveries in this project are summarized below.

In chapter 4, a new composition design strategy was proposed to create BMGCs with high strength, large ductility and excellent work hardening from the brittle MgZnCa BMG system. By appropriate choice of alloying elements and composition, the volume fraction, size of both the dendrites and amorphous matrix were effectively tuned by the variation of the composition. This allowed the combination of the yield strength, fracture strength and ductility to be optimised. As the current Mg alloys are substantially hypoeutectic in chemical composition, α-Mg solid solution solidified first from the melt on solidification. The alloying elements Zn and Ca, which have restricted solubility in the equilibrium α-Mg, will have partitioned preferentially to the remaining liquid. The remaining liquid will have frozen into an amorphous state when it is close enough to the (near) eutectic bulk glass forming composition. The increase in alloying elements results in an increase in the volume fraction of amorphous matrix and a decrease in the dendrite size, which leads the higher yielding strength but lower ductility. The mechanical properties of the current Mg alloy can be interpreted by considering the BMGCs as a combination of the nanometer scale metallic glass matrix with a ductile dendritic structure. The high strength, large ductility and excellent work hardening observed in the $\mathrm{Mg}_{91.5}\mathrm{Zn}_{7.5}\mathrm{Ca}_{1}$ can be attributed the homogeneous deformation of nanometre scale amorphous matrices, which delays the formation and rapid propagation of microcracks from the interface.

In chapter 5, a series of in-situ-cast nanostructured CuZrTi alloys were successfully designed by appropriate choice of alloying elements and compositions. XRD and TEM analysis showed that the alloys consisted of softer Cu solid solution and harder nano-scale $Cu_{51}Zr_{14}$ matrix embedded with retained Cu_5Zr . The $Cu_{90.5}Zr_{7.5}$ Ti_2alloy exhibited a yield strength of 787MPa, a fracture strength of 1221MPa and room temperature uniform tensile elongation of 5.16%, exhibiting simultaneous ultrahigh strength and large uniform elongation. The specific structure of these alloys, the uniform distribution ultrafine softer Cu phase with numerous intragranular nanoprecipiates in the nanoscale harder $Cu_{51}Zr_{14}$ matrix embedded with relative softerCu_5Zr , was responsible for the large uniform elongation accompanied with ultrahigh strength. During tensile tests, the relatively softer (larger) primary Cu dendrites with numerous intragranular nanoprecipiates are believed to yield first, leading to substantial dislocation accumulation due to their relatively large grain size and the uniform distribution of numerous intragranular nanoprecipiates. With further increase in loading, the ultrafine Cu solid solution in the ultrafine clusters started yielding and dislocation multiplication commenced in this ultrafine Cu. Meanwhile, the formation deformation bands is believed to start in the primary Cu dendrites due to the high dislocation density already accumulated in these grains, both of which further contribute to the work hardening and uniform plastic deformation. Finally, the hard $Cu_{51}Zr_{14}$ matrix commenced plastic deformation and upon further loading, cracks start formation from the interface, leading to the final failure.

Chapter 7

Future work

1. The EDS analysis shows that the atomic ratio between Zn and Ca is not at 7.5, although both of them have limited solubility in Mg, so a new MgZnCa-based BMGCs can be designed according to the EDS results, which could help to scale up the BMGCs size.
2. The casting method could be optimized to reduce the possibility of formation of voids during injection casting. For example, after melting of the ingots in a small scale melter, the ingots could be placed in a quartz tube, which would then be evacuated and back-filled with argon. This could then be melted in a furnace or in an inductive coil and drop it into oil or liquid nitrogen.
3. The corrosion properties of MgZnCa BMGCs could be studied in simulated body fluid as the MgZnCa BMGs are very promising for its potential application as biodegradable biomaterials due to their good biocompatibility and high corrosion resistance. However, monolithic Mg BMGs are too brittle for practical application. Therefore our Mg-based BMGCs could be a promising candidate as a biodegradable biomaterials.
4. The effect of Zr addition could be investigated as Zr addition could refine the Mg dendrites, which could increase the yielding strength and ductility by grain refining.
5. The solidification behaviour of nanostructured CuZrTi alloys could be studied in more detail by fabrication of samples with different diameters such as 3mm, 5mm and 6mm although the 2mm samples and ingot alloys have been studied in this work.
6. Modelling could be conducted to study the amount of Zr, Ti, and temperature on the mobility of Cu, and Zr atoms, which could be used to solidification mechanism of nanostructured microstructure.

Publications and Conference Presentation

1. Junheng Gao, Joanne Sharp, Dikai Guan, W. Mark Rainforth, and Iain Todd, New compositional design for creating tough metallic glass composites with excellent work hardening, Acta Materialia 86(2015) 208-215.
2. J. Gao, W. M. Rainforth, I. Todd. MgZnCa bulk metallic glass composites as potential temporary implants metals. TMS 2014 (143rd Annual Meeting &Exhibition), February 16-20, 2014 San Diego Convention Centre, San Diego, USA.
3. Junheng Gao, Huairou Zhang,Joanne Sharp, Dikai Guan, W. Mark Rainforth, and Iain Todd, Inhomogeneous structure mediated work hardening and uniform elongation in in-situ-cast nanostructured CuZrTi alloy, In preparation

Appendix Abbreviations and Symbols

BMGC	Bulk metallic glass composite
NM	Nanostructured material
ECAP	Equal channel angle extrusion
HPT	High pressure torsion
BMG	Bulk metallic glass
GFA	Glass forming ability
T_{rg}	Reduced glass transition temperature
T_g	Glass transition temperature
T_{liquid}	Equilibrium liquid state of metallic glass
I(T)	Homogenous nucleation rate
η(T)	Viscosity of metallic glass liquid
ΔG^*	Activation energy
$\Delta g(T)$	Free energy difference between liquid state and crystalline state
ΔH_f	Enthalpy of fusion
ΔS_f	Entropy of fusion
Vit1	$Zr_{41.2}Ti_{13.8}Cu_{12.5}Ni_{10}Be_{22.5}$ metallic glass composite
EDS	Energy-dispersive spectrometer
DSC	Differential Scanning Calorimetry
Δg^{l-c}	Free-energy difference between the liquid phase and crystals decreases
σ_{l-c}	Interface tension between the liquid and the crystal
k_B	Boltzmann constant
STZ	Shear transformation zone
v	Poisson' ratio
μ(T)	Temperature-dependent shear modulus
MG	Metallic glass

SEM	Scanning electron microscopy
TEM	Transmission electron microscopy
Γ	Energy per unit area of shear band,
E	Young's modulus,
a	Aspect ratio height over diameter
m	Strain-rate sensitivity exponent
d_{SB}	Shear band spacing
o_{SB}	Shear-band offset
$V_{f,SB}$	Shear-band affected volume fraction
t_{SB}	Shear-band thickness
SCLR	Supercooled liquid region
Rp	Radius of the plastic zone
λ	Interdendritic spacing,
TRIP	Transformation-induced plasticity
TWIP	Twinning-induced plasticity
k_{1C}	Linear fracture toughness
σ_Y	Yielding strength
G-P zone	A fine-scale metallurgical phenomenon, involving early stage precipitation
XRD	X-ray diffraction
T_{x1}	Onset temperature of crystallization
T_m	Onset temperature of melting
IFFT	Inverse fast Fourier transformation
FFT	Fast Fourier transformation
HRTEM	High resolution transmission electron microscopy
WE43	Mg alloy with composition Y 3.7-4.3, Rare Earth 2.4-4.4, Zr 0.4 W% Mg balance
UTS	Ultimate tensile strength

ρ	Material’s density
$R_{P0.2}$	0.2% proof stress. Stress at which the material undergoes a 0.2% non-proportional extension during a tensile test
H_V	Vickers hardness
HRDSR	High-ratio differential speed rolling
CEC	Cyclic extrusion and compression
PM	Powder metallurgy
HE	Hot extrusion
ARB	Accumulative roll bonding
FSP	Friction stir processing
PGTs	Pre-existing growth twins
f.c.c.	Faced-centred cubic
BF-STEM	Bright field scanning transmission electron microscopy
HAADF-STEM	High-angle annular dark field scanning transmission electron microscopy
AFM	Atomic force microscope
RTR	Rolling at room temperature
LNR	Rolling at liquid nitrogen temperature
HK	Split Hopkinson Pressure Bar impact
DPD	Dynamic plastic deformation at cryogenic temperature
SPD	Severe plastic deformation